DESIGN AND DEVELOPMENT OF CHROMOSPHERIC VECTOR MAGNETOGRAPH FOR SUNSPOT STUDIES

A Thesis

Submitted for the Degree of

Doctor of Philosophy (Technology)

Submitted by

HEMANTH PRUTHVI

Department of Applied Optics & Photonics

University College of Technology

University of Calcutta

May 2019

To my family, friends and mentors...

List of Publications

Refereed Journal Articles

- *Solar spectropolarimetry of Ca II 8542 Å line: polarimeter development, calibration, and preliminary observations*. **Hemanth Pruthvi**, Nagaraju Krishnappa, Ravindra Belur and Ramesh Bheemarao Kadagattor. *Journal of Astronomical Telescopes, Instruments, and Systems*, 2018, 4(04):1, doi:10.1117/1.JATIS.4.4.048002 [1].

- *Kodaikanal Tower-tunnel Telescope Image Stabilization System*. **Hemanth Pruthvi** and R. Sridharan (*In preparation*) [2].

Refereed Conference Proceedings

- *Developing scanning-slit spectrograph for imaging the Sun*. **Hemanth Pruthvi**, K. B. Ramesh, Sajal Kumar Dhara and B. Ravindra. *Ground-based and Airborne Instrumentation for Astronomy VI, SPIE Astronomical Telescopes + Instrumentation*, 2016, 9908:99083V, doi:10.1117/12.2231563 [3].

Publications not Part of the Thesis

- *Solar dynamics imaging system a back-end instrument for the proposed NLST*. K.B. Ramesh, N. Vasantharaju, **P. Hemanth** and K. Reardon. *Experimental Astronomy*, 2016, 42(3):271-283, doi:10.1007/s10686-016-9509-y.

- *Two-channel imaging system for the White light Active Region Monitor (WARM) telescope at Kodaikanal Observatory: design, development, and first images*. **Hemanth Pruthvi** and K. B. Ramesh. *International Conference on Optics and Photonics*, 2015, 9654:96540I, doi:10.1117/12.2182889.

[1] Presented in Chapters 2,3
[2] Presented in Chapters 4
[3] Used in Chapter 2

List of Presentations

- *Solar Scanning Polarimeter at Kodaikanal Tower-tunnel Telescope for Ca II 854.2 nm line*. **Hemanth Pruthvi**, K. Nagaraju and B. Ravindra. *37th Annual meeting of Astronomical Society of India*, 2019, Bengaluru, India. Oral presentation.

- *Rotation correction for full disk images acquired using Coelostat tracking*. **Hemanth Pruthvi** and K. B. Ramesh. *19th National Space Science Symposium*, 2016, Thiruvananthapuram, India. Oral presentation.

- *Developing a full disk longitudinal magnetograph using Lithium Niobate based tunable Fabry-Pèrot filter, for synaptic solar observations at Kodaikanal Observatory*. **Hemanth Pruthvi** and K. B. Ramesh. *International Conference on Optics and Photonics*, 2015, Kolkata, India. Oral presentation.

- *A two-channel imaging system at White light Active Region Monitor (WARM) telescope at Kodaikanal observatory: Design, development and preliminary results*. **Hemanth Pruthvi** and K. B. Ramesh. *33rd Annual meeting of Astronomical Society of India*, 2015, Pune, India. Poster presentation.

Abstract

Solar atmosphere is permeated with magnetic fields of various spatial scales that exhibit dynamics in various temporal scales. Study of so called active regions and their magnetic field measurements are of paramount importance in understanding the solar atmospheric dynamics and energetic events. Although magnetic field maps of photosphere are produced with great regularity, the same cannot be said for chromosphere. Unique conditions offered by chromosphere such as being close to force-free state facilitate better modeling of solar magnetic fields with chromospheric magnetic field measurements.

Magnetic field measurements at chromospheric heights are relatively challenging owing to factors such as (1) lower sensitivity of spectral lines to the magnetic fields, (2) difficulties in modeling the spectral lines, and (3) weaker magnetic field strength at these heights. In this thesis, we present instrumentation aspects of Solar Scanning Polarimeter that has been installed at Kodaikanal Tower-tunnel Telescope of Kodaikanal Solar Observatory to measure the active region magnetic fields at chromospheric level, using spectropolarimetry and Zeeman diagnostics of Ca II 8542 Å spectral line. In chapter 1, magnetic fields of active regions, their properties and their role in solar dynamics are discussed. Motivation for the thesis to measure chromospheric magnetic fields is explained.

In chapter 2, design and development of Solar Scanning Polarimeter, and polarimetry strategy are discussed. Telescope instrumental polarization has been revisited and a possible way to reduce it has been proposed. Instrument controls and operating software are briefly described, along with testing of polarization optics. In chapter 3, polarimetric data acquisition, calibration of the instrument, observations and corrections for instrumental polarization are presented. Polarimetric accuracy and sensitivity are estimated to be few times 10^{-2} and 10^{-3} respectively. Line-of-sight magnetic field map that is synthesized from corrected Stokes profiles using Weak Fields Approximation is presented. Main challenges such as low raster image resolution due to image motion and difficulty in computing transverse magnetic field due to low signal-to-noise ratio are addressed. In chapter 4, design,

development and testing of Image Stabilization System are described. Its development is aimed to reduce image motion induced due to telescope system and seeing. Correlation tracking of sunspot is used to evaluate its performance, and with an acquisition and correction rate of 563 Hz, closed loop correction bandwidth of 110 Hz is achieved.

In chapter 5, a pilot study of correlation between observed chromospheric magnetic field and modeled chromospheric magnetic field (obtained from potential extrapolation using photospheric magnetograms) in the active regions is discussed. In this context, probable formation height of chromospheric spectral line (Ca II 8542 Å) in the active regions is indicated. In chapter 6, thesis is summarized and future scope and needs are outlined.

Contents

List of Figures

List of Tables

Chapter 1

Introduction

1.1 The Sun

In pursuit of study of the celestial bodies, the Sun stands out in the ancient and modern times alike. Understanding the Sun has a multi-fold motive. It is a space laboratory whose prevailing conditions cannot be replicated on earth, giving rise to unique opportunities to study high energy and plasma physics. It is a very common type of star that happens to be closest to the earth, thus enabling study of the Sun in greater detail and making it a template to study rest of the stellar objects. Its effect on the mundane be it seasonal variations, or abrupt events (such as activity in the Earth's magnetic field) is very prominent. Hence, studying the Sun is imperative even for immediate practical concerns.

Electromagnetic radiation is by far the biggest source of information that we are using to study the Sun. A number of observational efforts over the centuries have revealed the fundamental physical properties of the Sun. Advancements on the technological front have enabled the observations at better spatial, spectral and temporal scales resulting in modeling of the Sun.

Model of the Sun According to the standard solar model, structure of the Sun is stratified both internally and externally as shown in Figure 1.1. Internal structure of the Sun consists of three regions: core, radiative zone and convection zone. In core, gravity overwhelms the gas pressure and heats it up to the point where Hydrogen nuclear fusion is triggered. Resultant output energy propagates outwards in the

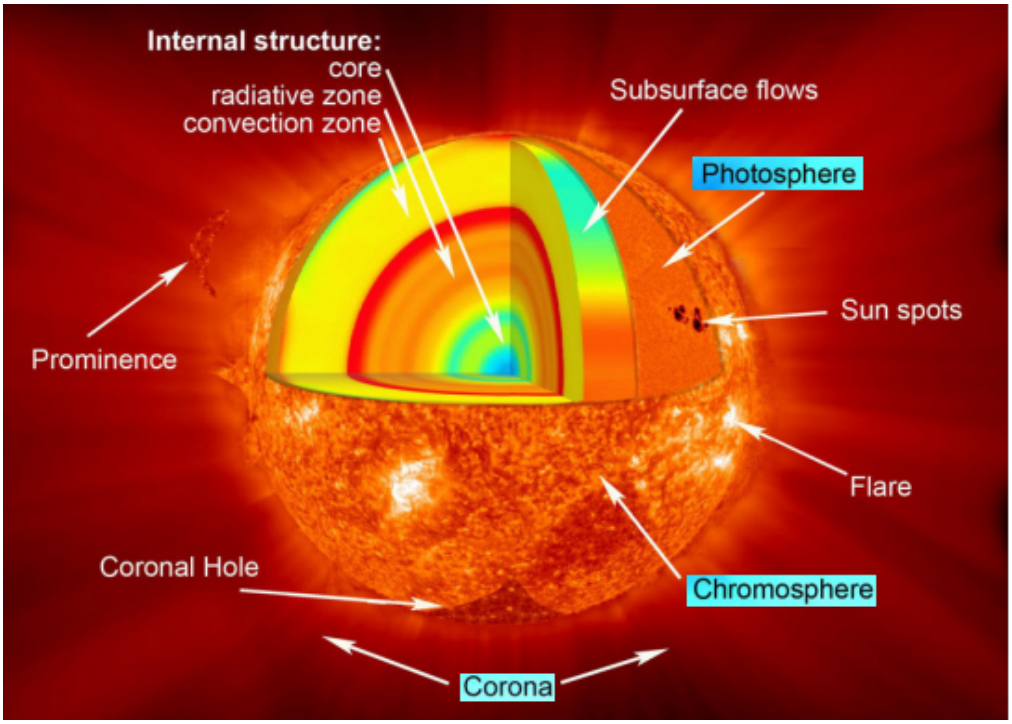

Figure 1.1: The Sun according to the standard solar model. Internal structure consists of core, radiative and convection zones. Atmosphere is mainly categorized as photosphere, chromosphere and corona (image credits: NASA).

form of radiation resulting in the *radiative zone*. Beyond that, gas pressure influence increases and dense plasma transports the energy by means of convection, and this region is called as the *convection zone*. Core and radiative zone rotate like a solid body where as convection zone behaves more like fluid, with *differential rotation* (Spiegel and Zahn, 1992).

Solar atmosphere Solar atmosphere begins at the point where disk becomes visible in white light. It is classified mainly as *photosphere*, *chromosphere* and *corona*. It is observed that the temperature is stratified in the solar atmosphere as shown in Figure 1.2. There is a thin dynamic region between corona and chromosphere where temperature rises drastically that is named as *transition region*. Extension of corona into the planetary system is called *solar wind*.

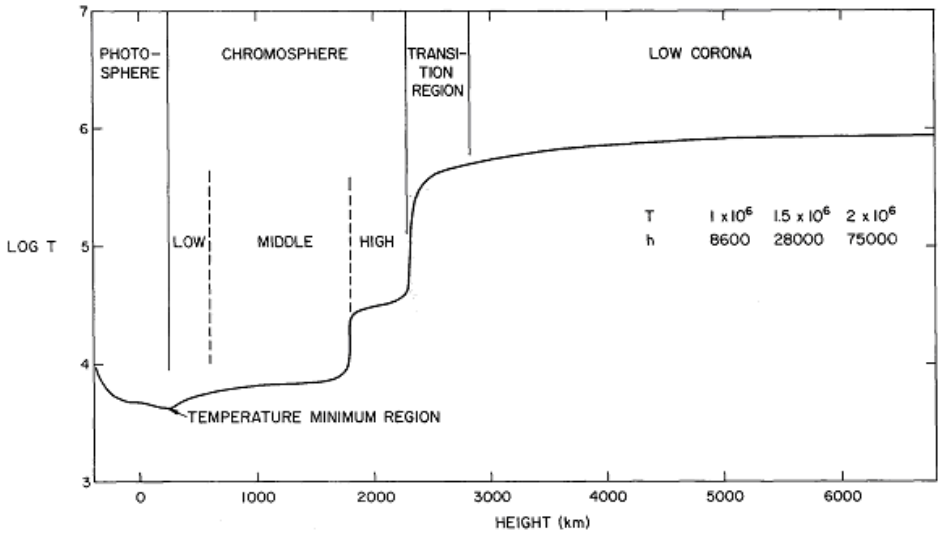

Figure 1.2: Temperature structure of the solar atmosphere. Temperature decreases with height in the photosphere. Chromosphere begins at the height of temperature minimum. Sudden increase in the temperature beyond chromosphere marks the transition region. Image is taken from Athay (1975).

Photosphere Photosphere, as the name suggests, is the visible disk of the Sun spanning roughly 500 km in height with an effective temperature of 5800 K. For a star, beginning of photosphere is defined as a height in the atmosphere where opacity is 50% for the visible radiation (λ=5000 Å). Equivalently, optical depth (τ) for corresponding wavelength would be $\sim 2/3$. As we go deeper into photosphere, atmosphere become opaque. Temperature (T) in photosphere is inferred to be decreasing with the height, by means of observational phenomenon called *limb darkening* that is, intensity decreases as observed from center to the limb. For most intents and purposes, photosphere can be thought to be in Local Thermodynamic Equilibrium (LTE) that is, a single temperature is sufficient to describe thermodynamic state. *Sunspots*, dark features with a lot of variety in shape, size and dynamics, are the most prominent features of this region. Convection from sub-photosphere manifests as *granulation* all over the disk.

Chromosphere Chromosphere is dynamic by definition, spanning the height of temperature minimum to where temperature becomes 25000 K. This roughly corresponds to 500 to 2500 km above photosphere. The name comes from eclipse observations, where a thin ring of red glow is seen around the disk. This glow, as it would be discovered later, is Hα (6563 Å) emission from a height of solar atmosphere that is above the photosphere. To this day, imaging the Sun in Hα is widely used to study a number of interesting features observed in chromosphere such as *prominences*, *filaments* and *spicules*. Sometimes, signatures of bright flash-like events termed *flares* are also observed in this region. As opposed to photosphere, the conditions of the chromosphere are not in LTE (non-LTE or NLTE).

Corona Corona is high temperature rare plasma that extends into the planetary system. It is mainly observed in Ultra-Violet (UV), X-ray and radio regimes, and occasionally in optical regime. It is highly inhomogeneous and structured. It is a thousand times hotter than photosphere but a million times fainter. Hence, the Earth's atmospheric scattering posed a great difficulty in coronal optical observations. However, advent of space observatories in the past decades have overcome this problem and resulted in a wealth of information about corona. It is also home to energetic events that routinely happen in solar atmosphere such as *eruptions* and *Coronal Mass Ejections (CME)*. Some of these events have been correlated with earth bound phenomena.

1.2 Solar magnetism

From continuing observations spanning over a century, researchers have realized that the Sun has magnetic fields at all spatial scales displaying variability in wide range of temporal scales. Many of the features and dynamics of solar atmosphere mentioned earlier are associated with magnetic fields and their dynamics.

1.2.1 Active regions

Sunspots are the most prominent features on the solar disk in visible wavelengths. Their appearance, disappearance and overall variability has fascinated the researchers for nearly four centuries and they have been observed systematically. Phenomenon of appearance of sunspots and variability in the solar magnetic activity are observed to have a periodicity. The so called *solar cyle* was found to have a period of 11 years (Schwabe and Schwabe, 1844). On the same lines, a number of other properties such as total solar irradiance, number of energetic events also observed to have the same periodic behavior (Hathaway, 2015).

In Figure 1.3, details of sunspot structures are marked. Dark central *umbra* is surrounded by less darker *penumbra* with hair-like features. One can see photospheric granulation in the nearby solar continuum. Sometimes sunspots are observed without penumbra and they are termed as *pores*. Although sunspots have been observed for so long, their exact nature has eluded our understanding for better part of that duration.

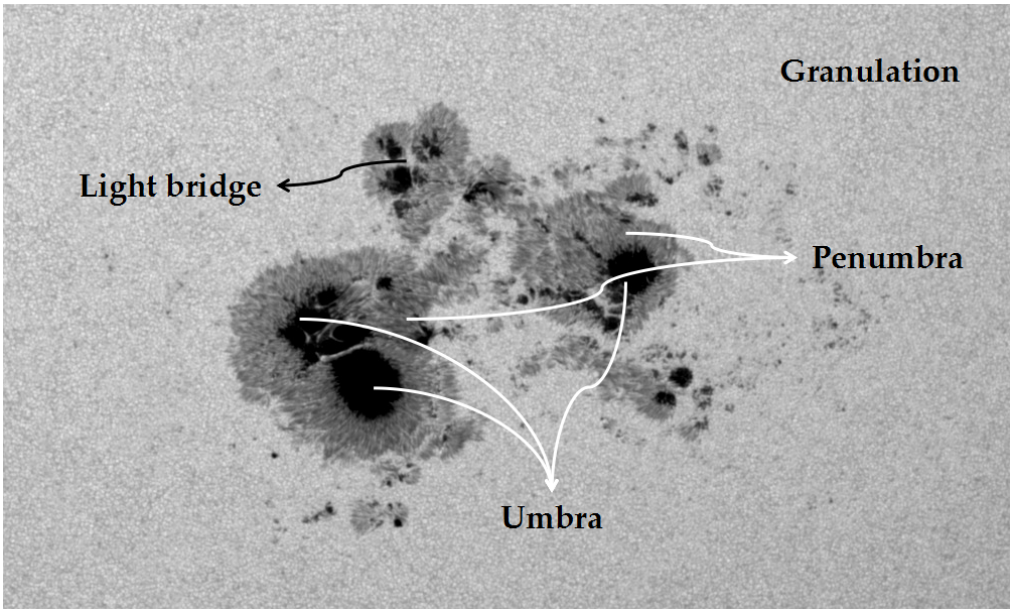

Figure 1.3: Structure of sunspot as seen in active region NOAA AR 12192 (Source: HMI/SDO).

Hale (1908) has observed *magnetic splitting* (splitting of spectral line into several components in presence of a magnetic field, Zeeman, 1897) in the spectra of sunspots and shown that they are visible manifestation of concentrated magnetic field. It has darker appearance as sunspot region is cooler than the surrounding quiet Sun (Maltby et al., 1986). Over the years, magnetic fields and plasma movement in and above the sunspots are extensively studied and mapped in 3-D. In the photosphere plasma seems to be flowing radially outwards, called as *Evershed effect* (Evershed, 1909), and it was inferred from spectroscopic observations of penumbra. However, this trend is reversed in chromosphere as plasma is observed to be flowing inwards (Evershed, 1910), called as *inverse Evershed effect*. Magnetic field lines seem to be concentrated in the photosphere and diverge with increasing height, resulting in a canopy like structure of the magnetic field (Giovanelli, 1980; Giovanelli and Jones, 1982). It all points to necessity to have multi-height observations of magnetic fields to better understand the nature and evolution of the sunspots.

Not only sunspots, but also a number of other observed features are also subsequently associated with magnetic fields. Filaments and prominences observed in Hα filtergrams are modeled to be suspended plasma supported by magnetic field (Anzer, 1987). Analysis of photospheric magnetograms and Extreme UV images of corona have shown that the coronal features seemed to be tracing the magnetic field lines (e.g., Aschwanden et al., 2008). Regions of the strong magnetic activity are aptly termed as *active regions*.

1.2.2 Energetic events

Magnetic field is also inferred to be the root of all the energetic events that are seen in the outer atmosphere. Sometimes, its interplay with plasma gives rise to the release of magnetic energy in the form of explosive events (e.g., Wang et al., 1994). They manifest in a variety of forms such as flares, erupting filaments/prominences and CMEs. An eruption of filament happens as the magnetic field that is supporting the suspended plasma is sufficiently perturbed (e.g., Yang and Chen, 2019). CMEs have been well associated with such eruptions and flares (e.g., Munro et al.,

1979). These explosive events that are observed in chromosphere and corona can be so strong that some of them have been well correlated with changes in earth bound phenomena (e.g., Vemareddy and Mishra, 2015).

1.2.3 Nature of magnetic fields

Solar atmosphere consists of plasma that behaves like ionized gas, and is permeated with magnetic fields. The governing equation for bulk motion in magnetized solar atmosphere is given by (Mullan, 2009),

$$\rho \frac{d\mathbf{V}}{dt} = -\nabla p - \rho \nabla \phi + \frac{1}{c}\mathbf{j} \times \mathbf{B} \tag{1.1}$$

Here, $-\nabla p$ is force exerted due to gas pressure gradient, $-\rho\nabla\phi$ is force due to gravity and $\mathbf{j} \times \mathbf{B}/c$ is *Lorentz force* that is, force exerted by magnetic field. In outer atmosphere, Lorentz force dominates over the other two as gas pressure is low. Dynamic pressure of solar wind also can be ignored till upper corona. Hence, in an equilibrium state (such as filaments/prominences where plasma is suspended) Lorentz force must balance itself.

$$\mathbf{j} \times \mathbf{B} = 0 \tag{1.2}$$

This characterizes the *force-free magnetic field* and consequently current can be written as

$$\mathbf{j} = \alpha \mathbf{B} \tag{1.3}$$

Here, α is a function of space that is, $\alpha(x, y, z)$. Albeit applicable only for chromosphere and corona (Metcalf et al., 1995; Wiegelmann and Sakurai, 2012 and references therein), force-free assumption is widely used to understand how magnetic fields behave through solar atmosphere.

The simplest case of force-free magnetic field is $\alpha = 0$, resulting in $\mathbf{j} = 0$. This special case pertains to *current-free* magnetic field or *potential* magnetic field. Consequently, from Maxwell's third equation, $\nabla \times \mathbf{B} = 0$, implying that potential magnetic fields have no twist in their field lines. Although this is never the case in

practice, especially not for active regions (Wiegelmann et al., 2017), current-free assumption greatly simplifies the computations and results in approximate estimates. Coronal structures are extensively studied by assuming photospheric magnetic fields to be current-free (see review by Wiegelmann et al., 2017).

To de-construct how exactly this Lorentz force acts, we apply $\mathbf{j} = \nabla \times \mathbf{B}(c/4\pi)$ from Maxwell's third equation. Consequently, we get

$$\mathbf{j} \times \mathbf{B} = -\nabla \frac{B^2}{8\pi} + \frac{\mathbf{B}.\nabla}{4\pi}\mathbf{B} \tag{1.4}$$

From aforementioned equation, we gather that magnetic field exerts two different kinds of forces due to: pressure gradient and tension. Interplay between the *magnetic pressure* and gas pressure dictates the magnetic field configuration through most of solar atmosphere. A simple quantity, *plasma-β* is used to characterize the dominance of forces due to two pressures, which is nothing but the ratio of gas pressure to magnetic pressure given by $\beta = 8\pi p/B^2$. In photosphere $\beta > 1$ and it gradually decreases with height and reaches $\beta << 1$ at upper chromosphere, as modeled for plage regions around sunspots (Gary, 2001). Lorentz force dominates the other forces in the chromosphere as the gas pressure is low. Dynamic pressure of solar wind comes into picture at higher corona resulting in $\beta > 1$ (Gary, 2001 and references therein). Low plasma-β is a sufficient criterion for the force-free condition although not necessary (see review by Wiegelmann and Sakurai, 2012 and references therein). A similar trend in plasma β is also inferred for the active region from the same model with observational constraints, except the value of β being two orders of magnitude lower, which explains canopy structure of the magnetic field (see comprehensive review by Solanki et al., 2006, Section 8).

1.3 Observations of solar magnetic fields

In the past decades, measurements of the solar magnetic fields have become an integral part of modeling and making predictions of energetic events. Today such observations to produce magnetic field maps are being carried out in long

and short term by space as well as ground based observing facilities (Lagg et al., 2017). Magnetic field map is called a *magnetogram*, and the instrument that is used to produce a magnetogram is called a *magnetograph*.

Qualitatively, most of the features give away the presence of magnetic fields as they are brighter or darker than the surroundings. In corona, plasma seems to be tracing the magnetic field lines (Wiegelmann et al., 2017) and correspondingly the structures are directly compared with magnetic field lines modeled by current-free extrapolation of the photospheric magnetic field. Features like bright networks observed in Ca K filtergrams of chromosphere are used as proxies (Priyal et al., 2014) for solar polar magnetic field. However, reliable direct quantitative magnetic field measurements are quite challenging. The difficulty increases as we go to outer atmosphere as the magnetic field becomes significantly weaker (Solanki et al., 2006, Section 8).

Photospheric magnetograms are being recorded on daily basis by space-based (Schou et al., 2012) as well as ground-based (Keller and NSO Staff, 1998) observing facilities. Chromospheric magnetograms are sparsely available (Keller and NSO Staff, 1998) compared to their photospheric counterparts. However, coronal magnetic field observations are only a handful due to weak magnetic field strength and less photons from corona. Some are done with radio wavelengths with severely limited spatial resolution (Kumari et al., 2017 and references therein) and very few are done in visible or infrared (IR) wavelengths (Lin et al., 2004). A more common practice is to model the coronal magnetic field by using the observed photospheric magnetic field, under certain assumptions such as those described in Section 1.2.3.

1.3.1 Zeeman effect

Zeeman effect is splitting of a spectral line into several components, in presence of a static magnetic field (Zeeman, 1897). It remains one of the most widely used diagnostic tools to study magnetic fields in the solar atmosphere (Sanchez et al., 1992). Apart from splitting a spectral line with non-zero *Landé g-factor* into its magnetic sub-levels, Zeeman effect produces characteristic polarization across

the spectral line which depends on the direction of the magnetic field with respect to the observer's Line-of-Sight (LoS). This effect is depicted in Figure 1.4. LoS and transverse magnetic field components induce circular and linear polarization respectively.

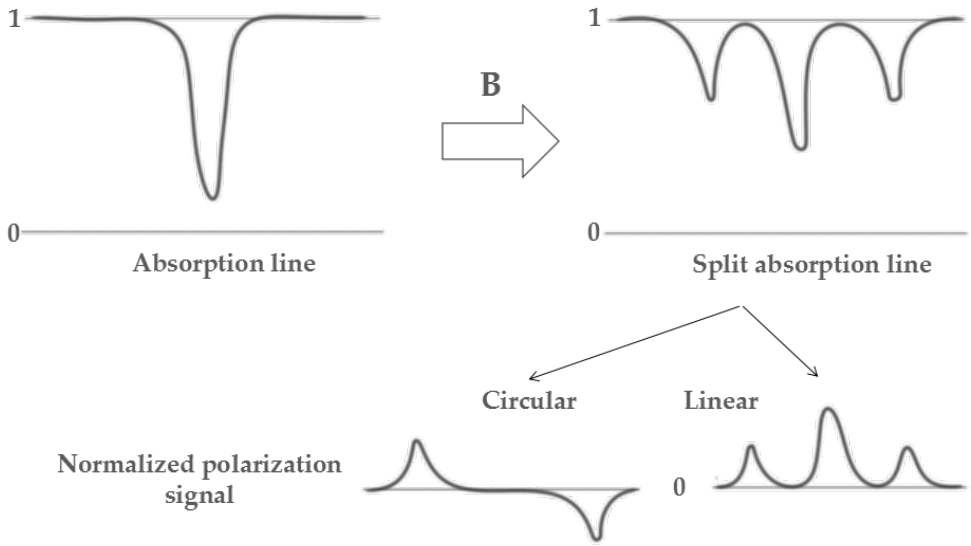

Figure 1.4: Zeeman effect in an absorption line. Splitting is directly proportional to the strength of the magnetic field. If we were to look at polarization in the spectral line, we would see that magnetic field induces circular and linear polarization.

1.3.2 Inferring magnetic field from observations

In solar atmosphere, different spectral lines are formed at various heights as they require specific condition for the formation (e.g., Grossmann-Doerth, 1994). *Spectropolarimetry*, a technique that provides polarized spectral line profiles of selected lines, is widely used to construct a magnetogram corresponding to region of that line formation. By applying radiative transfer theory in magnetized solar atmosphere to spectral lines (Jefferies et al., 1989), polarized line profiles can be synthesized for given model atmospheric conditions. Conversely, given the polarized spectral line profiles, information on line forming region such as magnetic field, velocity and temperature can be obtained. This process is called *inversion* of the polarized line profiles. For spectropolarimetric inversions, an established model

atmosphere is considered as starting point and corresponding line profiles are synthesized. Subsequently, atmospheric parameters are varied until produced synthetic line profiles match with those of the observed ones (Rodríguez et al., 2015). It is computationally very expensive and extensive, especially for the cases of NLTE atmospheric conditions. However, there are simpler and faster ways to get approximate estimates specific parameters (such as only magnetic field or only velocity) which will be discussed in further chapters.

In the context of this thesis, measuring magnetic field at chromospheric heights is of the focus. Most of the light that we see comes from photosphere, so chromosphere is not as easy to observe compared to the photosphere. Most of the spectral lines observed in visible and IR wavelength region are also formed in solar photosphere. However, some absorption spectral lines (especially resonance lines) are formed in solar chromosphere, Hα 6563 Å and Ca II triplet 8498 Å, 8542 Å and 8662 Å to mention a few. Radiation corresponding to these spectral lines enables the direct observations of chromosphere and activity happening at those heights. Consequently, spectropolarimetry of some of aforementioned lines has been used to study active regions and associated energetic events at chromospheric heights. A number of authors have studied structures of sunspots and their role in shaping magnetic fields in the upper atmosphere (Joshi et al., 2016; Robustini et al., 2018) using such observations. Some have reported observations of changes in the magnetic field configuration in chromosphere during flares of various classes (Kleint, 2016; Kuridze et al., 2018).

1.3.3 Observational techniques

Measurements of spectrally resolved polarization provide information on the vector magnetic field. Two techniques that are widely used to perform such observations are 1) Spectrograph based, and 2) Tunable filter based. In the former method, polarized spectra are obtained using a combination of polarimeter and

spectrograph at a given spatial position, and image is scanned in the spatial direction over time. It may involve single or multiple slits (e.g., Vector SpectroMagnetograph (VSM) at Synoptic Optical Long-term Investigations of the Sun (SOLIS), Keller and NSO Staff, 1998), or scanning can be omitted by using optical fibers (e.g., proposed Diffraction-Limited Near InfraRed SpectroPolarimeter at Daniel K. Inouye Solar Telescope, Tritschler et al., 2015).

In the latter method, tunable filters are used to sample the spectral line while obtaining the polarized images of the region of interest for that particular line position. The filters may be Fabry-Perot etalon (e.g., Imaging Spectropolarimeter at Multi Application Solar Telescope, Tiwary et al., 2017), birefringent crystal or Michelson interferometer based ones, or a combination of these (e.g., Helioseismic and Magnetic Imager (HMI) aboard Solar Dynamics Observatory (SDO), Schou et al., 2012). It should be noted that both the methods (spectrograph based as well as tunable filter based) incorporate a *polarimeter* unit to obtain the polarization information, and have respective trade-offs. More on polarimeters is discussed in the next chapter.

1.3.4 Kodaikanal Solar Observatory (KSO)

We aim to develop a suitable instrument for producing chromospheric vector magnetograms using one of the existing optical solar observing facilities: Kodaikanal Tower-tunnel Telescope (KTT) of Kodaikanal Solar Observatory (KSO). It has a High Resolution Spectrograph (HRS) as back-end instrument that enables spectropolarimetry of selected spectral lines. KSO is situated at Kodaikanal peak, Tamilnadu, India. It is located at a latitude of 10.24° North and an altitude of 2300 m. KSO is operational for over a century, and KTT is built in 1960s and operational ever since. It is a refracting telescope with a Coelostat tracking system, and single back-end instrument: HRS. This is a fixed setup (Bappu, 1967) except for the objective, which can be moved only along the optical axis to adjust the focus.

In the existing system, a two-mirror Coelostat placed in the tower is used as a light feeding system. Primary mirror (M1) of the Coelostat tracks the Sun and

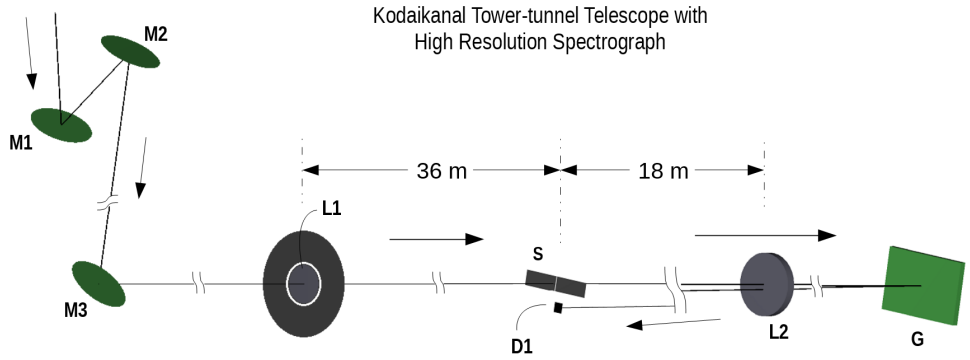

Figure 1.5: A schematic of the Kodaikanal tower-tunnel telescope and high resolution spectrograph. M1, M2 are plane mirrors of the Coelostat system. M3 is plane folding mirror situated at the bottom of the tower. L1 is the objective and it is an achromatic doublet. It forms the image on slit denoted by S. L2 is collimating and imaging lens of the Littrow spectrograph, and G is the reflecting grating. D1 is the science detector which is placed just below the slit.

Table 1.1: Specifications of the KTT, spectrograph and detector.

Front-end specifications	
M1, M2, M3 aperture	60 cm
L1 aperture	38 cm
F-ratio	96
Image plate scale	5.5 arcsec/mm
Spectrograph specifications	
Spectrograph configuration	Littrow
L2 aperture	20 cm
L2 focal length	18.3 m
Grating groove density	600 grooves/mm
Blaze angle	55°
Detector specifications	
Type	CCD
Format	2048 × 2048
Pixel size	13.5 μm
Sensor area	27.6 mm × 27.6 mm
Quantum Efficiency	50% @ 8542 Å
Readout clock	3 MHz

secondary mirror (M2) guides the light vertically down. This beam is fed into the horizontal tunnel by a fold mirror (M3) with 45° orientation. M3 directs the beam

on to an air-spaced doublet lens (L1) which is the objective. Slit based HRS is located at the focal plane of L1. The spectrograph has Littrow configuration, with another air-spaced doublet (L2) acting as a collimator as well as an imager. Blazed reflection grating (G) is the dispersing element in the HRS. Spectrum is focused just below the slit where the science detector (D1) is placed. A schematic of KTT along with the spectrograph setup is shown in Figure 1.5. Important specifications are summarized in Table 1.1.

1.4 Motivation

Principal objective of the thesis is to extend the capability of present solar observing facility with addition of chromospheric vector magnetograph. The purpose of the instrument is to enable creating a magnetic field map of active regions at chromospheric level, by means of spectropolarimetry.

Our aim is driven by motivation to better understand dynamics of the active regions and associated energetic events in the solar atmosphere. Figure 1.6 shows the comparison of images of active region NOAA 12912 taken in white light (corresponds to photosphere), Hα line core (corresponds to chromosphere) and Fe IX 171 Å emission line (corresponds to lower corona). One can see wildly different features and these features have some correspondence to the magnetic field (e.g., Inoue et al., 2016). Hence, magnetic field measurements must be done at as many heights as possible to gain complete perspective.

We have seen that most of the energetic events in the solar atmosphere are observed to be occurring in corona, and their understanding requires complete vector magnetic field information (Hagyard, 1990). For directly observing corresponding magnetic fields, there is little scope outside of photosphere and chromosphere. Photospheric magnetograms are routinely available however, in order to get better perspective chromospheric magnetograms are of utmost importance (Lagg et al., 2017). Polarized chromospheric spectral line profiles are rich in information regarding magnetic filed, velocity and temperature, all of which would be critical in expanding the understanding of dynamic energetic events.

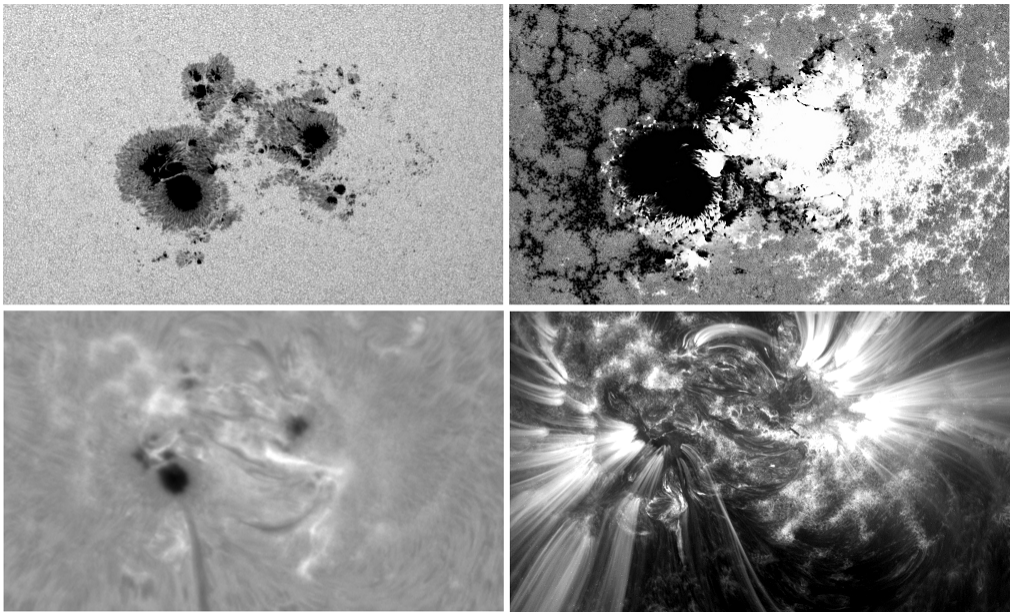

Figure 1.6: Various observations of active region AR 12192 on October 24, 2014. *Top left*: continuum image taken from HMI/SDO that corresponds to photosphere, *top right*: magnetogram taken from HMI/SDO that corresponds to photosphere, *bottom left*: Hα image taken from NSO/GONG network corresponds to chromosphere, and *bottom right*: AIA 171 image taken from AIA/SDO that corresponds to lower corona

As we go higher in the solar atmosphere, it becomes notoriously difficult to directly measure the magnetic fields. As all this activity is rooted in lower atmosphere that is, photosphere, researchers have sought to extrapolating the photospheric magnetic fields to upper layers under force-free condition. But, photosphere is not force-free as opposed to chromosphere which is much closer to being force-free (e.g., Metcalf et al., 1995; Moon et al., 2002; Georgoulis and LaBonte, 2004; Tiwari, 2012). Hence, chromospheric magnetograms are either better suited, or at the least yield better results when used along with photospheric magnetograms for force-free magnetic field extrapolations (Wiegelmann et al., 2008; Fleishman et al., 2018).

We have selected Ca II 8542 Å line to probe the chromospheric magnetic field by means of spectropolarimetric observations. Some of the reasons for choosing this line for diagnosing the chromospheric magnetic field are (Uitenbroek, 2010): (1) The line has continuous sensitivity from upper photosphere to middle chromosphere (τ = 0 to -5). Line wings form in the photosphere and core at a height of $\sim$

1500 km (Lagg et al., 2017). This means that it can provide information on magnetic field, velocity and temperatures at the line formation region, (2) It has good sensitivity to magnetic field with Landé g-factor of 1.10, (3) Spectropolarimetric inversion techniques that are required to infer magnetic field and other parameters from polarization information are well developed and tested, and (4) Existing telescope and Silicon based detectors can be used without much demand. Hence, we planned to build a spectropolarimeter which can probe the chromospheric active region magnetic fields.

1.5 Thesis Structure

The importance of measuring magnetic fields at chromospheric heights is emphasized in previous sections, and motivation for a chromospheric magnetograph is outlined. Accordingly, here we report instrumentation aspects of its development. The main body of the thesis is contained in four chapters.

In chapter 2, design and development aspects of *Solar Scanning Polarimeter* (SSP) are described. Optical design is described along with component selection. A key limitation in polarimetry that is, *Instrumental Polarization* (IP) is discussed. Its analysis and modeling is revisited, and we propose a way to reduce it. Observational plan to obtain data to fit instrumental polarization model is also discussed. Design and development of control electronics and observing software are briefly explained. We also present the laboratory verification of polarizing optical components' specifications.

In chapter 3, we describe data processing procedures. Data acquisition system, characteristics and shortcomings are discussed. Data processing pipeline along with the key steps of data reduction, calibration and observational data processing, and characterization of the data quality are explained in detail. We present the observations of a sunspot using SSP and subsequent magnetic field inferences. We also discuss a main limitation of the current system: image motion, and a potential upgrade to overcome it.

In chapter 4, we describe Image Stabilization System (ISS), an instrument to improve image quality and a subsystem that can be integrated with SSP. We considered previous image motion studies at KTT and devised ISS. Its design, development, and testing at laboratory and KTT are presented. Its potential to arrest the image motion is demonstrated along with other advantages that it may provide.

In chapter 5, we present a pilot study on magnetic fields of the active regions. It is a statistical study using VSM/SOLIS data to find out the probable height of formation for Ca II 8542 Å line in active regions. We describe a method of potential magnetic field extrapolation to compare observed magnetic fields with magnetic fields computed at different heights of solar atmosphere. We present data description, preparation, analysis and results. We discuss these results and future scope for expanding the study.

Finally, we conclude with summary of the work presented. We discuss continuation of the current work and its immediate prospects, along with future work. We also discuss some of the progress made in facilitating a part of this future work.

Chapter 2

Solar Scanning Polarimeter: Design, Development & Testing

2.1 Introduction

Magnetic field measurements of solar features using Zeeman effect as diagnostic tool requires polarized spectral line profiles observed of said feature. Measuring intensity of light as a function of State of Polarization (SoP) is *polarimetry* and the instrument with such capability is called *polarimeter*.

Spectropolarimetry has been tremendously aiding in extending understanding of magnetic fields of the solar atmosphere and its dynamics. State of polarization is inferred by using polarizing elements and modifying the intensity of the light (called *modulation*, discussed in the next section). Babcock (1953) measured circular polarization induced in the spectral line wings due to Zeeman effect by using electro-optical crystal (Ammonium Dihydrogen Phosphate – ADP) as modulator. By switching retardance between -$\lambda/4$ and $\lambda/4$ at a fixed frequency and recording corresponding differential signals in each wing, he was able to measure circular polarization. By means of spatial scanning he was able to produce polarization map and consequently the magnetic field map for two sunspots. Spectrally resolved polarization measurements were made with combination of rotating *waveplates* and grating based spectrographs, and subsequently with interferometer based spectrographs. Waveplates are sliced birefringent crystals sandwiched between optical windows. Modulation was achieved by mechanically rotating the waveplates (e.g.,

Mickey, 1985; Scherrer et al., 1995; Sankarasubramanian et al., 2002; Nagaraju et al., 2008b; Schou et al., 2012).

A number of problems were identified along the way, main one being *seeing-induced cross-talk* (Lites, 1987). Due to the earth's atmospheric disturbances and finite time that takes for polarimetric observations, measured states of polarization would have been mixed up. To counter this problem, a number of solutions were proposed (del Toro Iniesta, 2003, Chapter 4) such as fast *temporal modulation*, *spatial modulation*, or a combination of the two. In case of former technique, fast modulation would enable modulated intensity signals to be recorded in the order of tens of milliseconds or less, before seeing disturbances become effective. For this technique, electro-optic components such as KD*P crystals (Mathew et al., 1998), Liquid Crystals (LC; e.g., Cao et al., 2006; Hanaoka et al., 2011; Tiwary et al., 2017), or Peizo-Elastic Modulators (PEM; e.g., Povel, 2001) were used for modulation. For latter technique, polarizing beam splitters were used after the modulators to record orthogonal states of polarization simultaneously, and cross-talks were removed by means of processing. Such *dual beam* setups were effectively used with rotating waveplates (e.g., Elmore et al., 1992; Beck et al., 2005b; Socas-Navarro et al., 2006; Nagata et al., 2014) as well as electro-optics (e.g., Mártinez Pillet et al., 1999; Keller et al., 2003; Sankarasubramanian et al., 2004; Martínez Pillet et al., 2010) based polarimeters. Although fast modulating polarizing elements have been developed and being used, waveplates still remain relevant to this day (e.g., Hofmann and Rendtel, 2011; Goode et al., 2011; Harrington and Sueoka, 2018) due to their particular advantages such as stable retardance, higher incident energy threshold and availability of larger apertures.

Over the years, a number of spectropolarimetric observations are made by appending polarimeter to existing KTT system. They were developed aiming to measure the vector magnetic fields at photospheric (Sankarasubramanian et al., 2002, using Fe I 6302.5 Å line) as well as at chromospheric heights (Nagaraju et al., 2008a, using Hα 6562.8 Å line). First with the single beam (Balasubramaniam et al., 1985; Sankarasubramanian et al., 2002) and later with dual beam (Nagaraju et al., 2008b)

setup. Some of them suffered from spurious seeing induced cross-talks while others were too slow to measure the Stokes parameters for the whole of a sunspot region. Considering KTT system and limitations of previous polarimeters, a new polarimeter is designed aiming at (1) Improved cadence, (2) Spatial scanning mechanism which is an integral part of the polarimeter, and (3) Provision for imaging channel.

Solar Scanning Polarimeter (SSP) is an instrument designed and developed for KTT of KSO in order to measure polarization in spectral lines produced at each spatial location by scanning a 2-D Region of Interest (RoI) on the Sun. It consists of a polarimeter with an integrated linear scanner and a polarimetric calibration unit. In combination with spectrograph, SSP can produce 4-D data hypercube of spectropolarimetric images. In this chapter, we present design and developmental aspects of SSP. We discuss instrumental polarization, a main interference in measuring polarization from astronomical objects and a possible remedy in the context of KTT.

2.2 Stokes Polarimetry

2.2.1 Stokes formalism

The *Stokes parameters* are the full set of measurable quantities that describe a general SoP of electromagnetic (EM) radiation. They are mathematically expressed as column vector **S** that is,

$$\mathbf{S} = \begin{bmatrix} I \\ Q \\ U \\ V \end{bmatrix} = \begin{bmatrix} < \epsilon_x \epsilon_x^* > + < \epsilon_y \epsilon_y^* > \\ < \epsilon_x \epsilon_x^* > - < \epsilon_y \epsilon_y^* > \\ < \epsilon_x^* \epsilon_y > + < \epsilon_x \epsilon_y^* > \\ i(< \epsilon_x^* \epsilon_y > - < \epsilon_x \epsilon_y^* >) \end{bmatrix} \tag{2.1}$$

where $<>$ stands for time average, $*$ stands for complex conjugate, and ϵ_x & ϵ_y are the complex electric field amplitudes in x & y directions respectively. I, Q, U and V

quantify total intensity, linear polarization along reference axes, linear polarization at 45° with respect to reference axes and circular polarization respectively.

From the aforementioned definition, it follows that transition from one SoP to another can be expressed using a 4×4 matrix, termed *Mueller matrix* (**M**).

$$\mathbf{S_{out}} = \begin{bmatrix} I_{out} \\ Q_{out} \\ U_{out} \\ V_{out} \end{bmatrix} = \mathbf{M}.\mathbf{S_{in}} = \begin{bmatrix} M_{00} & M_{01} & M_{02} & M_{03} \\ M_{10} & M_{11} & M_{12} & M_{13} \\ M_{20} & M_{21} & M_{22} & M_{23} \\ M_{30} & M_{31} & M_{32} & M_{33} \end{bmatrix} \begin{bmatrix} I_{in} \\ Q_{in} \\ U_{in} \\ V_{in} \end{bmatrix} \tag{2.2}$$

Effect of any given physical element or coordinate transformation on observed SoP can be characterized by a corresponding Mueller matrix.

2.2.2 Modulation and demodulation

Detectors that are currently being used in visible and infrared range are only sensitive to the total intensity (I). Hence, SoP is inferred by indirect means of *modulation*. Change in SoP is imprinted as change in intensity by utilizing how selected optical elements affect SoP of light. Optical elements such as *polarizers*, *waveplates* cause changes in amplitude and/or phase of EM wave. Ideal polarizer transmits radiation polarized only in a particular plane where as an ideal wave plate affects only relative phase between ϵ_x and ϵ_y. A combination of such optical elements is used for modulation. Subsequently, SoP is inferred by *demodulating* a series of modulated intensity measurements. Mueller matrix for a combination of rotating waveplate followed by a stationary polarizer is given by

$$\mathbf{M}(\theta, \delta) = \mathbf{M_{polarizer}}(1, 0).\mathbf{M_{rotation}}(-\theta).\mathbf{M_{waveplate}}(\delta).\mathbf{M_{rotation}}(\theta) \tag{2.3}$$

where θ is position angle of waveplate fast axis with respect to fast axis of polarizer and δ is retardation of waveplate. Output of such system takes the form of

$$\begin{bmatrix} I_{out} \\ Q_{out} \\ 0 \\ 0 \end{bmatrix} = \mathbf{M}(\theta, \delta) \begin{bmatrix} I_{in} \\ Q_{in} \\ U_{in} \\ V_{in} \end{bmatrix} \text{ and } I_{out} = Q_{out} \tag{2.4}$$

where

$$\begin{aligned} I_{out} =& \frac{1}{2}(I_{in} + (cos^2 2\theta + sin^2 2\theta cos\delta)Q_{in} \\ &+ sin2\theta cos2\theta(1 - cos\delta)U_{in} - sin2\theta sin\delta V_{in}) \end{aligned} \tag{2.5}$$

In this system polarizer at the end is called an *analyzer*. Similarly, a number of modulation schemes can be devised by using a combination of retarders. As only the intensity can be directly measured, only first row of the Mueller matrix is relevant for modulation. To obtain all the four Stokes parameters, at least four intensities and corresponding Mueller matrices' first rows should be known. All such intensities can be expressed in matrix form as shown in Eq. (2.6).

$$\begin{bmatrix} I^1_{out} \\ I^2_{out} \\ \vdots \\ I^n_{out} \end{bmatrix} = \begin{bmatrix} 1 & m^1_{01} & m^1_{02} & m^1_{03} \\ 1 & m^2_{01} & m^2_{02} & m^2_{03} \\ \vdots & \vdots & \vdots & \vdots \\ 1 & m^n_{01} & m^n_{02} & m^n_{03} \end{bmatrix} \begin{bmatrix} I_{in} \\ Q_{in} \\ U_{in} \\ V_{in} \end{bmatrix} \tag{2.6}$$

$$\text{or } \mathbf{I_{out}} = \mathbf{O}.\mathbf{S_{in}}$$

Here, **O** is called *modulation matrix* and $m_{0i} = M_{0i}/M_{00}$. **O** should have a rank of four to measure four Stokes parameters (del Toro Iniesta and Collados, 2000). It is shown in a generalized form for n number of modulations in Eq. (2.6). Simple way to implement modulation is to rotate waveplate in discrete steps.

In order to retrieve input Stokes parameters, measured intensities must be *demodulated*. If Eq. (2.6) is pre-multiplied with pseudo-inverse of **O**, it would be

$$\begin{aligned} \mathbf{S_{in}} &= \mathbf{D}.\mathbf{I_{out}} \\ \text{where } \mathbf{D} &= (\mathbf{O^T}.\mathbf{O})^{-1}.\mathbf{O^T}. \end{aligned} \tag{2.7}$$

D is an *optimum* demodulation matrix for **O** (del Toro Iniesta and Collados, 2000).

In practice, modulation matrix is to be determined experimentally as aforementioned equations describe ideal behaviour of polarizing elements. To do so, light with known SoP ($\mathbf{S_{calin}}$) is sent through the polarimeter and intensity outputs are measured for all modulations. This is repeated for at least four different known SoP and all the intensities are recorded ($\mathbf{I_{calout}}$). From these intensity measurements, modulation matrix can be calculated as given in Eq. (2.8). This process is called *polarimetric calibration*.

$$\begin{aligned} \mathbf{I_{calout}} &= \mathbf{O}.\mathbf{S_{calin}} \\ \mathbf{O} &= \mathbf{I_{calout}}.\mathbf{S_{calin}^T}.(\mathbf{S_{calin}}.\mathbf{S_{calin}^T})^{-1}. \end{aligned} \tag{2.8}$$

2.2.3 Modulation scheme

We have worked out a *balanced* modulation scheme for polarimetry such that it gives approximately equal weights to Stokes parameters when they are being recorded. A simple balanced scheme comprising of four-stepped modulation is used for this polarimeter. The four-step modulation scheme is chosen with the objective of keeping observing time to a minimum. It also has equal $efficiency$ for measuring Q, U and V. Modulation matrix corresponding to this scheme is given in Eq. (2.9).

$$\mathbf{O_{bal}} = \begin{bmatrix} 1 & \mp 0.577 & \pm 0.577 & \mp 0.577 \\ 1 & \pm 0.577 & \mp 0.577 & \mp 0.577 \\ 1 & \mp 0.577 & \mp 0.577 & \pm 0.577 \\ 1 & \pm 0.577 & \pm 0.577 & \pm 0.577 \end{bmatrix}. \tag{2.9}$$

In practice, it can be implemented by using a combination of quarter-waveplate (QWP), half-waveplate (HWP) and analyzer whose Mueller matrix is

$$\begin{aligned}\mathbf{M}(\theta_Q, \theta_H) =& \mathbf{M_{analyzer}}. \\ & \mathbf{M_{rotation}}(-\theta_H).\mathbf{M_{HWP}}.\mathbf{M_{rotation}}(\theta_H). \\ & \mathbf{M_{rotation}}(-\theta_Q).\mathbf{M_{QWP}}.\mathbf{M_{rotation}}(\theta_Q)\end{aligned} \tag{2.10}$$

where, θ_Q and θ_H are rotation angles for QWP and HWP respectively. The output intensity is given by

$$\begin{aligned}I_{out} = \frac{1}{2}(I_{in} &+ [cos^2 2\theta_Q(1 + cos4\theta_H) + sin2\theta_Q cos2\theta_Q sin4\theta_H]Q_{in} \\ &+ [sin2\theta_Q cos2\theta_Q(1 + cos4\theta_H) + sin^2 2\theta_Q sin4\theta_H]U_{in} \\ &- [sin2\theta_Q(1 + cos4\theta_H) - cos2\theta_Q sin4\theta_H]V_{in})\end{aligned} \tag{2.11}$$

2.3 Instrument Design and Development

2.3.1 Optics

Unlike in the previous polarimeter setup by Nagaraju et al. (2007), this polarimeter is placed perpendicular to the optical path from the objective to the slit that is, optical axis is folded by 90° within the polarimeter. This configuration has been worked out keeping in view of two requirements. One is to have an integrated scanning system, and the other is to reduce certain cross-talks due to telescope system (detailed in Section 2.4). The optical layout of the polarimeter setup at KTT is shown in Figure 2.1. Incoming beam is directed through SSP using a plane mirror that also acts as Mode Switching Mirror (MSM), inclined at $\sim$ 45°. It enables switching to calibration mode by retracting completely and allowing light from the calibration unit to pass through polarimeter. A natural consequence of this mirror is to nullify the instrumental polarization introduced by M3, which is discussed in detail in Section 2.4.

A combination of Quarter-Wave Plate (QWP) and Half-Wave Plate (HWP) is used for the modulation and they constitute the modulation unit. QWP and HWP

position angles to implement the balanced modulation scheme are listed in Table 2.1. A Dichroic Beam Splitter (DBS), Scanning Mirror (SM) are placed following the modulation unit. DBS is a long pass filter with cut-off at 600 nm. Reflected beam is captured by an Imaging Detector (ID) for the purposes of context imaging. Transmitted beam is reflected by SM on to the slit. SM moves along the direction of incident beam and consequently image is moved across the slit. Although moving SM alone to scan the image does cause focal plane to shift, the effect is negligible considering a depth of focus of $\sim$ 50 mm provided by $f/96$ beam.

Table 2.1: List of QWP and HWP position angles to implement the balanced modulation scheme given in Eq. (2.9). They are derived using Eq. (2.11).

No.	QWP position	HWP position
1	-22.5°	42.6°
2	-22.5°	69.9°
3	22.5°	47.4°
4	22.5°	20.1°

Polarizing Beam Displacer (PBD) is used as analyzer as it separates two linearly polarized light beams. These two beams have orthogonal states of polarization and they are parallel to each other. A two-beam analyzer gives significant advantage in terms of reducing seeing induced cross-talk over single beam polarizers (Lites, 1987). Analyzer is followed by reflection grating based HRS and grating's reflectivity is dependent on the SoP of incident light. To compensate for the difference in grating's response for outputs of PBD, an Achromatic Quarter-Wave Plate (AQWP) (600 – 900 nm) is placed after PBD. It converts two linearly polarized outputs into circularly polarized outputs.

A calibration unit consisting of a Glan-Thompson Polarizer (GTP) and a Calibration Wave Plate (CWP) is used to generate the known state of polarization. GTP polarizes the light to a very high degree ($\sim 10^5$) and a zero-order QWP is used as CWP. As previously mentioned, MSM is completely retracted in calibration mode so that light from the calibration unit may pass through the polarimeter.

Table 2.2: Specifications of the instrument and settings of the spectrograph.

Specification	Value
Wavelength of interest	8542 Å
Order	2
Slit width	110 μm
Detector binning	2×2
Linear dispersion	10.8 mÅ/pixel
Slit equivalent wavelength extent	43 mÅ
Spectral resolution	64 mÅ
Wavelength coverage	10.8 Å
Field of View	60 arcsec
Retardance of the calibration wave plate	0.249λ
PBD entrace size	12 mm
Extent of the scan	23 mm
Wave plate rotation speed	15 rpm
Scanning speed	1 mm/s
Scan step	110 μm

2.3.2 Mechanics

Figure 2.2 depicts 3-D mechanical shaded drawing of assembled instrument. QWP, HWP and CWP are placed in motorized rotation mounts with homing position sensor. Mode switching mirror is placed on motorized linear stage with long travel (70 mm) to enable its complete retraction from optical path. Scanning mirror is placed on short-travel motorized linear stage (30 mm) that can cover sufficient region of interest. These motorized elements achieve rotation or translation using stepper motors driven by micro-stepping drives. GTP and AQWP are mounted on manual rotation mounts as they only require one time setup. Once their fast-axes are determined, their position angles are set to predetermined values and locked. This setup is fixed on single portable platform and the platform is placed on the optical bench that rests before the slit.

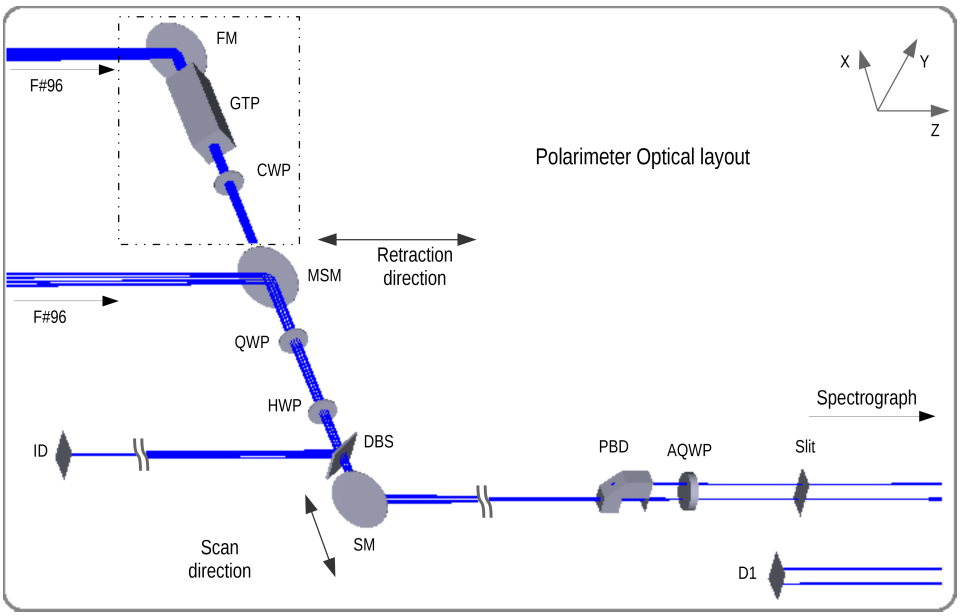

Figure 2.1: Optical layout of solar scanning polarimeter setup at KTT. In observation mode, light from the telescope is fed to the modulation unit by a folding mirror (MSM). It passes through quarter wave plate (QWP), half wave plate (HWP), and dichroic beam splitter (DBS) that transmits light of wavelength above 600 nm. It is then reflected by another fold mirror (SM), and passes through a polarizing beam displacer (PBD) that splits the beam in to two with orthogonal states of polarization, followed by an achromatic quarter wave plate (AQWP). In calibration mode, light from the telescope is fed to the calibration unit by yet another folding mirror (FM). It then passes through a Glan-Thompson polarizer (GTP) and a quarter wave plate (CWP) producing light with known state of polarization. In this mode MSM is retracted and the light is allowed to passes through modulation unit and so on.

2.3.3 Control electronics

Solar scanning polarimeter is operated using a custom made controller, based on micro-controllers. It receives commands from the computer via serial communication and executes them. It consists of two Motorized Element Controllers (MEC) developed in-house, operating in Master-Slave mode. Each MEC can control three motorized elements. Three motorized rotation mounts for the wave plates and two motorized linear stages for the mirrors, with home positioning sensors are controlled. Control block diagram and image of controller are presented in Figure 2.3.

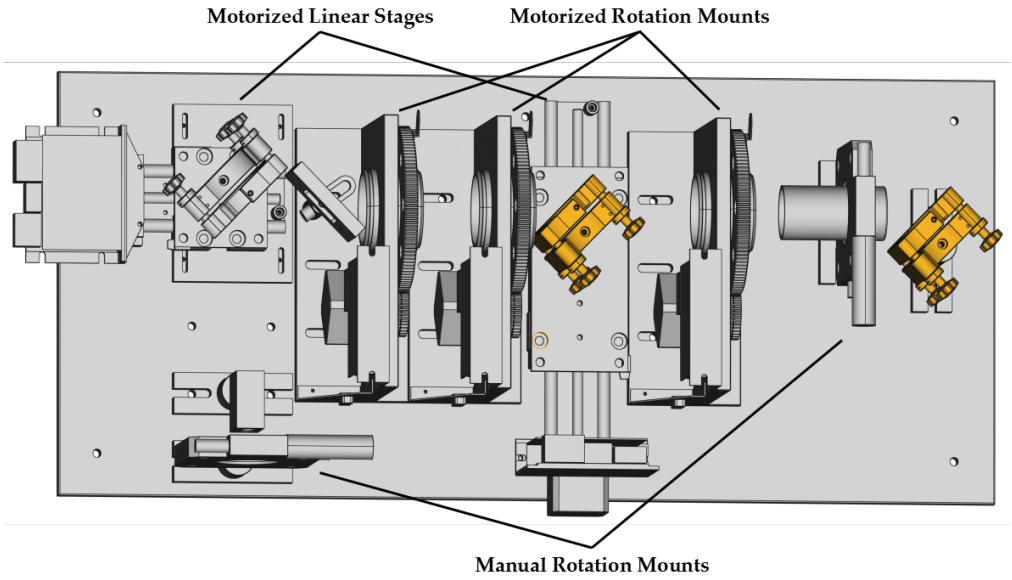

Figure 2.2: Shaded model of mechanical setup of solar scanning polarimeter.

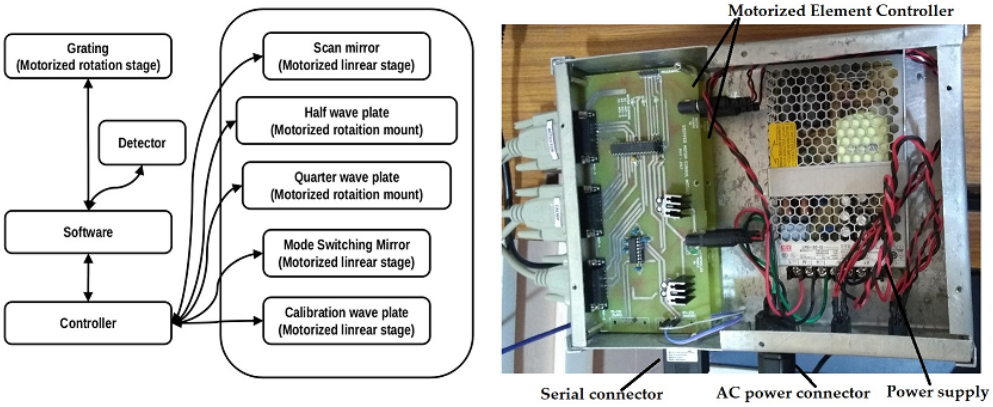

Figure 2.3: Solar scanning polarimeter control block diagram (*left*), and picture of custom-made controller (*right*).

2.3.4 Control software

The control software is developed in Python programming language using Qt4 Graphical User Interface (GUI) framework. It operates SSP by communicating with the controller. It is equipped with a wide range of functionality to enable the user to obtain a variety of observations. It operates the detector using Python programming library of Micro-Manager (Edelstein et al., 2010) image acquisition software. Salient features of the software are listed below and a snapshot of GUI is presented

in Figure 2.4.

- Executing modulation scheme (4-step scheme is used but provision is given so that up to 8-step modulation schemes can be executed).
- Simple raster scans (spectral imaging without polarimetry) and stacked frame acquisition.
- Access to commonly used detector settings and live preview.
- Auto-save frames and log with predefined directory structure.
- Key spectrograph grating stage controls such as spectral line selection.
- Command line option to send custom serial commands to controller and grating stage.

2.4 Instrumental polarization

Instrumental polarization of the Coelostat was recognized as a significant hurdle, and was modeled and measured for over 100 years (St. John, 1909; Hale, 1912; Bumba and Topolová-Růžičková, 1962; Capitani et al., 1989; Demidov, 1991). Earlier works to develop polarimeter for KTT also included developing a theoretical model for the instrumental polarization (Balasubramaniam et al., 1985). This model was used in subsequent polarimeters (Sankarasubramanian et al., 1999; Nagaraju et al., 2008a). The new model, which essentially is an extension of the previous model, is developed aiming to find ways to reduce the instrumental polarization, and it is discussed in detail further. ZEMAX model of the Coelostat is also created and the resulting output instrumental polarization values are compared. For the purposes of comparing the model and simulation, all the mirrors are taken to have unprotected Aluminium coating, and its complex refractive index (RI) at 8542 Å wavelength is taken to be $2.16 - 7.18i$ (McPeak et al., 2015).

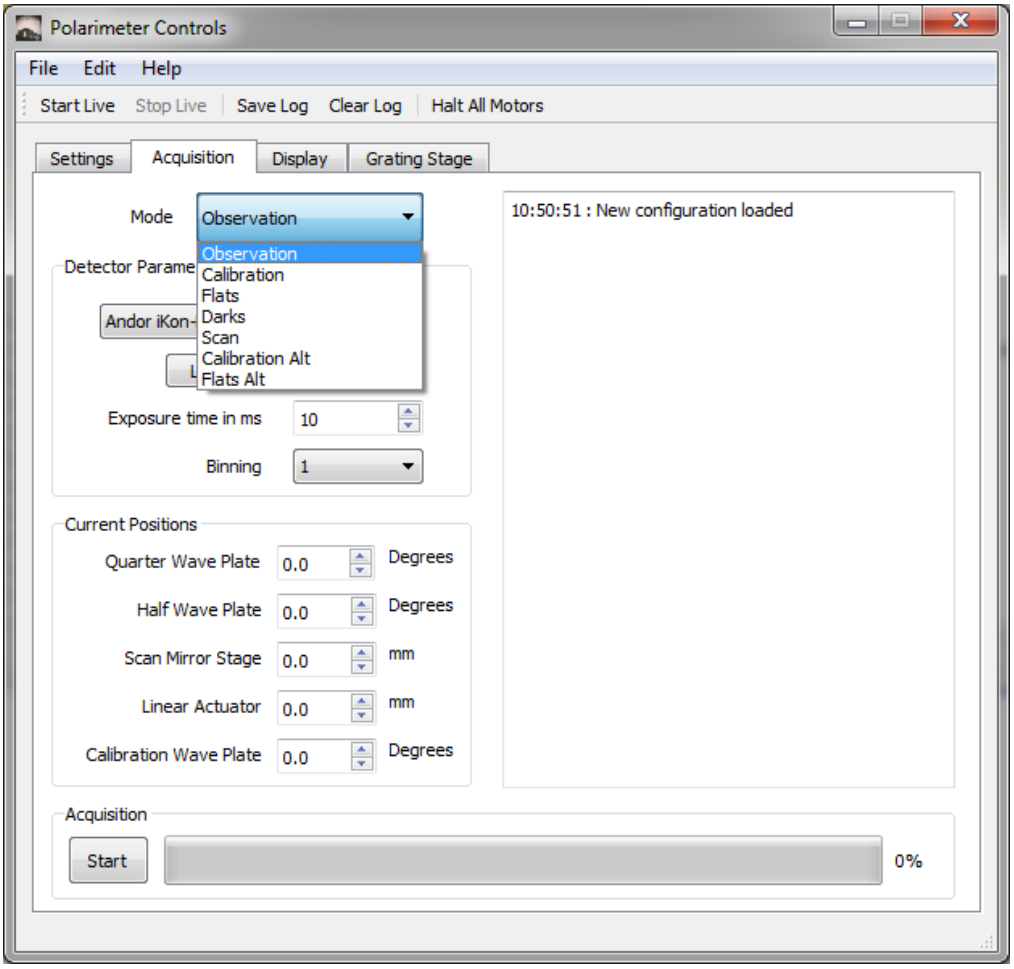

Figure 2.4: Graphical User Interface (GUI) developed in Python programming language to control solar scanning polarimeter, science detector and the grating stage.

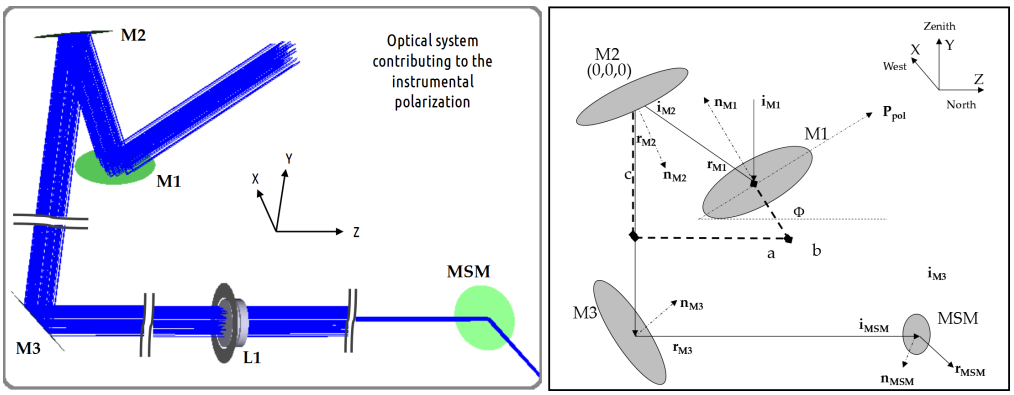

Figure 2.5: *Left*: optical system contributing to the instrumental polarization – M1, M2, M3, L1 and MSM. *Right*: coordinate system and conventions used in the model.

2.4.1 Analytical model

Instrumental polarization introduced by a mirror depends on the angle of incidence and the complex refractive index of the coating. In order to estimate the instrumental polarization of a series of mirrors, transformations of the local coordinate system also should be known. The Direction Cosines (DC) of the vectors relevant to get the incident angles are calculated. Coelostat model uses following convention for the coordinate system and angles.

Table 2.3: List of axes and angles, and their convention, along with input and model parameters, and their values as used in KTT Coelostat model.

Coordinate	Direction
Origin	Center of M2
$+X$	West
$+Y$	Zenith
$+Z$	North
Latitude, $+\phi$	Southern
Declination, $+DEC$	Northern
Hour Angle, $+HA$	Western
Input parameters	**Value**
Declination, DEC	$[-23.5^\circ, 23.5^\circ]$
Hour Angle, HA	$[-90^\circ, 90^\circ]$
Latitude, ϕ	-10.24°
M1 – M2 distance in East – West direction, a	830 mm
M1 – M2 distance in vertical direction, c	740 mm
Model parameters	**Default value**
Complex RI of Al coating, n_{Al}	$2.16 - 7.18i$
Complex RI of Al_2O_3 coating, n_{oxide}	1.54
Thickness of Al_2O_3 coating, t_{oxide}	0 Å

DC of the Sun's position and subsequently the for the incidence on M1 are

$$\begin{aligned}\mathbf{P_{Sun}} =&(\sin HA \cos DEC,\\ &\cos HA \cos DEC \cos\phi - \sin DEC \sin\phi,\\ &\cos HA \cos DEC \sin\phi + \sin DEC \cos\phi),\end{aligned} \tag{2.12a}$$

$$\mathbf{i_{M1}} = -\mathbf{P_{Sun}}. \tag{2.12b}$$

where HA, DEC and ϕ denote hour angle and declination of the Sun, and latitude of the observing location respectively.

DC of the rotation axis of the M1 i.e., polar axis are

$$\mathbf{P_{Pol}} = (0, -\sin\phi, \cos\phi). \tag{2.13}$$

Reflected beam must be towards M2 hence its DC are

$$\mathbf{r_{M1}} = \frac{(a, c, b)}{\sqrt{a^2 + b^2 + c^2}}. \tag{2.14}$$

where a, c and b are distances between M1 and M2 in X, Y and Z directions respectively.

DC of the normal to M1 are

$$\mathbf{n_{M1}} = \frac{\mathbf{r_{M1}} - \mathbf{i_{M1}}}{|\mathbf{r_{M1}} - \mathbf{i_{M1}}|}. \tag{2.15}$$

This must be normal to the polar axis, and solving Eq. (2.16a) results in the value for b, as given in Eq. (2.16b).

$$\mathbf{n_{M1}}.\mathbf{P_{Pol}} = 0, \tag{2.16a}$$

$$b = B + \frac{DEC}{|DEC|}\frac{\sqrt{B^2 - 4AC}}{2A}, \tag{2.16b}$$

where A, B, C are given by

$$\begin{aligned} A &= \cos^2\phi - (\mathbf{i_{M1}}.\mathbf{P_{Pol}})^2, \\ B &= -2c\sin\phi\cos\phi, \\ C &= c^2\sin^2\phi - (a^2 + c^2)(\mathbf{i_{M1}}.\mathbf{P_{Pol}})^2. \end{aligned}$$

On the polarimeter side, position and orientation of M3 and MSM are fixed. So, DC for the beam which is reflected from MSM, and DC for the beam incident on MSM are

$$\mathbf{r_{MSM}} = (-1, 0, 0), \tag{2.17a}$$

$$\mathbf{i_{MSM}} = (\sin 0.4^\circ, 0, \cos 0.4^\circ), \tag{2.17b}$$

$$\mathbf{n_{MSM}} = \frac{\mathbf{r_{MSM}} - \mathbf{i_{MSM}}}{|\mathbf{r_{MSM}} - \mathbf{i_{MSM}}|}. \tag{2.17c}$$

DC for the normal, incident and reflection from M3 are

$$\mathbf{n_{M3}} = (0, \cos 45^\circ, \sin 45^\circ), \tag{2.18a}$$

$$\mathbf{r_{M3}} = \mathbf{i_{MSM}}, \tag{2.18b}$$

$$\mathbf{i_{M3}} = \mathbf{r_{M3}} - 2(\mathbf{r_{M3}}.\mathbf{n_{M3}})\mathbf{n_{M3}}. \tag{2.18c}$$

From the above equations, DC of M2 normal as well as incident and reflections are

$$\mathbf{i_{M2}} = \mathbf{r_{M1}}, \tag{2.19a}$$

$$\mathbf{r_{M2}} = \mathbf{i_{M3}}, \tag{2.19b}$$

$$\mathbf{n_{M2}} = \frac{\mathbf{r_{M2}} - \mathbf{i_{M2}}}{|\mathbf{r_{M2}} - \mathbf{i_{M2}}|}. \tag{2.19c}$$

The electric field vector can be decomposed to have two orthogonal components: parallel (p) and perpendicular (s) to the plane of incidence and reflection. Together, direction of propagation, s and p form a right handed coordinate system.

DC for the s polarized components corresponding to each mirror are

$$\mathbf{s_{M1}} = \frac{\mathbf{i_{M1}} \times \mathbf{n_{M1}}}{|\mathbf{i_{M1}} \times \mathbf{n_{M1}}|}, \tag{2.20a}$$

$$\mathbf{s_{M2}} = \frac{\mathbf{i_{M2}} \times \mathbf{n_{M2}}}{|\mathbf{i_{M2}} \times \mathbf{n_{M2}}|}, \tag{2.20b}$$

$$\mathbf{s_{M3}} = \frac{\mathbf{i_{M3}} \times \mathbf{n_{M3}}}{|\mathbf{i_{M3}} \times \mathbf{n_{M3}}|}. \tag{2.20c}$$

$$\mathbf{s_{MSM}} = (0, -1, 0) \tag{2.20d}$$

The three angles for three coordinate rotations, considering the signs, are

$$\theta_{M1-M2} = \frac{(\mathbf{s_{M1}} \times \mathbf{s_{M2}}).\mathbf{r_{M1}}}{|(\mathbf{s_{M1}} \times \mathbf{s_{M2}}).\mathbf{r_{M1}}|} \cos^{-1}(\mathbf{s_{M1}}.\mathbf{s_{M2}}), \tag{2.21a}$$

$$\theta_{M2-M3} = \frac{(\mathbf{s_{M2}} \times \mathbf{s_{M3}}).\mathbf{r_{M2}}}{|(\mathbf{s_{M2}} \times \mathbf{s_{M3}}).\mathbf{r_{M2}}|} \cos^{-1}(\mathbf{s_{M2}}.\mathbf{s_{M3}}), \tag{2.21b}$$

$$\theta_{M3-MSM} = 89.6^{\circ}. \tag{2.21c}$$

As the complete information about the mirrors' positions and orientations are known, Mueller matrix of the system ($\mathbf{M_{sys}}$) can be constructed as given in Eq. (2.22). This is a function of HA and DEC. Present system has a time varying component as two mirrors of the Coelostat are tracking the Sun all day throughout the year. Hence, M1 and M2 constitute time-varying system ($\mathbf{M_{time-var}}$), and M3 and MSM constitute time-independent system ($\mathbf{M_{time-ind}}$). Here, $\mathbf{M}$ represents Mueller matrix for reflection and $\mathbf{R}$ represents the same for rotation.

$$\mathbf{M_{time-var}} = \mathbf{R}(\theta_{M2-M3})\mathbf{M_{M2}}\mathbf{R}(\theta_{M1-M2})\mathbf{M_{M1}}, \tag{2.22a}$$

$$\mathbf{M_{time-ind}} = \mathbf{M_{MSM}}\mathbf{R}(\theta_{M3-MSM})\mathbf{M_{M3}}, \tag{2.22b}$$

$$\mathbf{M_{sys}} = \mathbf{M_{time-ind}}\mathbf{M_{time-var}}. \tag{2.22c}$$

2.4.2 Simulation

The system is simulated in the ZEMAX non-sequential mode. PyZDDE (Sinharoy et al., 2016) - a Python-ZEMAX interface is used to interactively change the parameters and perform ray tracing for this dynamic system. Instrumental polarization of the system is calculated by giving six inputs ($\pm Q, \pm U, \pm V$, one at a time) and performing polarimetry at the output. The simulation is done for the time varying and time independent parts separately for the sake of comparison.

In the present model, Coelostat Mueller matrix is treated to be a product of two Mueller matrices: time-independent and time-varying parts. Time-independent part consists of effects of the tertiary mirror and MSM. By virtue of the design of SSP, configuration of time-independent part is created in such a way that the Mueller matrix is close to identity (Cox, 1976). Mueller matrices computed from theoretical model and the ZEMAX model for time-independent part are given in Eq. (2.23).

$$\mathbf{M_{CTI-Th}} = \begin{bmatrix} 1.0000 & 0.0006 & -0.0007 & -0.0001 \\ 0.0005 & 0.9999 & 0.0138 & 0.0025 \\ -0.0007 & -0.0138 & 0.9999 & 0.0019 \\ -0.0001 & -0.0025 & -0.0019 & 1.0000 \end{bmatrix}, \tag{2.23a}$$

$$\mathbf{M_{CTI-Si}} = \begin{bmatrix} 1.0000 & 0.0016 & -0.0007 & -0.0001 \\ 0.0016 & 0.9999 & 0.0138 & 0.0025 \\ -0.0008 & -0.0137 & 0.9999 & 0.0052 \\ -0.0001 & -0.0024 & -0.0050 & 0.9999 \end{bmatrix}. \tag{2.23b}$$

The disagreement of certain terms of the Mueller matrices can be attributed to the fact that the theoretical model only considers two mirrors in collimated beam where as the ZEMAX model is based on real configuration of the system i.e., it also accounts for the objective lens after M3 and the effects of $f/96$ beam on the MSM.

As for the time-varying part, instrumental polarization is very high in the morning and evening, and gradually decreases with decreasing magnitude of hour angle. Mueller matrices obtained from theoretical model and simulation for $HA = -60^\circ$, $DEC = 0^\circ$ are given in Eq. (2.24), and they agree to the level of 10^{-4}.

$$\mathbf{M_{CTV-Th}} = \begin{bmatrix} 1.0000 & 0.0949 & -0.0063 & -0.0018 \\ -0.0946 & -0.9852 & 0.1677 & 0.0334 \\ -0.0096 & -0.1697 & -0.9288 & -0.3156 \\ -0.0018 & -0.0220 & -0.3166 & 0.9435 \end{bmatrix}, \tag{2.24a}$$

$$\mathbf{M_{CTV-Si}} = \begin{bmatrix} 1.0000 & 0.0949 & -0.0063 & -0.0018 \\ -0.0946 & -0.9852 & 0.1677 & 0.0334 \\ -0.0097 & -0.1697 & -0.9288 & -0.3156 \\ -0.0018 & -0.0220 & -0.3166 & 0.9435 \end{bmatrix}. \tag{2.24b}$$

Using this theoretical model it is calculated that if the primary mirror position is switched, from east to west (for $HA < -45^\circ$) or west to east (for $HA > 45^\circ$), the instrumental polarization of the system reduces significantly (similar results were also noted earlier by Bachmann, 1984). The HA limitation is posed by the rigid opto-mechanical design of the KTT Coelostat. For the same $HA = -60^\circ$ and

$DEC = 0°$, Mueller matrices for the proper configuration and switched configuration are given in Eq. (2.25).

$$\mathbf{M_{C4-Prop}} = \begin{bmatrix} 1.0000 & 0.0944 & -0.0055 & -0.0017 \\ -0.0942 & -0.9875 & 0.1540 & 0.0314 \\ -0.0090 & -0.1562 & -0.9316 & -0.3142 \\ -0.0017 & -0.0193 & -0.3152 & 0.9441 \end{bmatrix}, \tag{2.25a}$$

$$\mathbf{M_{C4-Swit}} = \begin{bmatrix} 1.0000 & 0.0126 & 0.0071 & -0.0001 \\ -0.0136 & -0.9871 & -0.1593 & 0.0168 \\ -0.0050 & 0.1583 & -0.9862 & -0.0452 \\ -0.0001 & 0.0238 & -0.0420 & 0.9987 \end{bmatrix}. \tag{2.25b}$$

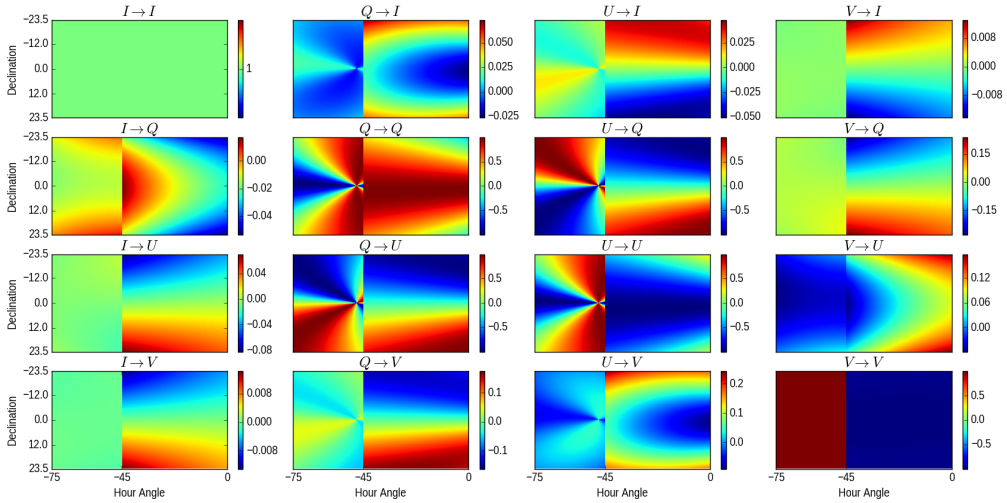

Figure 2.6: Mueller matrix corresponding to the system before the polarimeter. Note that the elements are normalized with respect to the first element (M_{00}).

The final Mueller matrix of the entire system with possible improvements, as a function of HA and DEC is mapped in Figure 2.6. The diagonal elements of the Mueller matrix correspond to the transmission of each Stokes parameter. Non-diagonal elements of first row correspond to the cross-talks from Q, U and V to the total intensity. These values are usually very low and considering the degree

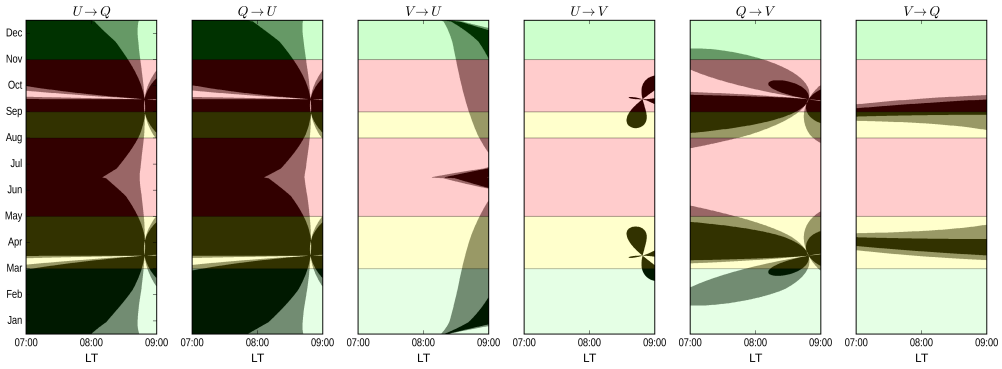

Figure 2.7: Illustration of effect of change in configuration and introduction of MSM on the key terms of instrumental polarization. Ratio of absolute values are rounded and plotted against local time on X-axis and month on Y-axis. Black colour indicates degradation, gray indicates improvement up to 2 times and white indicates improvement more than 2 times. Horizontal bands of colour indicate sky conditions. Green indicates good conditions, red indicates mostly cloudy conditions and yellow indicates the rest of intermediate conditions.

of polarization ($\sim$ 0.2 or less) in solar observations, the cross-talk becomes negligible. Non-diagonal elements of first column correspond to the cross-talks from total intensity to Q, U and V. They manifest as constant offsets in Stokes Q, U and V profiles, and to a large extent it is correctable by subtracting respective continuum polarization level from each profile. It is possible as continuum polarization in red part of optical wavelengths is expected to be close to zero (Fluri and Stenflo, 2003). Rest of the elements correspond to cross-talks from one state of polarization to the other. Figure 2.7 depicts the comparison of these elements in usual Coelostat configuration and after changing the configuration. Considering the Coelostat design, configuration can be changed only for the duration corresponding to $-75^\circ < HA < -45^\circ$. Hence, comparison for only those results are shown. The same results can be extended for $75^\circ > HA > 45^\circ$. Black shade indicates degradation, gray indicates up to 2 times improvement and white indicates more than 2 times improvement. Horizontal bands of colour indicate observing conditions at KSO in an approximate manner. Green indicates good conditions (peak winter), red indicates mostly cloudy conditions (monsoons) and yellow indicates the rest of intermediate conditions.

As it is evident, cross-talks corresponding to $Q \rightarrow V$, $U \rightarrow V$, $V \rightarrow Q$ and $V \rightarrow U$ have reduced significantly. These cross-talks manifest as distortions in the

Stokes Q, U and V profiles hence, any residuals after corrections can create hurdles in inverting those profiles to obtain magnetic field information. However, $Q \rightarrow U$ and $U \rightarrow Q$ cross-talks imply the rotation of coordinate system and residuals manifest as error in estimation of azimuth angle of the transverse magnetic field component. Hence, it was decided to adopt the improved Coelostat configuration, and MSM was placed before the modulation unit.

2.4.3 Strategy for estimating model parameters

In the present model, RI value was taken from existing literature. But, this is only for the purposes of comparing the model and simulation. For accurate estimation of instrumental polarization few more things must be considered. Mirrors are coated at in-house facility with bare Aluminium. After evaporation, an oxide layer is formed that protects the coating to certain extent (Sankarasubramanian and Venkatakrishnan, 1996). Oxide layer is also included in the present model that is to be fitted to the observations.

Profiles of five cross-talk elements ($I \rightarrow Q, U, V$ and $V \rightarrow Q, U$) of telescope Mueller matrix shall be obtained from the observations as discussed in Section 3.5.2. Sunspot with strong magnetic field closer to the disk center shall be observed continuously spanning few hours. Strong magnetic field is for high signal level, and its proximity to the disk center ensures that photospheric line-of-sight magnetic field strength at the center of sunspot is considerably greater than the transverse magnetic field strength. Continuous observations spanning few hours shall result in cross-talk profiles that are usable for fitting the model (see Skumanich et al., 1997). RI of the coating, oxide layer thickness and folding angle of MSM are the variables that need to be estimated from the fitting. Using these values, a more accurate estimate shall be obtained for the instrumental polarization.

2.5 Testing Components

Except for the PBD which is custom made, all other optical components are procured off-the-shelf. Wave plates are designed for 850 nm and have anti-reflection

(AR) coating for high throughput. They are tested for their retardance and polarizers are tested for their extinction. Fast axis of polarizing elements is also checked.

2.5.1 Polarizers

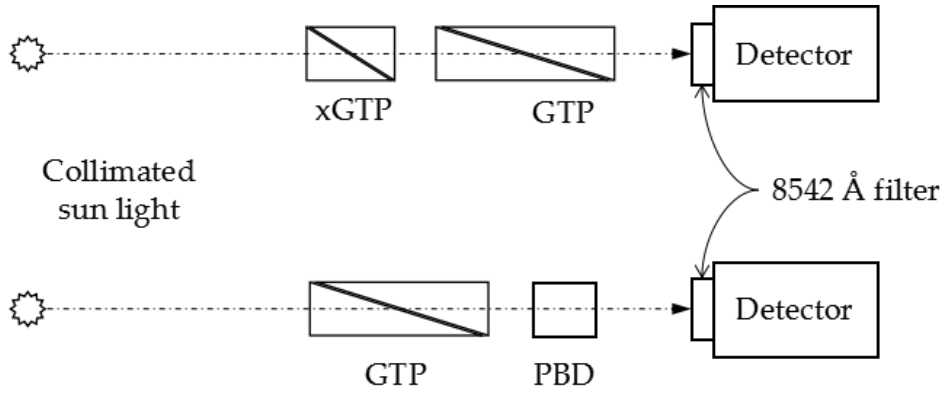

Figure 2.8: Layout of the test setup for polarizers consisting of reference polarizer (xGTP or GTP), test polarizer (GTP or PBD), filter and the detector. Collimated sunlight from the Coelostat at our lab is directly passed through the setup.

Table 2.4: Extinction values for polarizers (rounded off to the lower values).

Component	Extinction
GTP	$> 10^5$
PBD top	~ 1000
PBD bottom	~ 450

For testing GTP and PBD, a simple setup consisting of a detector and a filter is used. GTP is tested with a pre-existing Glan-Thompson Polarizer (xGTP). Sunlight is passed through xGTP and its polarized output is passed through GTP. Filter that is placed before the detector has a pass band of 1.5 Å centered at 8542 Å, and intensity corresponding to that spectral band is measured. Reference polarizer is rotated to obtain maximum and minimum intensities. The ratio of maximum to minimum intensity gives the estimate of extinction. Same exercise is repeated using top and bottom beams of the PBD. Extinction values are tabulated in 2.4.

2.5.2 Wave plates

Scanner with spectrograph setup at laboratory facility is used for testing the polarizing components. Schematic of the test setup is given in Figure 2.9. Spectrograph is set to direct 8542 Å radiation onto the detector. White light lamp in combination with pin hole provides point like source. The beam is collimated using a doublet and passed through two polarizers. One of them is GTP and the other is PBD.

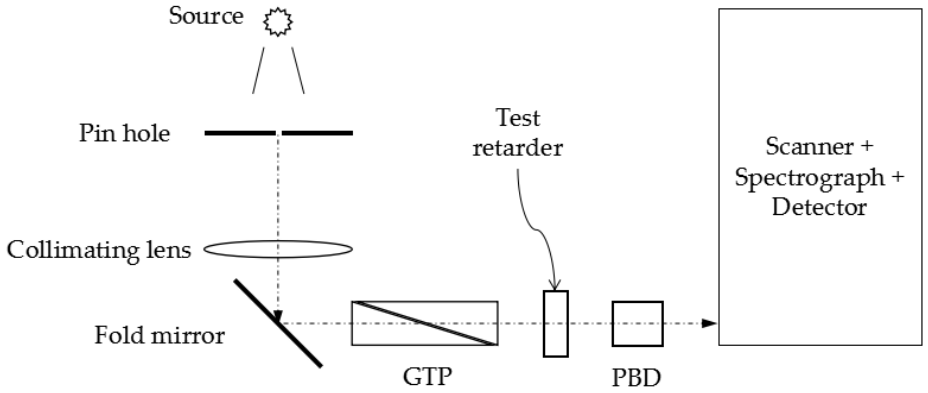

Figure 2.9: Layout of wave plate retardance test setup. High power incandescent lamp (white light) with pinhole is used as point-like source. Light from it is collimated and sent through GTP, test wave plate placed in motorized rotation mount, and analyzer (PBD top). Following that, spectrograph setup selects desired spectral range and directs the light onto the order-sorting filter followed by the detector.

Table 2.5: Retardance values of the waveplates (accurate to the level of 0.001λ).

Wave plate	Fraction of λ	Retardance
CWP	0.249	$\lambda/4.02$
QWP	0.249	$\lambda/4.02$
HWP	0.5	$\lambda/2$
AQWP	0.246	$\lambda/4.06$

First, fast axis of GTP and PBD are aligned. Then, the wave plate to be tested is introduced between them, mounted on a motorized rotation mount. It is rotated by 360° in 500 steps and spectra are recorded. Linearly polarized light is passed through wave plate and analyzed by PBD. Spectra are processed and intensity corresponding to images are integrated. Intensity versus position angle curves are

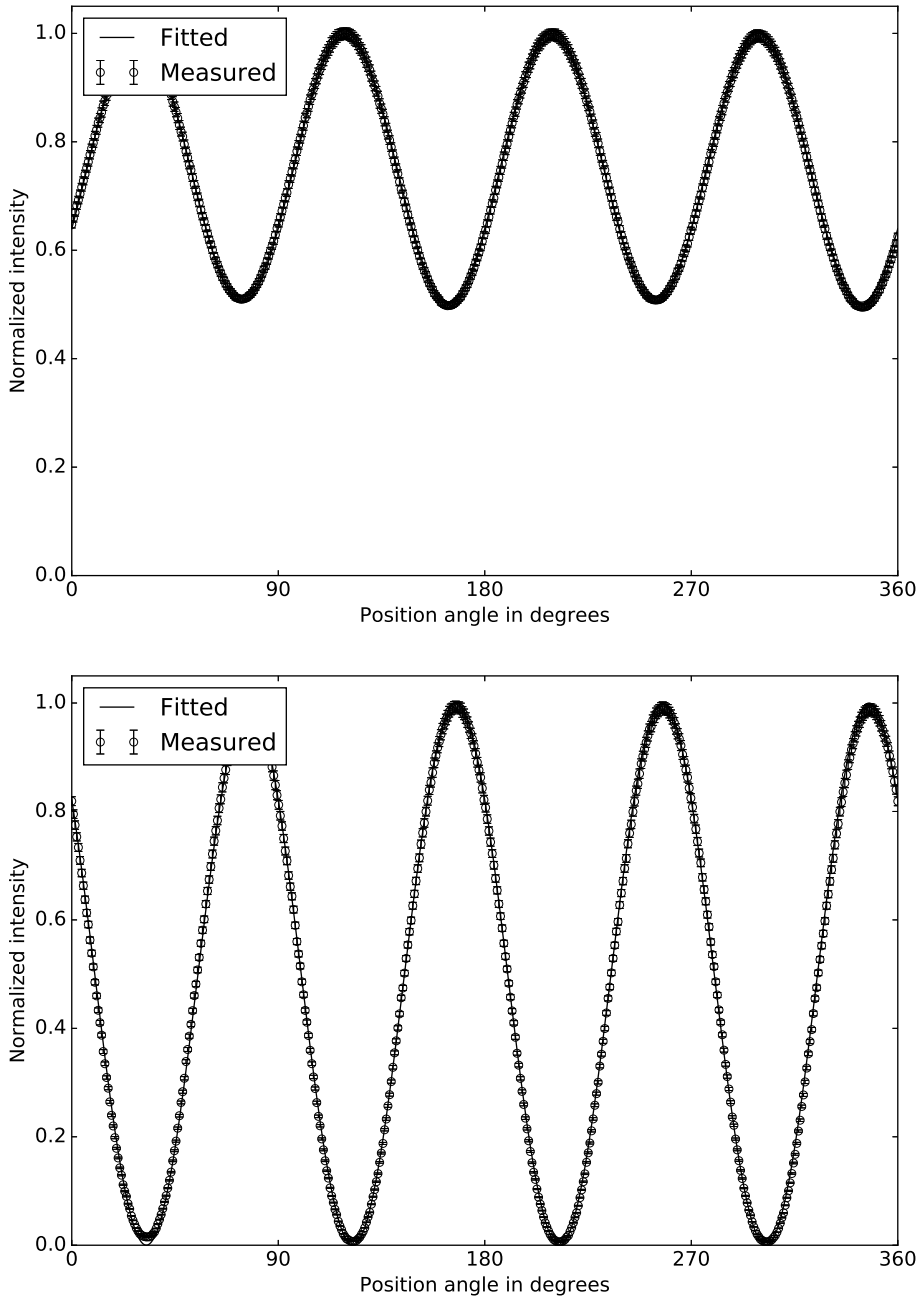

Figure 2.10: Intensity curves obtained when testing wave plates. *Top*: QWP test & *bottom*: HWP test. They are fitted with theoretical intensity curves with retardance values of 0.249λ and 0.5λ respectively.

fitted with Eq. (2.26), that is derived from of Eq. (2.5), to obtain retardance.

$$I = A(1 + cos^2 2(\theta + P) + sin^2 2(\theta + P) cos\delta). \tag{2.26}$$

where A corresponds to amplitude, P is position angle of the fast axis at the beginning and δ is retardance of the wave plate. Figure 2.10 shows such intensity plots for HWP and CWP. Retardance values for all the wave plates are listed in Table 2.5.

2.5.3 Detector

As previously stated, SSP is developed to be compatible with the existing system that includes a large format detector. It has a quantum efficiency of 50% at 8542 Å as per specifications. However, detector D1 is originally optimized for observations in blue region. Its sensor is back-illuminated and back-thinned, and anti-reflection coating is optimized for the same. Hence, we observed that it suffers from *etaloning effect*. For Silicon substrate, near infrared radiation has higher *penetration depth* compared to blue. When it enters thin substrate, it undergoes multiple internal reflections between two surfaces of the sensor substrate resulting in *fringe patterns* in the images. By means of applying anti-reflection coating on the sensor this effect may be minimized. However, this is not the case with D1. It imposes severe limitation on Signal-to-Noise Ratio (SNR) as the exposure time is dictated by the brightest fringe and SNR is dictated by the darkest fringe. It also affects flat fielding accuracy. Here, we have separately characterized fringes using *fringe flat*, that is to be used in addition to regular spectroscopic flat. Although it does not improve SNR, it helps in restoring spectral continuum more accurately. It is described in detail in the next chapter.

2.6 Summary

We have designed and developed Solar Scanning Polarimeter, and installed it at KTT to enable measurements of chromospheric magnetic fields. We have selected Ca II 8542 Å to be suitable spectral line for Zeeman diagnostics. We have identified relevant components to develop SSP that are compatible with pre-existing telescope and back-end system including the detector. SSP designed in such a way that it can map the solar features with raster scan. It is modeled to encounter lesser instrumental polarization than its predecessors. It is packaged in such a way that

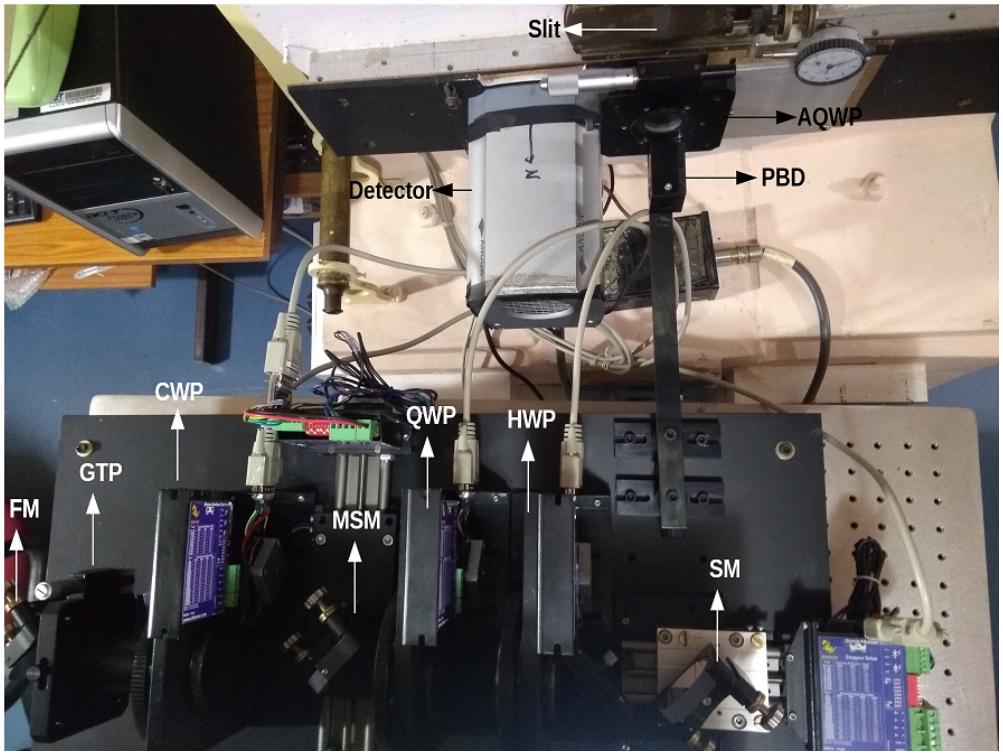

Figure 2.11: Solar scanning polarimeter, installed at back-end of KTT, before the focal plane.

it can be easily installed and uninstalled from the observing table at the telescope back-end. Figure 2.11 shows a top view of the polarimeter installed at the back-end of KTT. Objective lens rests on rails and it is moved towards focal plane to compensate for the focal shift introduced by SSP.

We devised four-step polarimetric modulation scheme that increases cadence and also gives equal efficiencies for Stokes Q, U and V measurements. We have analytically modeled one of the hurdles in polarimetry: instrumental polarization, and validated it with ZEMAX simulation. Subsequently, we have come up with a proposal to reduce it for KTT system. We have also developed customized controller and GUI based operating software for observations. We have installed aforementioned system at KTT for observations. An imaging channel is also provided for the context imaging purposes. However, SSP is flexible in the sense that there is ample provision to integrate an Image Stabilization System with it. It is discussed in Chapter 4 in greater detail.

Once SSP installed, we have acquired on-telescope calibration and observational data. However, this data need to go through extensive processing in-order to result in meaningful information. In the next chapter, we describe the process from acquiring data to producing magnetic field map of the observed region.

Chapter 3

Spectropolarimetry: Data Reduction, Calibration & Observations

3.1 Introduction

In order to measure magnetic field from spectropolarimetry, accurate measurements of Stokes parameters are required. In case of spectropolarimetry, reduction of solar spectrograms taken using slit based spectrographs in itself is extensive, one of the main challenges being flat fielding (Wöhl et al., 2002). Such spectrograms are affected by finite slit width that is required to allow sufficient light, scatter light caused by spectrograph optics, and misalignments among slit, grating and the detector. Apart from it, polarimetric calibration is required to characterize the optics that encounter light path as its state of polarization is sensitive to any changes in the media (Born and Wolf, 1999, Section 1.5). This requires extensive study and calibration of the instrument as well as the telescope.

Many times, such characterization is done by sending input light of well known SoP through the optical system and obtaining SoP of the output. In case of compact space-based telescopes, these experiments were done in laboratory (e.g., Schou et al., 2012). In ground-based facilities with relatively bigger telescopes, specialized setups were developed for polarimetric calibration, with sunlight being the source.

Such specialized setups consisting of polarizing optics were placed before the telescope entrance aperture, and part of telescope's *response* was measured aided by modeling (e.g., Beck et al., 2005a). Rest of the telescope optics' response was measured by introducing a *calibration unit* before those optics. Some telescope systems were designed in such a way that axially symmetric telescope optics were immediately followed by polarimetric calibration unit, to ensure that minimal cross-talks are introduced before light enters the calibration unit (e.g., Ichimoto et al., 2008). Rarely, polarimetric cross-talks relevant to observations were computed from the observed data themselves and Stokes parameters were corrected (Sanchez Almeida and Lites, 1992; Kuhn et al., 1994; Collados, 2003). At KTT, Sankarasubramanian et al. (1999) have estimated telescope's response by measuring refractive index of the mirror coatings and plugging it in theoretical model of telescope's instrumental polarization (Balasubramaniam et al., 1985). Solar scanning polarimeter's design is modeled to reduce some polarization cross-talks relevant to active region observations. However, we have not used this modeling results in present observations as mirror coating parameters are not estimated yet. Instead, we have computed relevant cross-talks from the observational data and corrected the Stokes parameters.

We have designed, developed and installed the solar scanning polarimeter at KTT of KSO, aiming towards producing chromospheric vector magnetograms. In order to enable the construction of accurate magnetograms, various types of data are required for the purposes of correcting previously described effects. Once such data are acquired, they must be reduced and various corrections must be applied to acquire polarized line profiles i.e., Stokes profiles. In the present chapter, we introduce data acquisition with the description of various types of data. Further, we outline data reduction procedure, applied corrections and estimation of various parameters. Finally, we present the magnetogram that is constructed from the data.

3.2 Data Acquisition

A complete data set required to construct magnetogram, using SSP observations, consists of five types of data frames: 1) Dark frames, 2) Flat frames, 3) Fringe flat frames, 4) Calibration data and 5) Observational data. Respective modes in observing software are used to acquire aforementioned data and they are saved as level-0 raw data. Note that the sunlight enters SSP through the observation port for all the modes except calibration mode, and this operation is performed manually.

3.2.1 Dark frames

Dark frames account for the *bias* and *thermal electron* counts' contribution in the acquisition. Bias is an offset value that is electronically introduced at the time of frame readout to make counts non-zero. Apart from photo-electrons, thermal agitation of electrons gives rise to *thermal noise* or *dark noise*. Dark frames are obtained by blocking the illumination on the detector by closing the slit. It also accounts for ambient light, if any.

3.2.2 Flat frames

Flat frames account for the pixels' response of the detector for a uniform illumination. But, as it stands, there are difficulties in solar spectrograph based observations when it comes to obtaining flat frames. Strong spectrally flat source is required to illuminate the detector uniformly. Hence, the solar illumination itself is used for the flats. Solar spectra is full of absorption lines making it spectrally not flat. It is a common practice to smear out spatial features in 2-D spectral frame during the acquisition and remove spectral features while processing (Wöhl et al., 2002). Flat frames are acquired by placing the solar disk center on the slit and moving it randomly. This results in capturing spectra with smeared spatial features.

3.2.3 Fringe flat frames

As stated in Section 2.5.3, fringe flat frames are specific to the present detector and wavelength of observation. It represents only the fringes caused by etaloning effect and it is devoid of any other spectral features. They are acquired in a similar manner to flat frames with two key differences: (1) Third order is selected instead of second order, (2) Instead of spectral line nearby continuum is selected. As we need fringes caused by etaloning effect but without any spectral lines, we have selected higher order spectrum. As wavelength coverage is low in higher order, it is easier to find a spectral region near to 8542 Å with no lines present. Changing the wavelength to nearby continuum would not have any significant effect on fringe pattern as it is specific to wavelength and sensor chip. Although this ensures that there are no spectral lines, there is still intensity gradient across the image, and that is taken care in the processing.

3.2.4 Calibration data

For calibration data acquisition, we move the solar image so that light enters SSP through calibration port. Calibration data consist of $m \times n$ frames, m being the number of steps in modulation and n being the number of known input states of polarization. A minimum of four (n) distinct known input states should be used. Here, a total of 24 known states are generated using the calibration unit, and polarimetry is performed. As mentioned in Section 2.3.1, these states are produced by rotating the CWP in equal steps (7.5°) totaling 180 degrees.

3.2.5 Observational data

For calibration data acquisition, we move the solar image so that the light enters SSP through the observation port and center of the observing feature is placed exactly on the slit. Observational data consist of $m \times k$ frames where k is the number of slit positions across the image. For each slit position on the image four stepped modulation is implemented, and image is moved across the slit cycling through this process.

3.3 Data Reduction

After acquisition, raw data must be reduced to get full Stokes profiles. Flowchart shown in Figure 3.1 depicts steps involved in reduction. The process is interactive to provide certain inputs and verify the reduction process at various stages. It is implemented in Python programming language. Each process and its functions are outlined in current and subsequent sections.

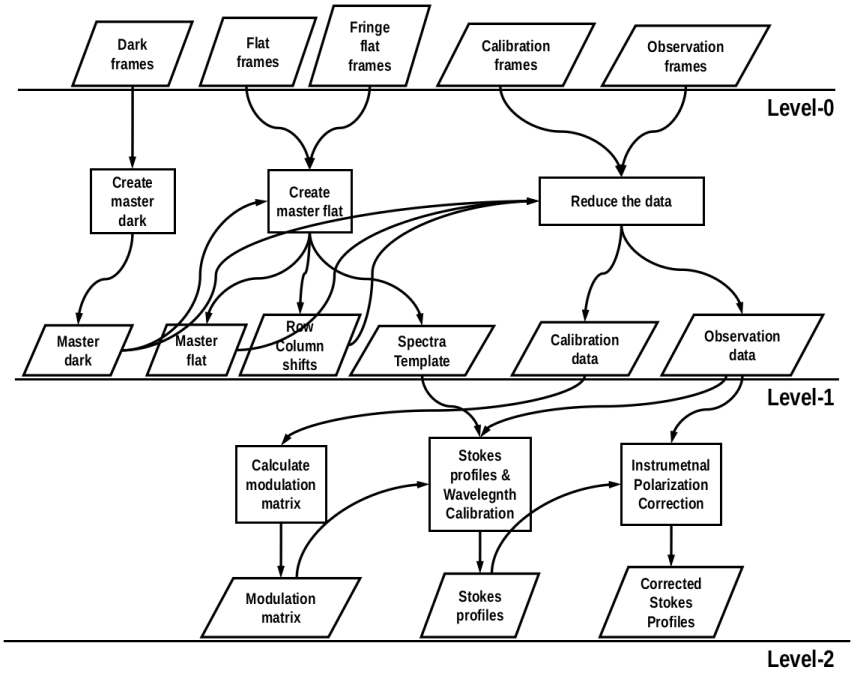

Figure 3.1: Flow of the steps involved in reduction of SSP spectropolarimetric data. They are executed in the same order that is depicted : first from top left to bottom right in the end.

3.3.1 Master dark & master fringe flat

All the dark frames are averaged to produce mean dark. A median filter with 3×3 window is applied. Median filtering removes any spurious *hot/cold* pixels. They are isolated pixels with unusually high/low counts.

For master fringe flat, fringe flat frames are averaged and normalized. Intensity gradient across the mean fringe flat is detected. From the top beam, random pixels

from bright fringe region are selected and their intensity is plotted against their x-position. A quadratic equation is fitted to the plot and the fit is converted into a 2-D intensity mask. Mean fringe flat is then divided with this mask resulting in master fringe flat. This process is depicted in Figure 3.2.

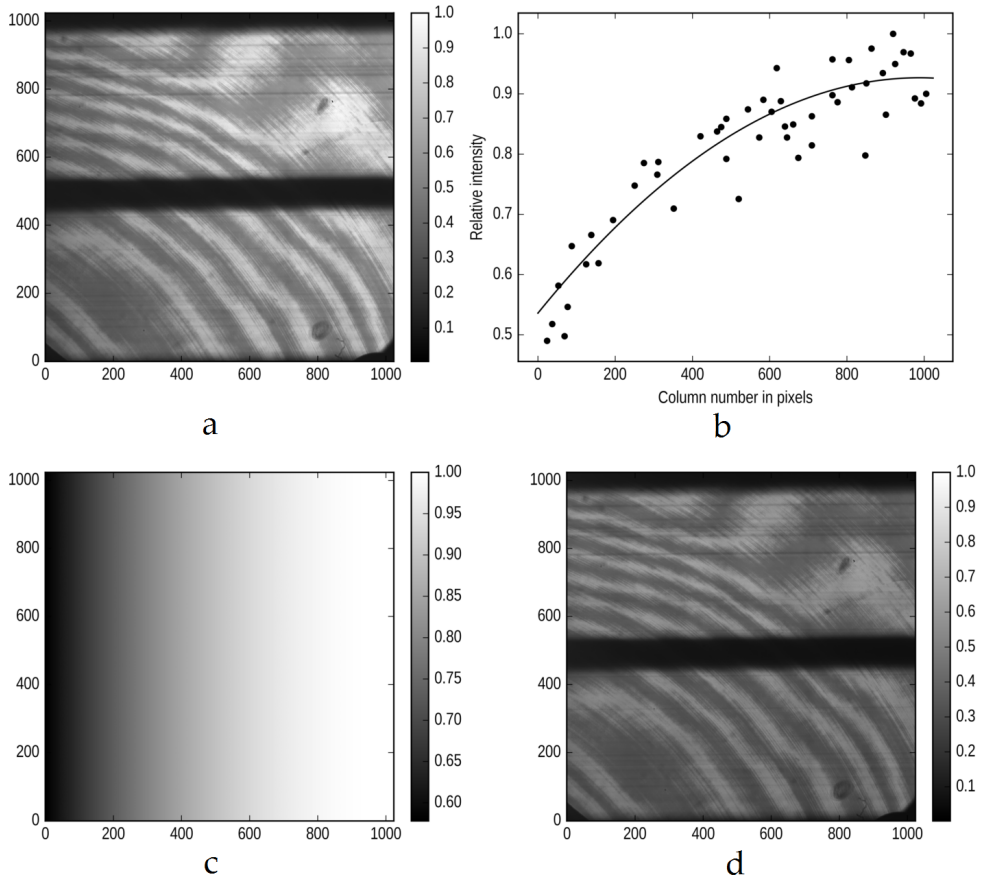

Figure 3.2: Process of creating master fringe flat. Intensity gradient across mean fringe flat (a) is plotted and fitted with quadratic equation (b). A mask (c) is created from this equation and mean fringe flat is divided by this mask to get master fringe flat (d).

3.3.2 Master flat

For the master flat, procedure described in Wöhl et al. (2002) is followed with a few modifications. First, all the flat frames are averaged. Then, mean flat must be aligned in such a way that the spectral and spatial axes are along the detector axes. To do so, three corrections are required: 1) X inclination, 2) Y inclination,

and 3) Y curvature. They are caused due to a combination of distortion caused by optics, slit and detector reference axis not being parallel, and slit and grating grooves not being parallel. As the effects of these misalignments are very small in amount compared to the detector size, they are corrected by shifting columns and rows respectively. To correct X inclination, a slit pattern (formed due to non-uniformity of the slit or some obstruction on the slit) with good contrast is selected and traced across the detector. A line is fitted to this trace and each column is shifted by the amount given by that linear equation.

Before correcting for the Y inclination, mean flat is divided by master fringe flat to which the same column shifts were applied. This results in reduced fringe contrast. Earth's atmospheric line at 8540.7 Å is traced and a quadratic equation is fitted to it to get both Y inclination and curvature. All the rows are shifted by the amounts given by this equation. Correcting the mean flat for the inclinations results in the spectral line being aligned vertically. Figure 3.3 illustrates tracing of slit and spectral line features, and corresponding column and row shifts. Row and column shift values required to align the images are saved as level-1 data so as to be used in further reduction.

At this point, spectral line is aligned vertically. Pristine line profiles are selected from beam centers and column-wise medians are computed. This profile is smoothed by a Gaussian filter to reduce spurious pixel-to-pixel variation. Each row of the aligned mean flat is divided by smoothed line profile, thus creating the master flat. Median spectrum acts as a template (henceforth referred as *template* spectrum), and it contains information regarding various characteristics of the instrument. It is saved for wavelength calibration, and estimating instrumental broadening and stray light. Raw flat frame and master flat are compared in Figure 3.4.

3.3.3 Instrumental effects & wavelength calibration

Template spectrum is used to estimate various parameters that characterize the instrument. High resolution solar spectrum with $\Delta\lambda$ = 0.001 Å is obtained from

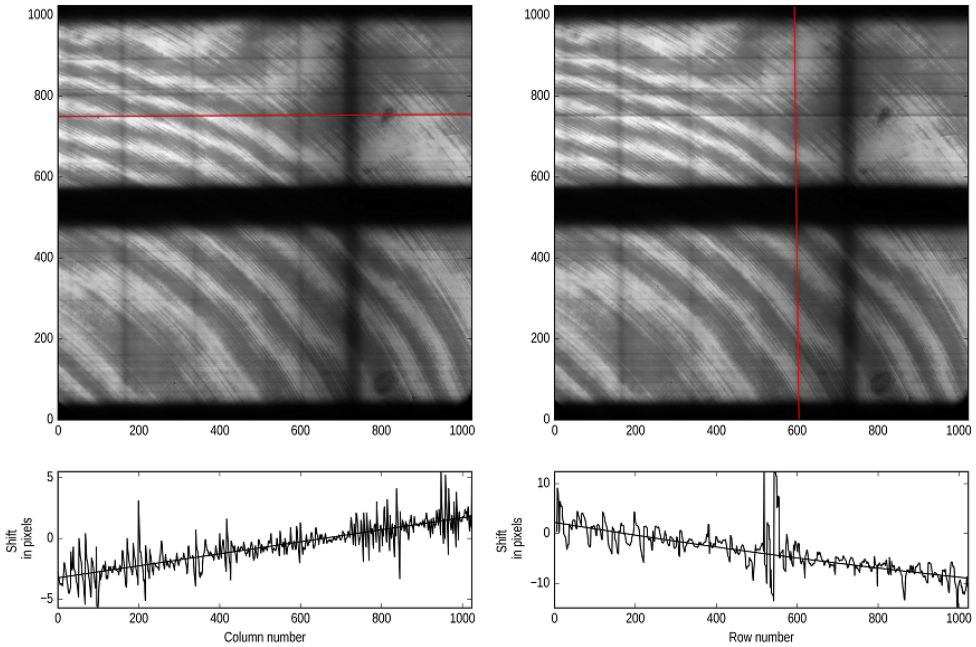

Figure 3.3: *Top-left*: slit feature trace, *bottom-left*: column shift values for each row, *top-right*: line profile trace, and *bottom-right*: row shift values for each column.

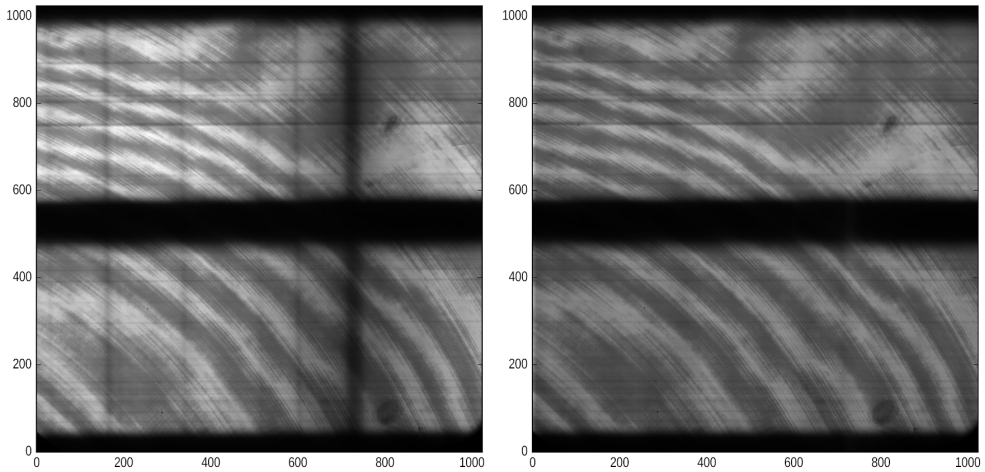

Figure 3.4: *Left*: raw flat after acquisition, and *right*: master flat.

Delbouille et al. (1973) (henceforth referred as catalog spectrum). Catalog spectrum is broadened with Gaussian kernel and normalized so as to match with template spectrum. Figure 3.5 shows comparison for $\sigma = 2.5$ pixels. Correspondingly, instrumental broadening is calculated to be 54 mÅ. If we examine closely, we see that the

line core is raised in the case of template spectrum as compared to broadened catalog spectrum, which can be due to spectral stray light (if so, it is $\sim$ 2%). However, due to prevailing flat fielding errors (sometimes up to $\sim$ 5%) that can be seen in template spectrum, stray light estimate would not be accurate.

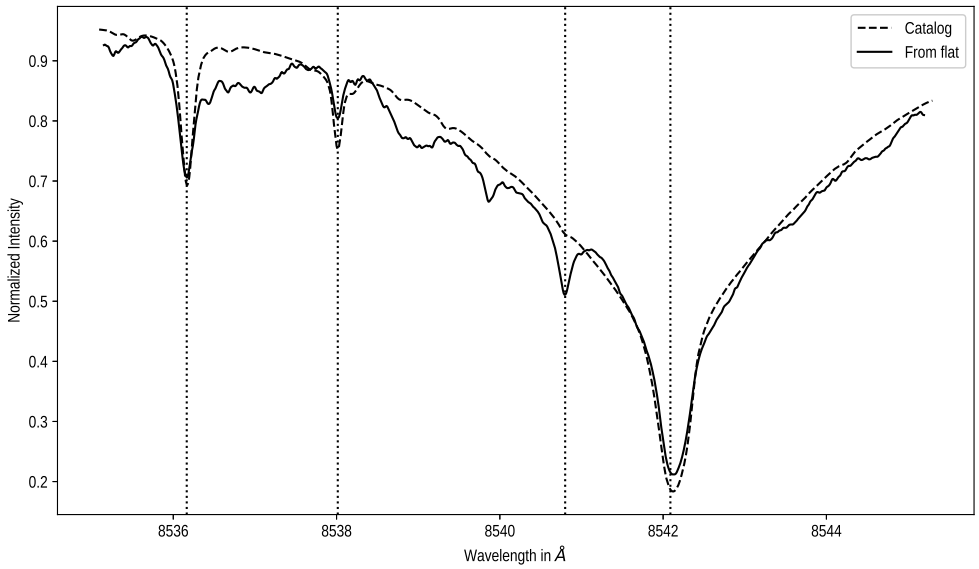

Figure 3.5: Spectrum obtained from the disk center over-plotted with the catalog spectrum (Delbouille et al., 1973) that is convolved with a Gaussian profile of σ = 2.5 pixels.

We have identified four absorption lines in template spectrum: one atmospheric and three solar lines. Gaussian profiles are fitted to central core in order to compute their position with sub-pixel accuracy. Absolute reference position for Ca II line is also computed. Spectral plate scale is calculated to be 10.8 mÅ/pixel and it matches with expected value.

3.3.4 Dark & flat corrections

After synthesizing master dark and master flat, and estimating row and column shifts, calibration data and observational data frames must be corrected. Master dark is subtracted from all the frames. Row and column shifts are applied and subsequently all the images are divided by master flat. Figure 3.6 shows a sample raw frame before and after correction.

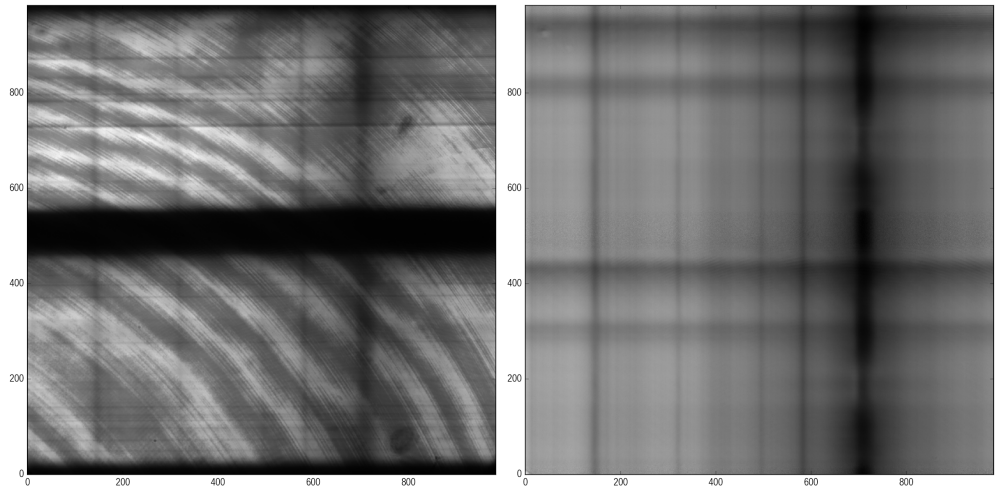

Figure 3.6: *Left*: raw data frame, and *right*: corrected data frame.

3.4 Polarimetric Calibration

Polarimeter is characterized by its modulation matrix **O**. Polarimetric calibration is the process of experimentally estimating **O**. It is achieved by performing polarimetry on the light of known state of polarization. Once **O** is obtained, its pseudo-inverse is computed to obtain **D**, which is used with observational data to extract Stokes parameters.

3.4.1 Modulation matrix

Level-1 calibrated data are used to calculate modulation matrix. A Region of Interest (RoI) away from the solar spectral lines is selected in both top and bottom beams. Intensity from this RoI is integrated and plotted against position angle of calibration wave plate. From such data, modulation matrix is computed by using Eq. (2.8). Eq. (3.1) gives modulation matrices for both top and bottom beams with

error estimations.

$$\mathbf{O_{top}} = \begin{bmatrix} 1.0 & 0.560 & 0.450 & 0.589 \\ 1.0 & -0.532 & 0.599 & 0.557 \\ 1.0 & 0.488 & 0.604 & -0.513 \\ 1.0 & -0.577 & -0.508 & -0.612 \end{bmatrix} \pm \begin{bmatrix} 0 & 0.006 & 0.005 & 0.003 \\ 0 & 0.004 & 0.004 & 0.003 \\ 0 & 0.006 & 0.007 & 0.003 \\ 0 & 0.004 & 0.005 & 0.003 \end{bmatrix}, \quad (3.1a)$$

$$\mathbf{O_{bot}} = \begin{bmatrix} 1.0 & -0.591 & 0.528 & -0.570 \\ 1.0 & 0.523 & -0.537 & -0.570 \\ 1.0 & -0.553 & -0.567 & 0.577 \\ 1.0 & 0.508 & 0.538 & 0.571 \end{bmatrix} \pm \begin{bmatrix} 0 & 0.004 & 0.005 & 0.003 \\ 0 & 0.006 & 0.007 & 0.004 \\ 0 & 0.004 & 0.004 & 0.003 \\ 0 & 0.005 & 0.005 & 0.003 \end{bmatrix}. \quad (3.1b)$$

As MSM and DBS also fall in the path of beam, measured **O** deviates from the theoretical one i.e., the one calculated for the combination of QWP and HWP. Optimum demodulation matrix **D** is calculated according to Eq. (2.7) and result is given in Eq. (3.2).

D is applied to level-1 calibration data to retrieve known input SoP. They are compared with the calculated input values. This process is iteratively performed to identify and exclude the outliers, and retrieve the position angle offset for CWP. Figure 3.7 shows the retrieved input Stokes parameters after modulating and subsequently demodulating the input, and they are compared with actual input.

$$\mathbf{D_{top}} = \begin{bmatrix} 0.284 & 0.213 & 0.230 & 0.273 \\ 0.452 & -0.504 & 0.478 & -0.425 \\ -0.471 & 0.442 & 0.483 & -0.455 \\ 0.428 & 0.456 & -0.476 & -0.408 \end{bmatrix} \pm \begin{bmatrix} 0.003 & 0.003 & 0.004 & 0.003 \\ 0.006 & 0.006 & 0.007 & 0.006 \\ 0.006 & 0.006 & 0.007 & 0.006 \\ 0.006 & 0.006 & 0.006 & 0.006 \end{bmatrix}, \quad (3.2a)$$

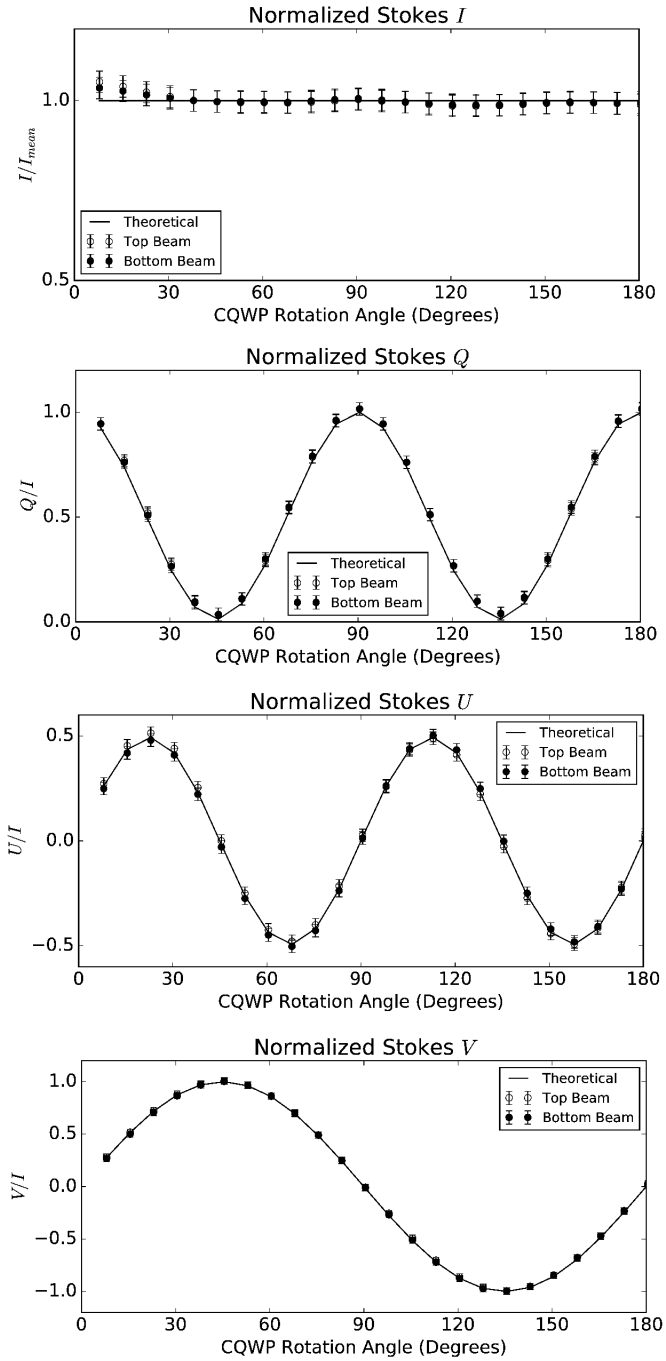

Figure 3.7: Stokes parameters obtained after demodulating PBD outputs. We see that most of the retrieved values for both top and bottom beams overlap. Maximum difference between theoretical and measured curves is ~ 0.03 (for Q) or less.

$$\mathbf{D_{bot}} = \begin{bmatrix} 0.242 & 0.260 & 0.232 & 0.266 \\ -0.469 & 0.467 & -0.450 & 0.452 \\ 0.448 & -0.451 & -0.471 & 0.473 \\ -0.429 & -0.446 & 0.437 & 0.437 \end{bmatrix} \pm \begin{bmatrix} 0.003 & 0.003 & 0.003 & 0.003 \\ 0.006 & 0.006 & 0.006 & 0.006 \\ 0.006 & 0.006 & 0.006 & 0.006 \\ 0.006 & 0.006 & 0.006 & 0.006 \end{bmatrix}. \tag{3.2b}$$

3.4.2 Polarimetric accuracy

Polarimetric accuracy characterizes the deviation in the computed Stokes profiles from actual Stokes profiles. It is estimated from errors in **D**. Sources of such errors are : 1) Input intensity variation, 2) Error in CWP retardance estimation and 3) Error in CWP position angle estimation. Their impact on errors is given in Table 3.1.

Table 3.1: Impact of various parameters on polarimetric accuracy

Parameter	Error in estimation	Impact on **O**
CWP position angle	0.1	fitted
CWP retardance measurement	$< \lambda/100$	<0.1%
Input intensity variation	$\sim$1%	$\sim$1%

The source of random errors that is, intensity variation is dominating factor in determining polarimetric accuracy in this case. This is propagated to estimate errors in **O**. *Monte-carlo* method is used to estimate error propagated to **D**. Subsequently, polarimetric accuracy is estimated to be better than 3×10^{-2}. This also reflects in the difference between given and measured input Stokes parameters for calibration, as depicted in Figure 3.7.

3.5 Sunspot Observations

A set of sunspots from the active region NOAA 12706 was observed on April 26, 2018, using SSP. Figure 3.8 shows its white light image and magnetogram as observed from HMI/SDO (Schou et al., 2012), obtained from `solarmonitor.org`.

At the time of observations its latitude and longitude were 3° North and 13° West respectively, with cosine of *heliocentric angle* $\mu = 0.96$. It is a type-β sunspot group of Hale classification (Hale et al., 1919) with clearly separated magnetic polarities. It did one disk passage and did not produce any flares.

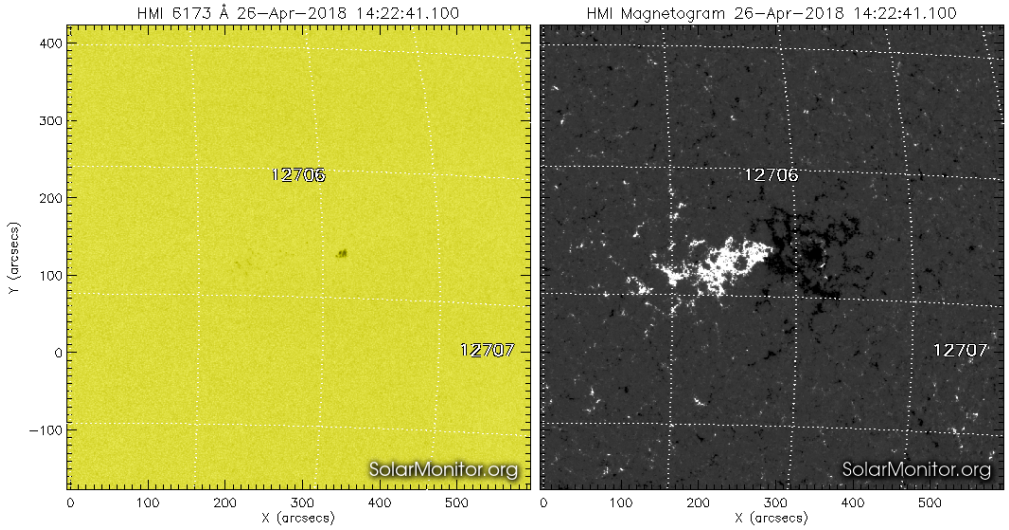

Figure 3.8: Active region NOAA 12706 as observed by HMI/SDO on the same day of present observations. Images on the *left* and *right* panels correspond to continuum image and LoS magnetogram respectively.

A region of 36 arcsec covering part of sunspot group was scanned in 60 steps (0.6 arcsec per step) in approximately 14 minutes. As part of reduction, observational data are corrected for dark, aligned using saved row and column shift values, and flat fielded. They are saved as level-1 observational data. Each of these data frames is a linear combination of Stokes parameters. Next, **D** is applied to top and bottom beams separately for level-1 observational data to compute the Stokes profiles. Resulting Stokes profiles suffer from three main problems: 1) Seeing induced cross-talk, 2) Instrumental polarization and 3) Periodic fringes.

3.5.1 Seeing induced cross-talk

As mentioned in Section 2.3.1, PBD is used as analyzer to reduce seeing induced cross-talk from $I \rightarrow Q, U, V$. It is done by combining Stokes parameters from top and bottom beams. Intensity raster images taken from top and bottom beams in

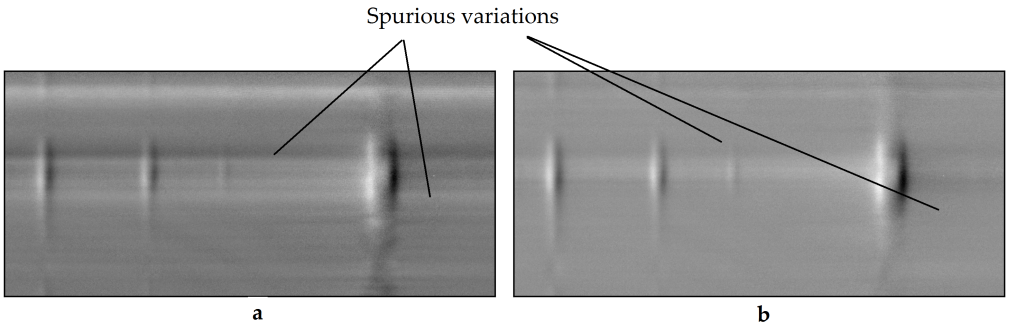

Figure 3.9: (a) Single beam versus (b) Combined beam polarized spectrum. It can be seen that dark and bright horizontal lines have disappeared after co-adding the beams which signifies reduction in seeing-induced cross-talk.

spectral continuum are correlated to align the beams. For Stokes I, intensities from both the beams are added and normalized. For Stokes Q, U and V, normalized Stokes profiles from both beams are averaged. Figure 3.9 shows V/I spectra in bottom beam and combined beam. As it can be seen, spurious variations are reduced drastically.

3.5.2 Instrumental polarization

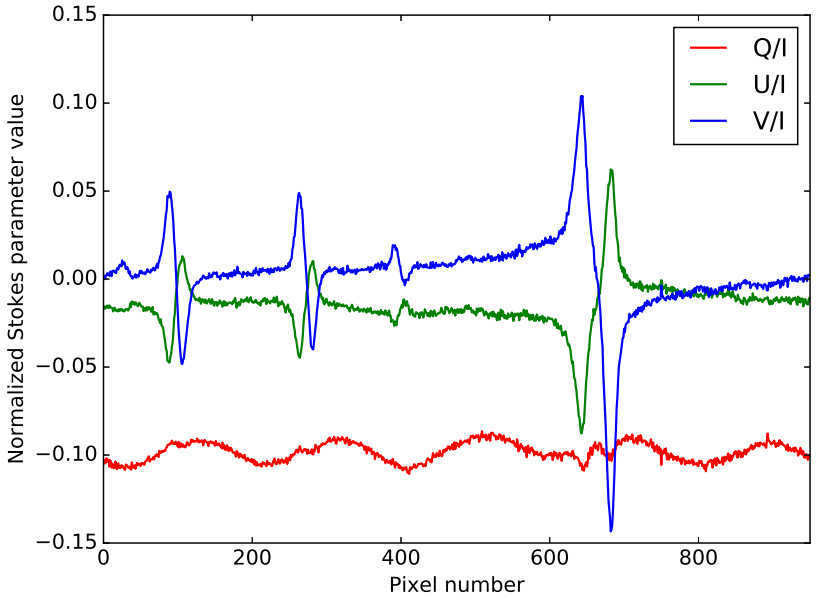

Figure 3.10: Uncorrected Stokes profiles obtained after demodulation and co-adding the beams.

Figure 3.10 shows Stokes profiles corresponding to a region closer to sunspot umbra. By looking at these profiles we make following observations:

1. Each profile is off-set from zero with a different value. This is due to $I \rightarrow Q, U, V$ cross-talks.

2. U and V profiles look very similar but inverted. This is due to a strong $V \rightarrow U$ cross-talk, as V is expected to be an order of magnitude higher than U.

3. Strong periodic fringes are present in Q along spectral direction. This could be the spectral response of one of the components in polarimeter. It is most likely AQWP as only it has broadband AR coating and every other component has 854 nm AR coating.

The final step in the processing is to remove cross-talks due to instrumental polarization. $Q \rightarrow I$, $U \rightarrow I$ and $V \rightarrow I$ cross-talks are ignored as significant portion of the light would be unpolarized and the contribution from these terms would affect the total intensity in the order of 0.1%. $I \rightarrow Q$, $I \rightarrow U$ and $I \rightarrow V$ manifest as offsets from zero in Q/I, U/I and V/I profiles. These are usually computed by identifying the continuum level. But, considering the broad nature of spectral line, it is difficult to identify the continuum level. Hence, they are estimated by applying Fourier transform to each of normalized Stokes profiles and calculating the contribution from near-zero frequency component, for each spatial location. Histograms of Mueller matrix elements corresponding to $I \rightarrow Q, U, V$ cross-talks (Section 2.4) are shown in Figure 3.11, and their values are given in Eq. (3.3).

$$M_{I \rightarrow Q} = -0.095 \pm 0.004, \tag{3.3a}$$

$$M_{I \rightarrow U} = -0.013 \pm 0.004, \tag{3.3b}$$

$$M_{I \rightarrow V} = -0.007 \pm 0.003. \tag{3.3c}$$

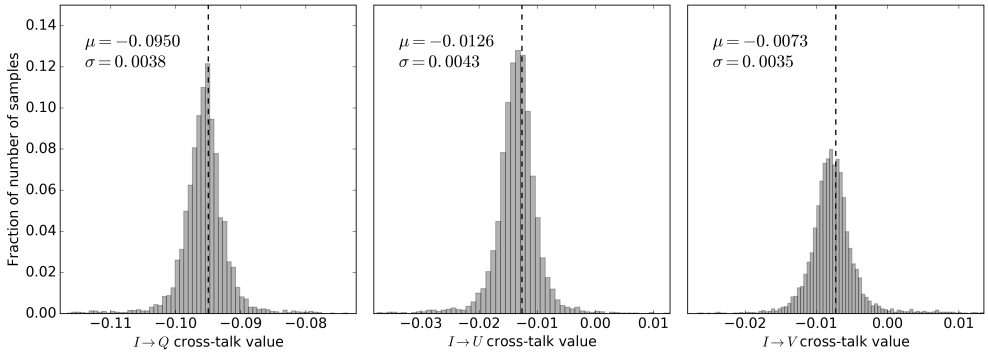

Figure 3.11: Histograms of $I \to Q, U, V$ cross-talks.

To find out rest of the cross-talk terms, analysis given in Sanchez Almeida and Lites (1992) is followed with minor modifications as outlined below. $Q \to V$, $U \to V$ are ignored as there are no parts of image with $Q >> V$ or $U >> V$. To compute $V \to Q$ and $V \to U$ cross-talks, Stokes profiles of photospheric lines (Si I 8536 Å and Fe I 8538 Å) from sunspot's umbra region are considered. They typically have strong V, and several times weaker Q and U components. From data, these Q and U signals above 3σ noise level are plotted against V signal from the same spectral line position and straight lines are fitted to them. Such fit to estimate $V \to U$ is shown in Figure 3.12.

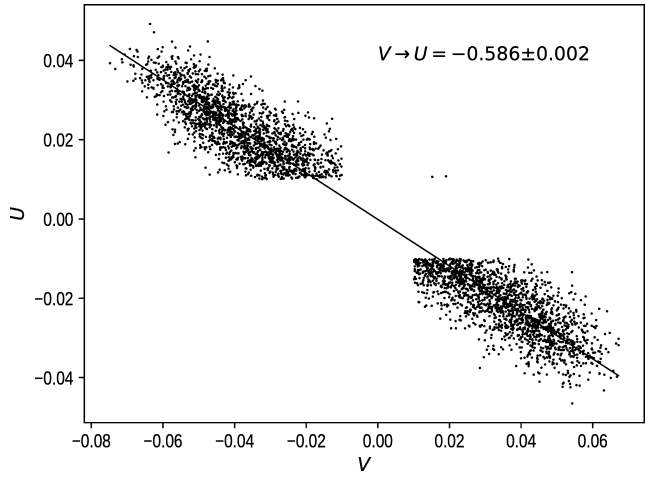

Figure 3.12: Normalized Stokes U versus V taken from photospheric lines (Si I 8536 Å and Fe I 8538 Å) in the region of sunspot umbra. Values below 3σ of noise (0.1) are not considered.

Slopes of the lines give $V \to Q$ and $V \to U$ cross-talk values. There is not

enough signal to compute $V \rightarrow Q$ cross-talk reliably, however $V \rightarrow U$ cross-talk is computed to be $M_{V \rightarrow U} = -0.584 \pm 0.002$.

Fringes in Q/I are removed by applying a high-pass filter in Fourier domain. A filter is devised to specifically eliminate these components and it is applied. Final corrected Stokes profiles are given in Figure 3.13. Resultants are saved as level-2 data.

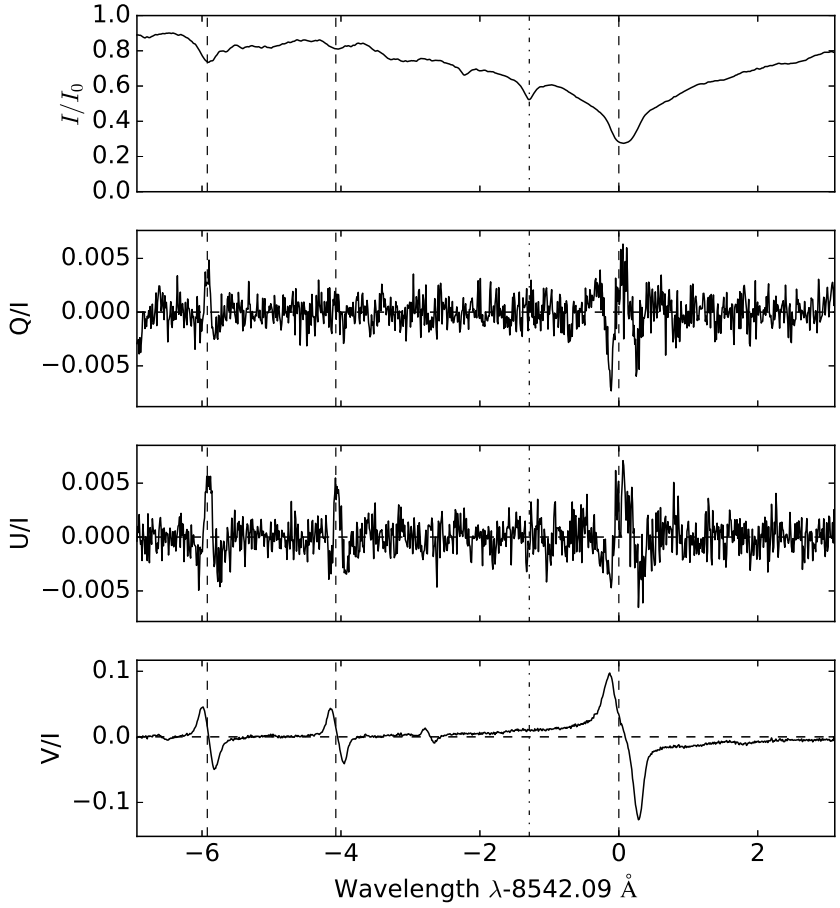

Figure 3.13: Final corrected Stokes profiles taken from 4×4 pixel region towards edge of sunspot umbra. Noise in the normalized Q, U and V profiles is measured to be $\sim 10^{-3}$. It can be seen that the characteristic Stokes Q and U profiles with amplitudes of 3–5$\times 10^{-3}$ are extracted.

3.5.3 Polarimetric sensitivity

Polarimetric sensitivity is a minimum detectable polarization signal or noise equivalent signal in normalized Stokes profiles. It is estimated from the normalized Stokes profiles, similar to the ones shown in Figure 3.13. RMS value of Q/I and U/I from spectral continuum region are estimated to be the noise power. This is mainly stemming due to photon noise and flat field error. As a fraction of intensity it is calculated to be 3×10^{-3}/pixel which is reasonably good for the active region magnetic field measurements. This figure can be improved with a better detector. Using detectors that do not have etaloning effect will simultaneously reduce photon noise and flat fielding errors.

3.5.4 Reconstructed image

We have also obtained context images for the region of interest by placing another detector (ID) in the imaging channel. A broadband green filter with $\lambda(\Delta\lambda)$ = 500 nm (10 nm) in conjunction with neutral density filters is used for the imaging. Raw images are acquired with 0.15″/pixel plate scale and 100 ms exposure time. Dark and flat frames are also acquired, and dark subtraction and flat fielding are applied to the raw images. Figure 3.14 shows the image that is captured in the imaging channel.

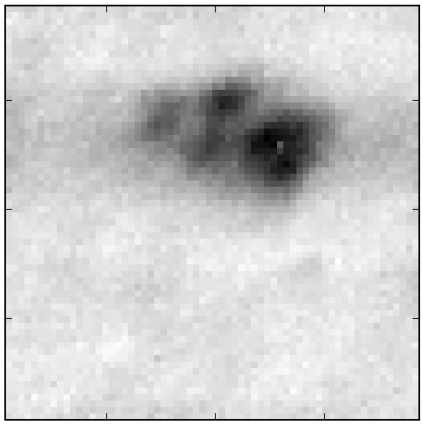

Figure 3.14: Context image obtained from the imaging channel of solar scanning polarimeter.

Final data product of SSP after processing is a 4-D array consisting of four 3-D arrays corresponding to each of the Stokes parameters. Each 3-D array has two spatial and one spectral dimension. Array slice from spatial dimensions gives raster image of region of observation. Figure 3.15 shows the raster image constructed with Stokes-I data away from the line core (left) and from the line core (middle). Corresponding field-of-view in the continuum image as seen by HMI/SDO is also shown along side (right). It shows large scale features such as fragmented sunspots and light bridge are captured. Raster image is blurred due to image motion induced by open loop tracking and seeing. Low contrast horizontal and vertical stripes are also noticed in the image. Horizontal stripes most likely are residuals from data processing, and vertical stripes are due to a combination of image motion and coarse scan step.

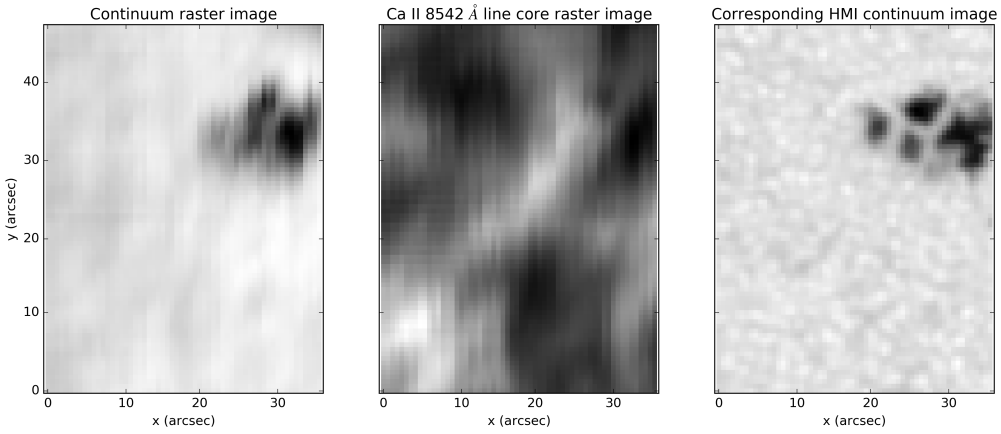

Figure 3.15: *Left image*: raster image obtained from SSP data in continuum, *middle image*: raster image obtained from SSP data in Ca II 8542 Å line core, and *right image*: region of interest taken from HMI continuum image, corresponding to SSP raster image.

3.5.5 Magnetogram construction

Once full Stokes spectral profiles for all the spatial locations are extracted, corresponding magnetic field map is constructed by using theory of radiative transfer in magnetized atmosphere. We have used Weak Field Approximation (WFA; Sanchez et al., 1992) to obtain crude estimate of field strength. Eq. (3.4) shows equations corresponding WFA to compute line of sight field strength, transverse field strength

and azimuth angle. Although it makes assumptions such as Zeeman split is much smaller compared to velocity broadening (applicable to weak magnetic fields) and constant velocity and magnetic field strength in the LoS direction (applicable only if a thin layer in the atmosphere is considered), it is successfully applied to a number of scenarios to quickly estimate magnetic field, especially in the chromosphere (Centeno, 2018). Figure 3.16 shows LoS magnetogram of observed region (left) obtained by applying WFA. Photospheric LoS magnetogram for the same region as obtained by HMI/SDO is shown alongside (right). Q and U signals are too noisy to get any meaningful estimates of transverse component and azimuth angle of magnetic field.

$$
\begin{aligned}
Bcos\gamma &= \frac{2.1 \times 10^{12}}{g_L \lambda^2} \frac{V}{dI/d\lambda} \\
Bsin\gamma &= \frac{2.5 \times 10^{12}}{g_L \lambda^2} \left[\frac{\Delta\lambda (Q^2 + U^2)^{1/2}}{dI/d\lambda} \right]^{1/2} \\
tan2\chi &= U/Q
\end{aligned}
\tag{3.4}
$$

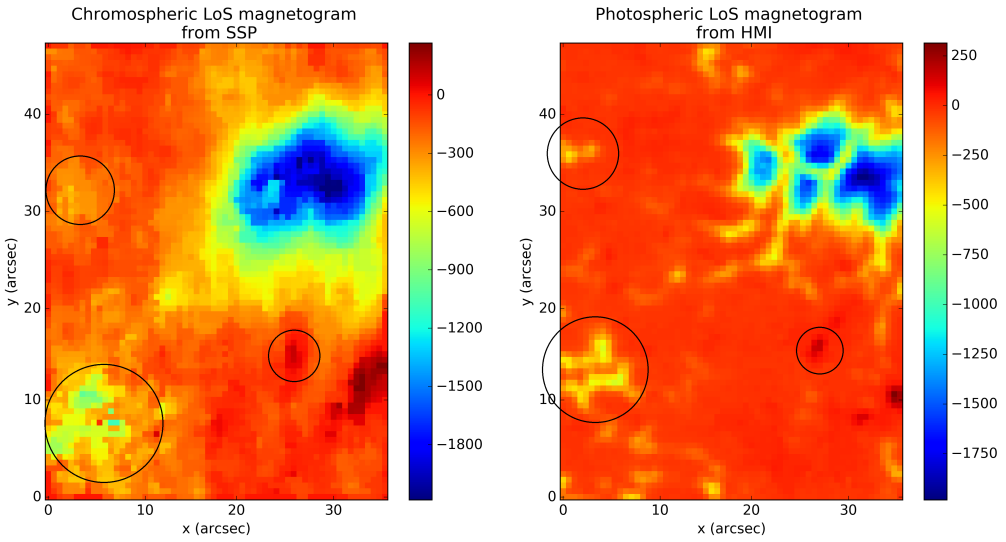

Figure 3.16: *Left*: chromospheric LoS magnetogram obtained from SSP data, and *right*: photospheric LoS magnetogram by HMI.

Figure 3.16 shows qualitative comparison of chromospheric magnetogram obtained by SSP (Ca II 8542 Å) with photospheric magnetogram for the same region obtained by HMI (Fe I 6173 Å). Encircled regions show some of the spatially finer features that are captured in both the magnetograms. Although these features are detected, they are not spatially corresponding with their photospheric counterpart, due to the image drift caused by open-loop tracking system of KTT. Figure 3.17 shows scatter plot of chromospheric versus photospheric LoS magnetic field after roughly aligning the features, and it shows that they correlate well (correlation coefficient 0.87) with each other.

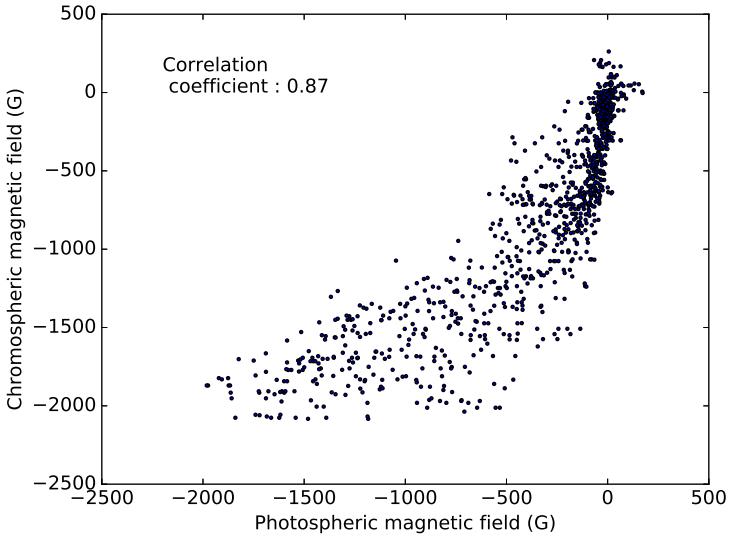

Figure 3.17: Line-of-sight magnetic field strength in chromosphere versus photosphere, for a few features in the observed region of interest shown in Figure 3.16.

Inversion of full Stokes profiles results in estimating more physical parameters such as LoS velocity and temperature. However, it is very much time and resource consuming to invert all the profiles. In the final chapter we describe the process and results of NLTE inversion of few of the observed Stokes profiles.

3.6 Summary & Conclusion

In this chapter, we presented processing and analysis of the spectropolarimetric data obtained from Solar Scanning Polarimeter. We have estimated various parameters that quantify SSP capabilities, such as polarimetric accuracy (better than 3%) and sensitivity (3×10^{-3} per 0.6 arcsec). We were also able to estimate instrumental effects to some extent. Signal-to-noise is improved to $\sim 10^{-3}$ by spatial and spectral binning considering the seeing limited spatial resolution and slit width limited spectral resolution. Looking at the amplitudes of characteristic Stokes Q and U profiles (Figure 3.13), we see that the polarimetric accuracy would be several folds better than that of our estimate of $\sim$ 3%. Scatter light measurements are limited by residual effects from flat fielding in Stokes I data. After data processing, we have constructed raster image and chromospheric line-of-sight magnetogram. We have compared them with continuum image and photospheric line-of-sight magnetogram obtained by HMI. Qualitatively they are in very good agreement. However, there are a couple of caveats:

1. Raster images are blurred owing to random image motion due to jitters and seeing, thusly limiting the spatial resolution.

2. Features (such as faculae/plages seen in magnetogram) are captured but their spatial correspondence is lost due to persisting image drift, limiting the scope of studying this data along with other data sets.

These problems are to be expected in a system where there is no closed-loop control over image motion. Hence, we have developed Image Stabilization System (ISS), a complementary system that can be integrated with SSP to arrest image motion that is mentioned in point (1) and provide stable image. It can also correct the image drift to certain extent. Its design, development and testing are presented in detail in Chapter 4. However, long term image drift described in point (2) has to be arrested by auto-guiding, which is not in the scope of this work.

Chapter 4

Image Stabilization System: Design, Development & Testing

4.1 Introduction

In ground-based as well as space-based telescopes, environmental effects cause image motion that severely limits the spatial resolution of observations. Table 4.1 lists out various factors that contribute to image motion and their effect, especially in the context of KTT.

Table 4.1: Description of various factors that cause image motion and extent of their effect.

Image motion	Contribution	Cause and Comments
Drift	few arcsec/minute, systematic and cumulative	Caused by misalignment in the Coelostat system, tracking speed errors. It is to be usually corrected by using auto-guiding.
Jitters	up to few arcsec RMS, random and slow (several tens of Hz)	Caused by moving mechanical components, wind loading and gusts. It is usually reduced by careful system design, and actively correcting the remainder.
First order aberrations	sub arcsec RMS, random and fast (several hundreds of Hz)	Caused by seeing that is, turbulence in the atmosphere. It is to be corrected dynamically (adaptive optics) or using specialized observational and processing techniques (speckle interferometry).

Stabilization is essential requirement for imaging applications such as raster scanning where, exposure times are longer than the timescales of disturbances causing the image motion and different spatial locations are imaged at different times. KTT has a Coelostat mounted in tower that tracks the Sun in open loop and provides the beam of sunlight for imaging. However, there is no closed loop control for this system and its consequences are evident. Figure 4.1 shows sample data obtained from image motion studies at KTT by imaging solar features with 10 ms exposure time and 10 frames per second. It shows image motion in x (green)- and y (blue)- directions, and corresponding power spectra. It is smoothed with a Gaussian window (σ = 2 seconds) to obtain image drift component (black). Barring drift, total RMS image motion is $\sim$0.5″. In x-direction, we see a large drift of 3″/minute. Primarily, KTT has been used for spectroscopic and spectropolarimetric observations. As we move to imaging be it raster scan or otherwise, stabilization is imperative to obtain good quality observational data.

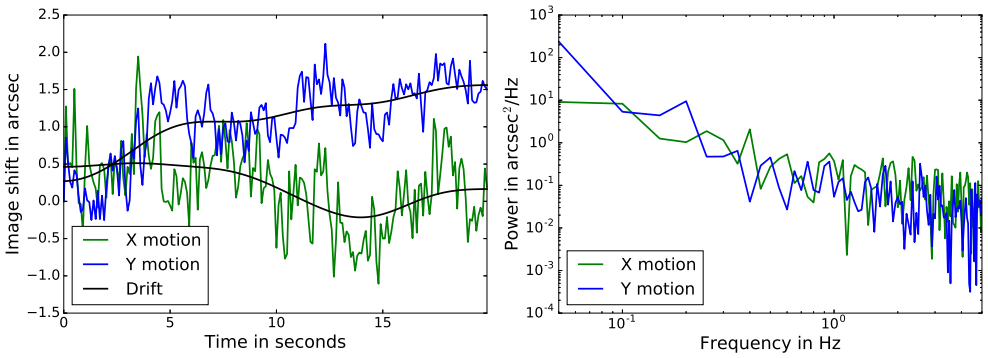

Figure 4.1: Sample data from image motion studies conducted at KTT (data courtesy: Dr. R. Sridharan). *Left*: image motion along x and y axes in arcsec vs. time, with drift indicated as black solid line (smoothed with Gaussian window of σ = 2 seconds). *Right*: power spectral density plot corresponding to image motion.

Image stabilization for SSP has two fold effect: 1) It improves spatial resolution of raster images, and 2) It reduces seeing induced polarimetric cross-talk (Judge et al., 2004) that is caused due to mixing of spatial elements of the image. Although the latter improvement is anticipated, it is not discussed here. We developed Image Stabilization System (ISS) as an upgrade to SSP to reduce the image motion thereby improving its quality.

A number of solar observatories are regularly employing image stabilization systems as part of telescope and adaptive optics system (e.g., Coulter et al., 2014; Fischer et al., 2016; Rao et al., 2016). Unlike night time astronomy where point sources are readily available and their motion is easily measured by using their centroid, solar imaging poses critical problem of image motion detection. The very successful and common technique that is currently used in both space-based (e.g., Shimizu et al., 2008) as well as ground-based (e.g., Von Der Lühe et al., 1989) telescopes is *correlation tracking*. In next sections, we describe the methodology of correlation tracking and instrument setup to implement it. We detail the tests performed with regard to main components, and image stabilization system calibration in the laboratory. Finally, we conclude with testing the system at KTT, and its capabilities and limitations.

4.2 Instrument

Image stabilization system is developed as complementary system to SSP's raster scanner. In its development, we have used methodology and inferences from previous developments at Udaipur Solar Observatory (Sridharan et al., 2007). Three principle actions are performed repetitively in ISS to achieve image stabilization: 1) Image acquisition, 2) Shift computation and 3) Applying correction. A mirror equipped with tip and tilt motion is setup in the path of beam that goes to the science instrument. Part of reflected beam from the mirror is diverted for high speed image acquisition, and rest is delivered to the science instrument. Images are acquired at very short exposure (typically 1 ms or less) with fast readout so as to capture frame in *frozen* environmental conditions. A reference image (I_{ref}) is acquired at first, and subsequent running images (I_{run}) are compared with it to compute the relative image shift (thus image motion). Once the shifts in both orthogonal directions are computed, tip and tilt corrections are applied to the mirror so as to mitigate the image motion. Reference image is updated periodically (several seconds, 3.5 seconds in present case) so as to capture any changes in the image.

Implementation of aforementioned actions, their performance and instrument details are discussed below.

4.2.1 Image acquisition

We have used Andor Neo 5.5 sCMOS detector with global shutter and high frame rate for image acquisition. Its full frame format is 2560×2160 pixels. However, we used 128×128 pixel region of interest to increase acquisition rate and subsequently the computing speed. We use global shutter (as opposed to high speed rolling shutter) option to ensure that all the pixels are exposed at the same time. *Andor SDK3* is used to develop custom subroutines in C++ programming language. Acquisition rate is tested to be ∼563 frames per second using these custom subroutines, which is close to manufacturer's specification. Once an image is acquired, 1.7 ms shall elapse till the next image becomes available. A fraction of this time is used for computing the image shift and applying tip-tilt corrections.

4.2.2 Shift computation algorithm

We have adopted Correlation technique using Fourier Transform (CFT) to estimate image shifts. The correlation algorithm is robust for computing image shifts for extended features, and implementing it using Fourier Transform (FT) is proven to be faster (Löfdahl, 2010). Implementation algorithm for CFT is shown in Figure 4.2. Details of programming options are listed in Table 4.3. Each of the functions is described below.

Pre-processing It consists of basic image corrections such as dark subtraction, flat fielding and image normalization. Thusly all the images are corrected for pixel-to-pixel sensitivity and overall image brightness variations.

Gradient correction It is done to remove slow intensity change across the image that is caused by the setup or present in the feature itself. As method of using Fourier transform to compute image shift is sensitive to such gradient it must be

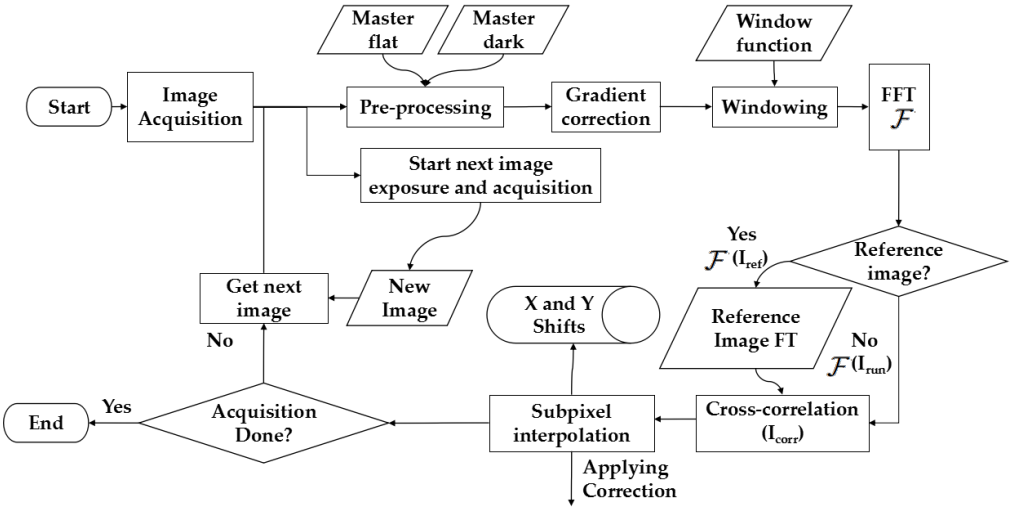

Figure 4.2: Flow diagram of shift computation algorithm that is implemented in C++

removed before transforming the image (von der Lühe, 1983). A surface given by $I = A + Bx + Cy + Dxy$ is fitted and subtracted from the image.

Windowing Solar features such as granule boundaries and sunspots are dark features with bright surroundings. Sharp contrast from bright edge of the image results in residual spectral features after Fourier transform is applied. Although its effect is prominent when the feature has very low contrast, we have incorporated windowing to reduce spectral side lobes. Instead of bright image edge, intensity is slowly reduced to zero in the edges by multiplying with custom window function.

Fast Fourier Transform It is an efficient and fast implementation of Fourier transform. We have used third party "C" programming library FFTW3 (Frigo and Johnson, 2005) to perform forward and inverse Fourier transform operations. This library has optimizations for array with 2^n size, Fourier transform from real to complex arrays and Fourier transform from complex to real arrays, all of which are relevant for the images acquired with ISS. It is applied on reference image (I_{ref}) and the result ($\mathcal{F}(I_{ref})$ where "$\mathcal{F}$" denotes Fourier transform operation) is stored. Subsequent running images (I_{run}) are transformed ($\mathcal{F}(I_{ref})$) and used with $\mathcal{F}(I_{ref})$ to compute correlation.

Correlation Correlation between two images using Fourier transform is computed as given in Eq. (4.1) (von der Lühe, 1983) where "$*$" denotes complex conjugate. Fourier transforms of reference and running images are used to compute correlation. Position of maximum correlation value with respect to the image center gives relative shift between two images. Precision of shift calculated is one pixel.

$$I_{corr} = \mathcal{F}^{-1}(\mathcal{F}(I_{ref}).\mathcal{F}(I_{run})^*) \tag{4.1}$$

Interpolation Considering image shift in the order of tens of pixels and applicable corrections, pixel level image shift computation might suffice for most applications. However, for the cases of good seeing conditions and higher resolution, computing shift value to sub-pixel level yields even better corrections. Two dimensional quadratic interpolation (von der Lühe, 1983) of 3×3 pixels is used for computing sub-pixel level shift.

We have developed subroutines for aforementioned processes in C++ and tested them for their speed and accuracy. Image motion data acquired from KTT is used for the testing.

Speed Test For testing speed, a single reference frame and a single running frame are loaded. Relative shift between them is computed repeatedly for 10,000 times. This program is executed 100 times and results are plotted as shown in Figure 4.3. The same test is applied for individual processes and their speed is computed. Results are summarized in Table 4.2 along with acquisition time, for the sake of comparison. As it can be seen, it takes 0.9 ms to compute shift for a 128×128 image using all the essential and optional processes. Compared to acquisition time of 1.77 ms, shift computation time is very less and hence we can say that ISS speed would be limited by rate of acquisition.

Accuracy Test For testing accuracy, one of the images is selected from KTT image motion study. One thousand frames (sub-images) with 128×128 format are selected from the this image. First frame of the 1000 is selected to be the reference frame.

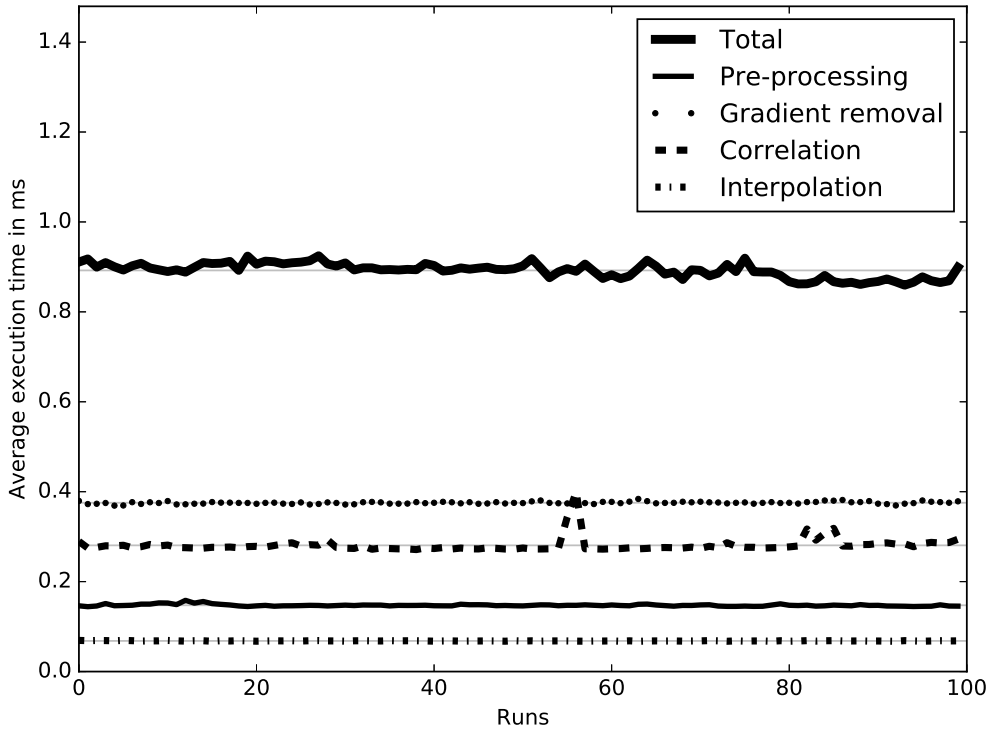

Figure 4.3: Plots of speed test results for shift computation subroutines. Each point corresponds to average time estimated from 10,000 shift computations. Gray solid line for each plot indicates average of 100 values in that plot. Occasional spikes are most likely caused by the increase in load on the processor due to background processes.

Table 4.2: Time required for executing various processes of image shift computation, and their comparison with acquisition process.

Task	Execution time in ms
Pre-processing	0.15
Gradient correction	0.38
Correlation	0.29
Sub-pixel interpolation	0.07
Total execution	0.90
Total essential execution	0.52
Image exposure	1
Image read-out	0.77
Total image acquisition	1.77

Rest of the frames are selected in such a way that their relative shifts with respect to the reference frame are random and within ± 4 pixels (comparable to typical

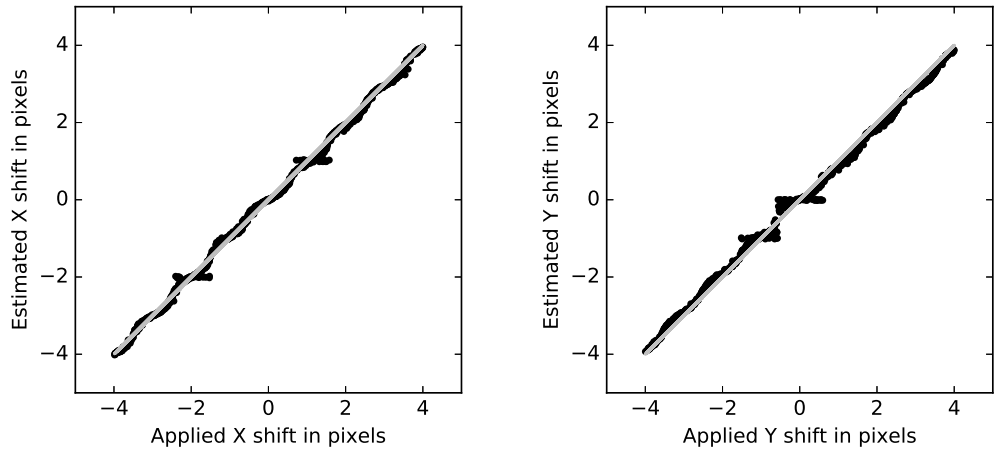

Figure 4.4: Accuracy test results for shift computation subroutines. Estimated shifts for x and y axes are plotted against applied shift. Gray colour line represents $x = y$. Deviation from applied values are at sub-pixel level.

shifts that we expect). We have used C++ subroutines to load them and compute the image shifts. Results are plotted in Figure 4.4 and we conclude image shift computations are accurate to the level of one-fifth of a pixel.

4.2.3 Applying corrections

After computing shift in pixels, corresponding corrections must be applied by tipping and tilting the mirror that is present in light path so as to mitigate the image motion. In order to achieve this, mirror is mounted on two-axis *piezo-actuator*. It tips and tilts the mirror with a response time of the order of hundred μs when voltages are applied to corresponding axes. Suppose $\mathbf{P}$ and $\mathbf{V}$ represent pixel shifts and voltages required to be applied to cause such shift, we write their relation as

$$\mathbf{V} = \mathbf{a}.\mathbf{P} \tag{4.2a}$$

or

$$\begin{bmatrix} V_x \\ V_y \end{bmatrix} = \begin{bmatrix} a_{00} & a_{01} \\ a_{10} & a_{11} \end{bmatrix} \begin{bmatrix} P_x \\ P_y \end{bmatrix} \tag{4.2b}$$

where **a** is control matrix. Using aforementioned equation, incremental shifts given in pixels are converted into incremental voltages. Procedure to calculate control matrix is described in Section 4.3.2. Once the voltages are computed, a correction signal is generated and applied by method of Proportional-Integral-Derivative (PID) control. For actuator's x axis n^{th} correction $e_x[n]$ is given by Eq. (4.3), and a similar relation follows for y axis too.

$$e_x[n] = K_p.V_x[n] + K_d.\frac{\Delta V_x[n]}{\Delta n} + K_i.\frac{\sum_{n-N}^{n} V_x[n]}{N} \tag{4.3}$$

K_p, K_d and K_i are called proportional, derivative and integral gain constants respectively. They are tuned iteratively by trial and error till we obtain desired residuals, and the process is described in Section 4.3.3.

Piezo-actuator controller and amplifier provide provision to apply actuator voltages by means of sending a serial command to controller or directly applying analog voltage of range 0–10 V to amplifier. For high speed operation of actuator, we have chosen to apply analog voltage using data acquisition (DAQ) card that is controlled using associated C/C++ library.

4.2.4 Design

Figure 4.5 shows the layout of ISS and its integration into telescope system. Mode switching mirror is replaced by Tip-Tilt Mirror (TTM) that is, a plane mirror mounted on the actuator. Imaging channel is occupied by sCMOS detector (ID) to acquire short exposure images at high frame rate. Actual system installed at the KTT is shown in Figure 4.10. As the pixel size is too small for KTT's plate scale, re-imaging optics is used to de-magnify the image. A broadband filter of 100 Å is used with the detector to enhance image contrast compared to white light. A set of two polarizers, one stationary and other rotating, is used for light level control. This is to ensure that ISS operates at highest possible speed with wide range of light levels.

However, there is one severe limitation with this design. As ISS is operated in the converging beam at KTT (f#96) and spectrograph is the back-end instrument,

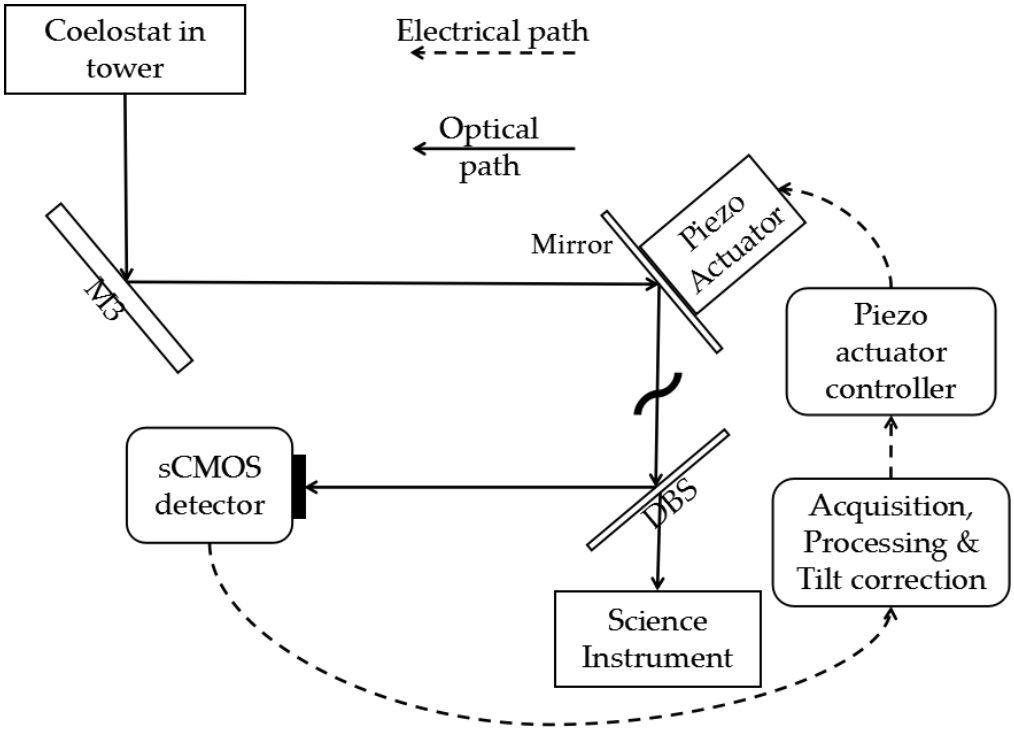

Figure 4.5: Layout of image stabilization at the back-end of KTT. Vertical beam from the Coelostat is folded by 90° and directed into the horizontal tunnel by M3. High speed acquisition detector is placed in the imaging channel created by Dichroic Beam Splitter (DBS) of the solar scanning polarimeter.

illumination on the grating changes as the image is moved by means of tipping and tilting the converging beam. From geometry, shift in beam that falls on the grating is estimated to be 30 times the image shift on the focal plane that is, if one arsec image motion is corrected by TTM, beam on the grating moves by 5.5 mm. Considering the illuminating beam size of ∼200 mm this effect may become significant only at large shifts. Previous image motion studies show that barring image drift, RMS image motion is less than 0.5″ in 20 second duration. Hence, we conclude that this limitation affects observations depending on seeing conditions, and it needs further evaluation using actual observations.

4.2.5 Summary of components

Important specifications of the components and tools used in developing image stabilization system are listed in Table 4.3.

Table 4.3: Summary of important specifications of image stabilization system components.

Specification	Value
Detector	
Make and model	Andor Neo 5.5
Type	sCMOS
Region of Interest (pixels)	128×128
Minimum exposure time	0.7 ms
Frame rate (1 ms exposure with global shutter)	563
Workstation processor	
Make and model	Intel Core i5 3470
Clock speed	3.2 GHz
Number of cores and threads	4, 16
Programming	
Programming language	C++ (11)
Compiler	GNU C++ compiler
Optimizations	Default
Operating system	Windows 7, 64-bit
Piezo-actuator	
Make and model	Piezosystemjena PSH 10/2
Tilt range	± 4 mrad
Mounting mirror size	25 mm (50 mm max.)
Resonance frequency	3.5 KHz
Piezo-amplifier	
Make and model	Piezosystemjena, EVD series
Amplifier input range	0 to 10 V
Amplification, Bias	15, –20 V
Typical slew rate	5 V/ms

Data acquisition card	
Make and model	National Instruments DAQ X-series
Number of analog outputs	2
Analog output range	$\pm$ 10 V

4.3 Laboratory Testing

We have conducted several tests in the laboratory to characterize the image stabilization system. Figure 4.6 shows layout of laboratory setup used to conduct tests. Resolution target plate that is back-illuminated with white light is used as extended source. Motion-Mirror (MM) is another mirror mounted on piezo-actuator. It is used to induce known image shifts. Tip-Tilt Mirror (TTM) and Imaging Detector (ID) are part of ISS. Beam f-ratio, and distance between the actuator and detector is maintained to be comparable to that of the system present at KTT. In that sense, laboratory setup emulates on-site setup.

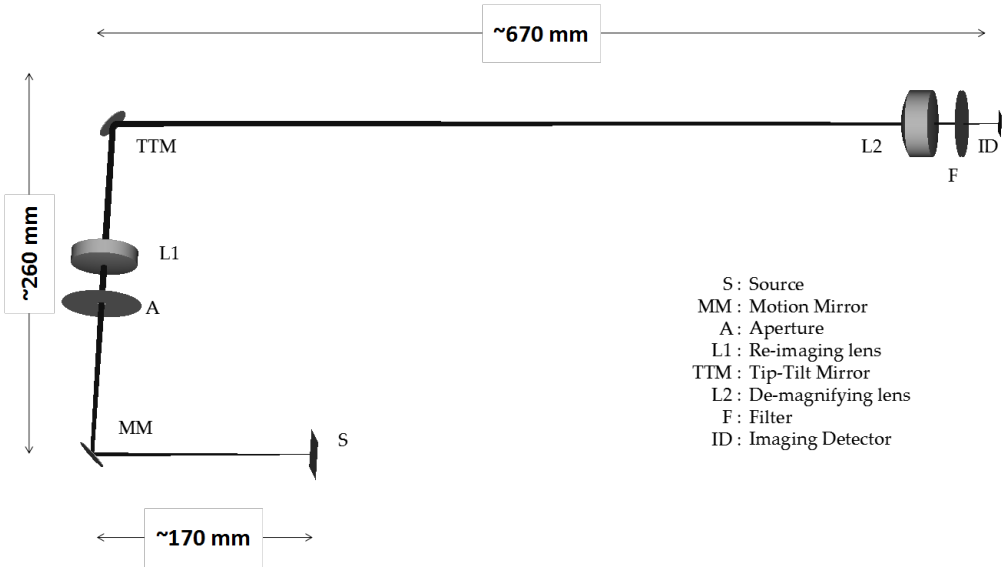

Figure 4.6: Layout of the laboratory setup used for testing image stabilization system.

4.3.1 Operating voltage range

We have tested actuator response in various voltage ranges to estimate whether it would be optimum to operate in a particular voltage range. Piezo-actuator operates between –20 to 130 V range. Here we have considered ± 10 V range centered at 0 V, 30 V, 60 V for both x and y axes. Reference image is taken at center voltage. First, voltage is slowly reduced by 10 V. Then it is slowly increased by 20 V and subsequently decreased to reference voltage. Figure 4.7 shows the plots of results obtained.

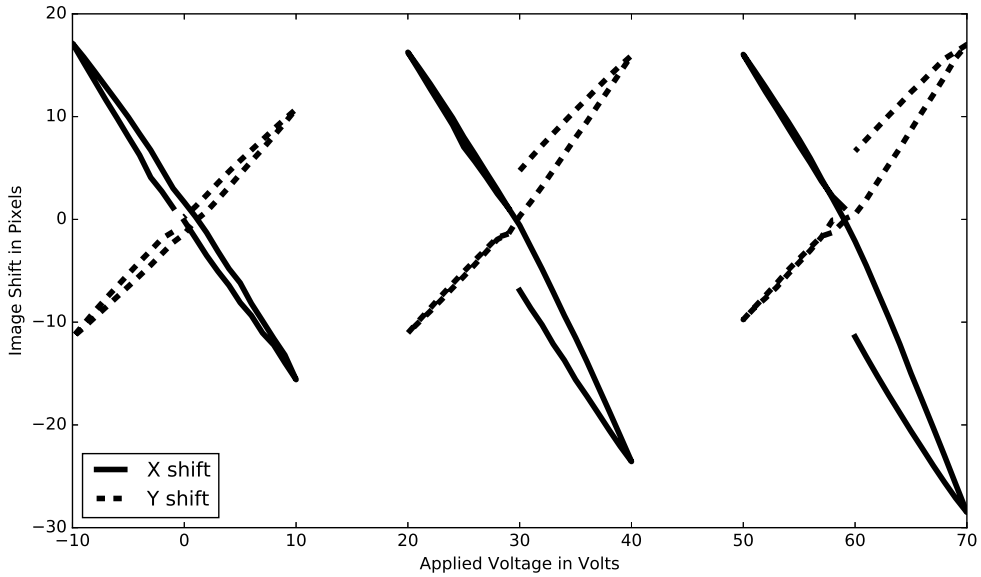

Figure 4.7: Actuator response at different operating voltages centered at 0 V, 30 V and 60 V.

From this test (Figure 4.7), we see that actuator's response is not the same at higher voltages as it is at lower voltages. It appears to have different response to increasing and decreasing voltage, resulting in higher hysteresis at higher voltages. Hence, we have selected operating voltage to be centered at 0 V. Considering 1.5 to 2 pixel shift per volt being typical conversion factor as gathered from emulating system, –20 to 20 V operating voltage should be sufficient to respond to image shifts that are expected to be occurring.

4.3.2 Calibration matrix

Consider the image shift to actuator voltage relation. For a linear system it is given by Eq. (4.4) where **s** indicates calibration matrix, that is nothing but inverse of control matrix **a** (Eq. (4.2)).

$$\mathbf{P} = \mathbf{s}.\mathbf{V} \tag{4.4a}$$

or

$$\begin{bmatrix} P_x \\ P_y \end{bmatrix} = \begin{bmatrix} s_{00} & s_{01} \\ s_{10} & s_{11} \end{bmatrix} \begin{bmatrix} V_x \\ V_y \end{bmatrix} \tag{4.4b}$$

In the case of actuator reference axes being aligned with detector reference axes, **s** becomes a diagonal matrix. However, it is not the case in practice. Hence **s** must be computed by applying known voltages and measuring resulting shifts. This procedure is calibration and it is executed in following steps.

1. Center voltages of operating voltage ranges are applied to both the axes.
2. Only V_x is varied and x and y pixel shifts are measured.
3. Only V_y is varied and x and y pixel shifts are measured.
4. Four plots (P_x vs V_x, P_y vs V_x, P_x vs V_y and P_y vs V_y) are obtained, and four lines are fitted to them. Slopes of these lines are the elements of **s**.

Further, this matrix is inverted to get control matrix that can be used to convert pixel shifts to respective voltages.

$$\mathbf{a} = \mathbf{s}^{-1} \tag{4.5a}$$

or

$$\begin{bmatrix} a_{00} & a_{01} \\ a_{10} & a_{11} \end{bmatrix} = \frac{1}{s_{00}s_{11} - s_{10}s_{01}} \begin{bmatrix} s_{11} & -s_{01} \\ -s_{10} & s_{00} \end{bmatrix} \tag{4.5b}$$

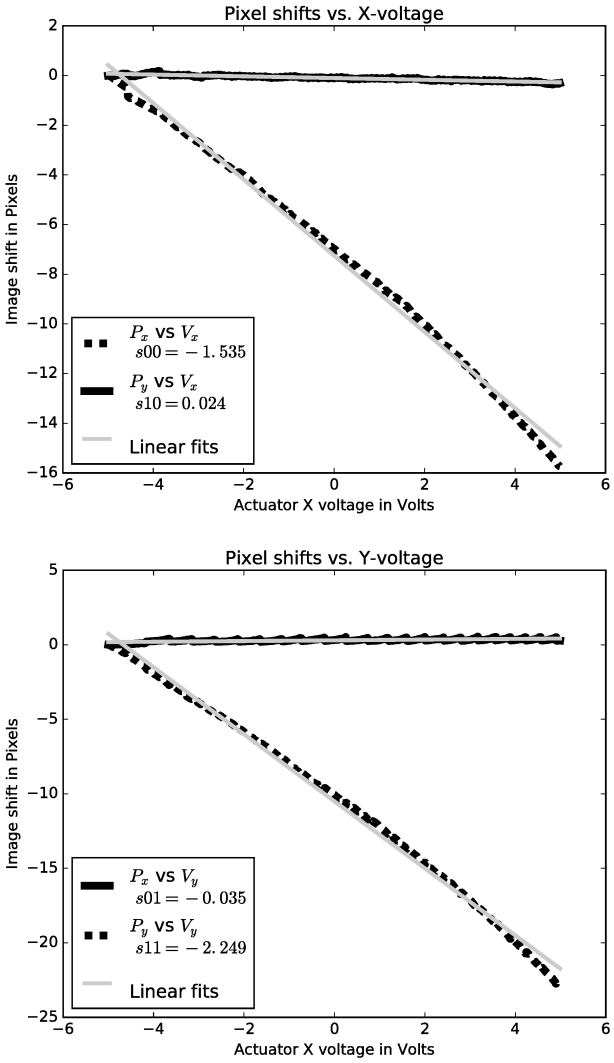

Figure 4.8: Calibration plots for estimating pixel to voltage conversion. *Top*: x and y shifts when only V_x is varied, and *bottom*: x and y shifts when only V_y is varied. Slope of each fitted lines gives an element of the calibration matrix.

Figure 4.8 shows plots of four lines that correspond to applied voltage versus measured shifts. From these plots we compute

$$\mathbf{s} = \begin{bmatrix} -1.535 & 0.024 \\ -0.035 & -2.249 \end{bmatrix} \tag{4.6a}$$

$$\mathbf{a} = \begin{bmatrix} -0.651 & -0.007 \\ 0.010 & -0.444 \end{bmatrix} \tag{4.6b}$$

We observe that the actuator has different responses for x and y axes. As the beam is folded horizontally by 90° and mirror normal makes 45° with detector normal, different axes have different response.

4.3.3 Estimating control parameters

Control parameters K_p and K_d are estimated by method of trial and error that is, we change K_p and K_d in steps until acceptable corrections are achieved. Although controls are developed to implement integral error correction, K_i is not used in the tests as we observe that accumulated error is not significant. Our later observations on telescope also support this. We arrived at a crude estimate for K_p and K_d in the laboratory and used them as starting points when testing at the site. By nature, K_p corrects for present error estimation and K_d corrects for error predicted for the next sample.

We have introduced known image motion using motion-mirror and corrected it with tip-tilt mirror of image stabilization system. By changing control parameters and monitoring corresponding residuals, we arrived at optimum control parameters. We have applied sinusoidal voltage with fixed amplitude and various frequencies to motion-mirror to induce image motion. Figure 4.9 shows image motion introduced and corrected for two frequencies.

When the frequency of image motion is low (10 Hz), setting K_p alone is sufficient and delivered more than 80% reduction in image motion. At higher frequency (50 Hz), using K_p alone resulted in amplified image motion but setting K_d = 0.5 yielded 10% reduction. Hence, we have decided to use $K_p < 0.7$ and $K_d \sim 0.5$ for further on-telescope testing of ISS.

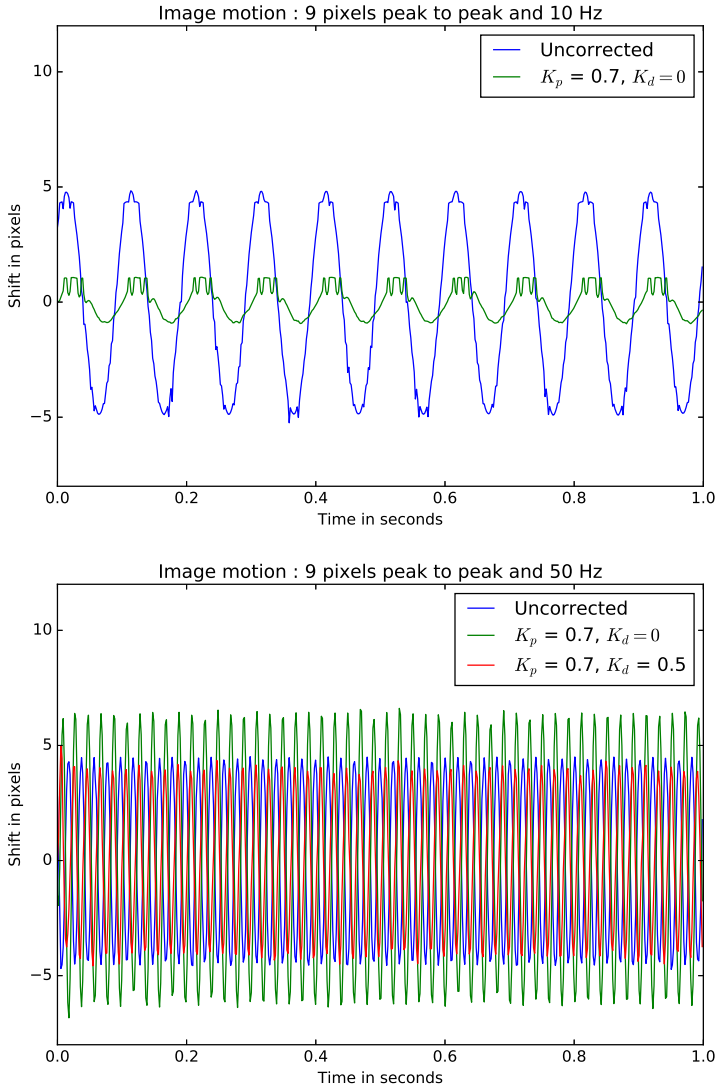

Figure 4.9: Image shift correction for low and high frequency disturbances. *Top*: 10 Hz disturbance (blue) corrected with $K_p = 0.7$ alone (green). *Bottom*: 50 Hz disturbance (blue) corrected keeping $K_p = 0.7$, and with $K_d = 0.0$ (green) and $K_d = 0.5$ (red).

4.4 On-telescope Testing

Main objective of ISS is to achieve image stabilization at KTT for solar imaging related observations. Here, we describe installation of image stabilization system at KTT and its integration into solar scanning polarimeter setup. Image stabilization using sunspot region is used for validation and results are discussed.

4.4.1 Installation

Image stabilization system is installed at KTT and integrated into solar scanning polarimeter, by replacing mode switching mirror (first optical element of SSP in the beam path) with tip-tilt mirror. Figure 4.10 shows ISS integrated into SSP. Imaging channel provided by dichroic beam-splitter reflection is used for acquiring images. A region of interest of $19'' \times 19''$ is covered by 128×128 pixels on the detector. Green filter with λ ($\Delta\lambda$) = 5500 Å (100 Å) is used for imaging. Installed setup follows the design as described in Section 4.2.4. We have computed the calibration and control matrices for the system and stored as configuration file. Since there is only one focal plane available that is, on the detector, it is not possible to calibrate the system as described earlier. Instead, a shadow is cast on the detector by placing an obstruction before the tip-tilt mirror, and that is used as a feature. Subsequently, we have acquired the flats by randomly moving the solar image on the detector and calculating average of the acquired frames.

4.4.2 Image stabilization using Sunspot

We have tested image stabilization system using a sunspot in the active region NOAA 12734 for imaging, on March 9, 2019. Control parameters are tuned and found to be $K_p = K_d = 0.6$. All the computed image shifts, applied corrections and reference images are saved to the disk. This data are used to compute the image motion that would have been induced at the time of ISS operation. Figure 4.11 shows image shifts and corresponding power spectra for x and y directions, and overall, observed at 08:32 UT. Residual image shifts are compared with uncorrected image shifts.

From plots shown in Figure 4.11, we see that there is a significant drift along the x axis. This is consistent with previous image motion studies (Figure 4.1) which also found persistent drift in that direction. We removed the drift component and computed RMS image motion before and after corrections. They are tabulated in Table 4.4.

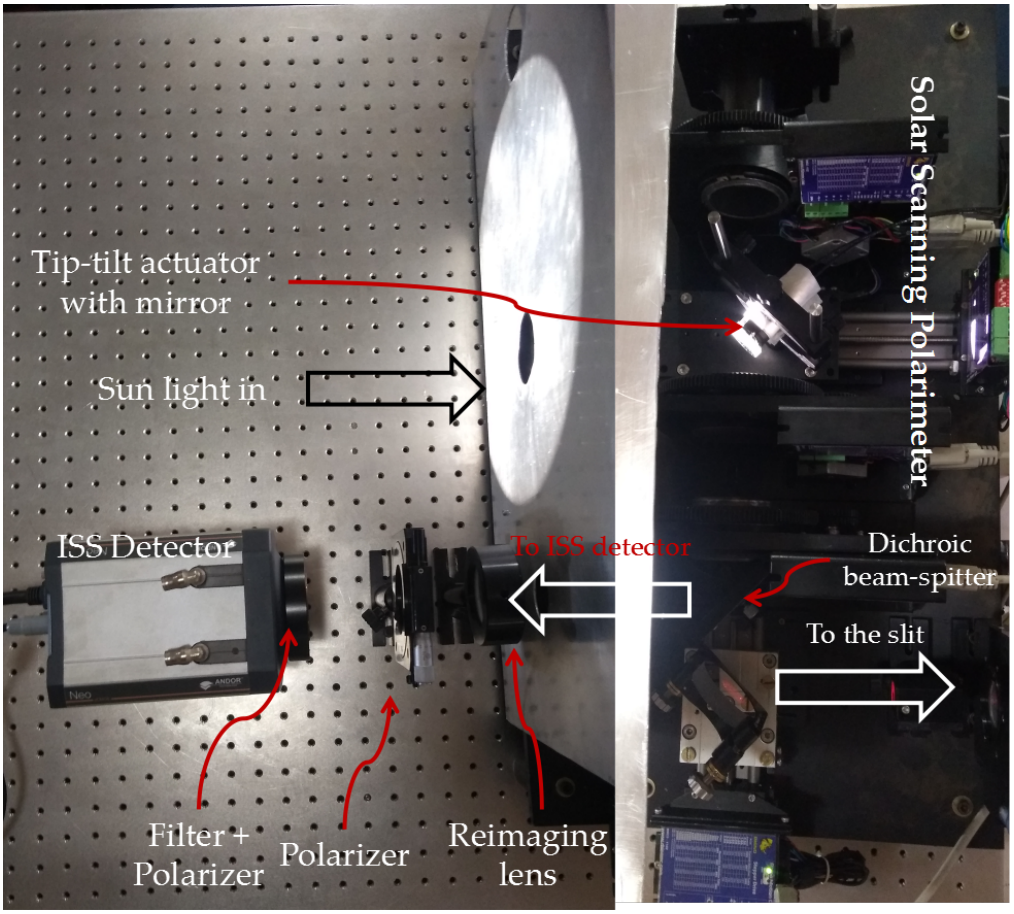

Figure 4.10: Image stabilization system integrated with solar scanning polarimeter at KTT.

Table 4.4: RMS image motion before and after applying corrections (rounded off to second decimal place).

Parameter	x	y	Total
Uncorrected RMS image motion (arcsec)	1.27	0.99	1.60
Drift subtracted uncorrected RMS image motion (arcsec)	0.56	0.73	0.92
Corrected RMS image motion (arcsec)	0.02	0.03	0.04
No. of folds improvement without considering drift	29	24	26
No. of folds improvement including drift	64	33	45

Ratio of power spectra corresponding to corrected and uncorrected shifts is shown in Figure 4.12. For this system, 0 dB closed loop bandwidth that is, highest frequency till which corrections are achievable, is found to be f_{BW} = 110 Hz. It is marked by a circle where power spectral ratio is 1, and corresponding frequency is marked with vertical line.

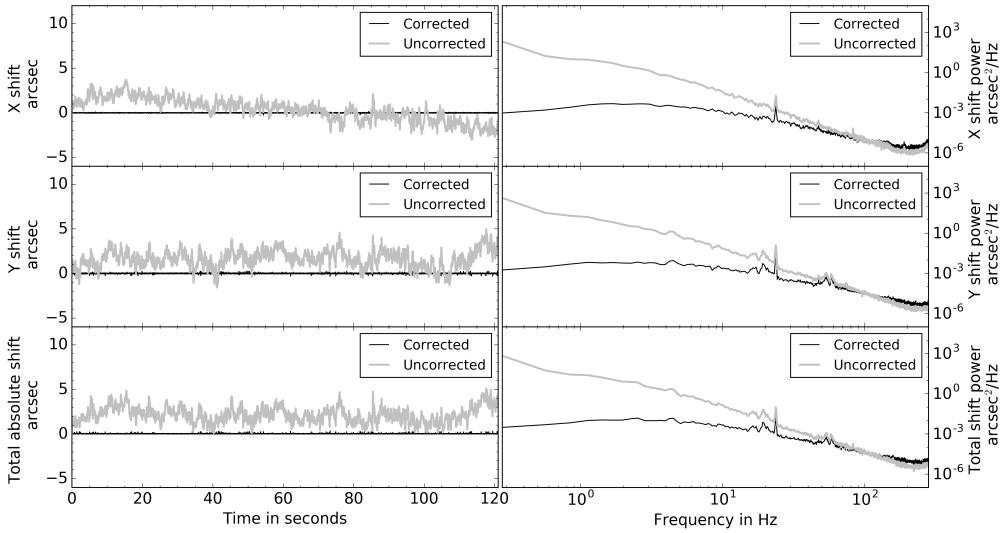

Figure 4.11: *Left*: image shift in arcsec plotted against time and *right*: power spectral density plots for corresponding image motion.

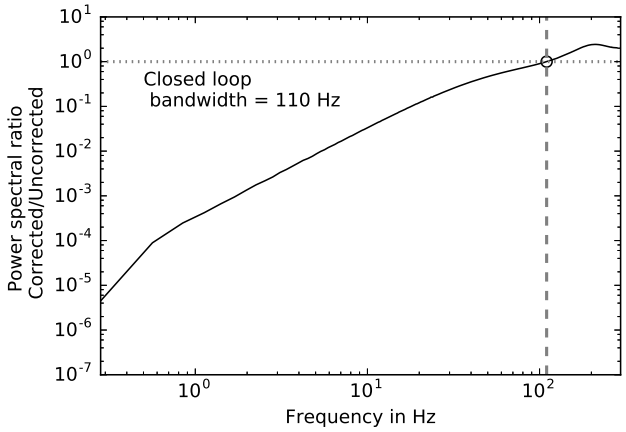

Figure 4.12: Corrected to uncorrected power spectral ratio. Horizontal line is ratio = 1, and vertical line is frequency for which power spectral ratio is 1.

For recording uncorrected images, we have performed high speed acquisition alone without operating ISS and saved all the images to the disk. Figure 4.13 shows average of reference images in correction loop (middle) and average image without applying corrections (left). HMI/SDO image of the same spot is shown for reference (right).

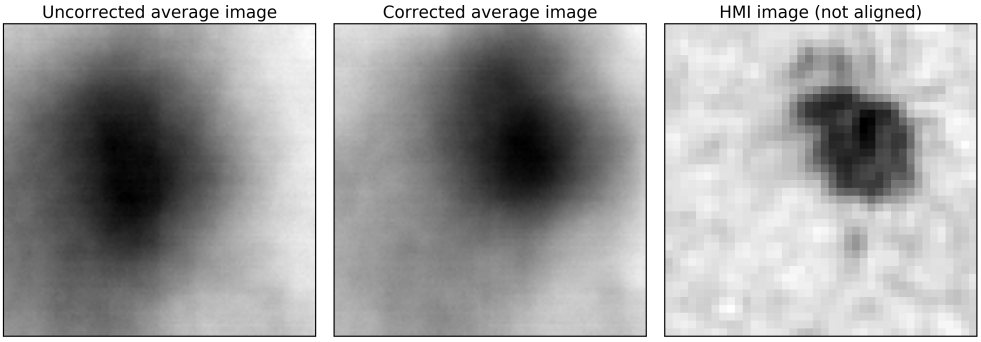

Figure 4.13: Mean uncorrected image (*left*), mean corrected image (*middle*), and HMI/SDO image (*right*) taken at the same time.

4.4.3 Discussion

Image stabilization system has been successfully demonstrated for KTT with laboratory as well as on-telescope testing. Image motion is reduced by 26 times (not considering the telescope drift) which corresponds to stabilization to a level of 1/10 times diffraction limited resolution of the telescope. We have quantified the image quality by using image gradient, with the expression given in Eq. (4.7) as $I.Q.M.$. Note that the image is normalized to the mean.

$$I.Q.M. = \Sigma(\nabla_x I)^2 + \Sigma(\nabla_y I)^2 \tag{4.7}$$

where, ∇_x and ∇_y correspond to image gradients in x and y directions and $I.Q.M.$ is image quality measure.

The idea is that if image has no features then variations in the intensity that is, its gradient would be zero. However, if image has become sharper then image gradient should have values away from zero, increasing its variance (Helmli and Scherer, 2002). The same is visualized in Figure 4.14 where the histograms of absolute values of gradients of images are shown. Histogram corresponding to corrected image has stronger tail than the one corresponding to uncorrected image. It implies that the image has become sharper after applying corrections. $I.Q.M$ for corrected and uncorrected images is calculated to be 0.291 and 0.267 respectively.

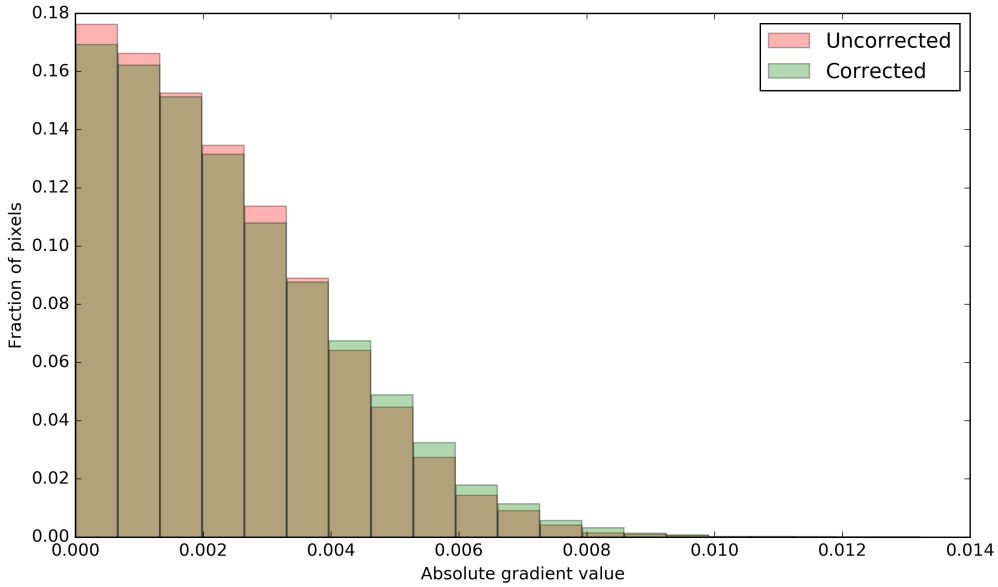

Figure 4.14: Histograms of absolute image gradient for uncorrected and corrected images. Corrected image gradient has more values away from zero as seen in green colour. Overlap of both histograms is shown in yellow colour.

From earlier studies as well as current observations, we gather that there is a significant image drift which is main limitation for sustained image stabilization. It can be clearly seen in x motion plot of Figure 4.11. Image is drifted by 2″ in one minute where as rest of the image motion is less than 0.5″. At present, we could stabilize the image for three minutes in the morning ($\sim$ 07:00–09:00 LT) where aforementioned image motion is observed.

4.5 Summary & Conclusion

In present chapter, we have described a sub-system namely Image Stabilization System (ISS) that can arrest the image motion induced in the focal plane of KTT. We have selected appropriate components and algorithm, developed suitable subroutines, and tested them in the laboratory. Subsequently, we have integrated ISS with emulation of KTT setup in order to test the total system performance. After successful testing in the laboratory, we have moved the system onto the telescope and integrated it with Solar Scanning Polarimeter (SSP). We did on-telescope testing to

evaluate its capability to stabilize the image and reported the results. Closed loop bandwidth of the system is estimated to be 110 Hz, which should be very effective in reducing even seeing induced image motion.

A number of limitations also must be evaluated before integrating ISS with SSP for good. A typical spectropolarimetric observing run with 60 scan steps takes about 14 minutes. In order for ISS to be operating for such duration, image drift must be arrested with an auto-guider. Once the auto-guider is working, ISS performance should be lasting for significantly higher duration. However, as discussed in Section 4.2.4, effects of dynamic tip-tilt mirror on the spectrograph based back-end setup also needs to be evaluated before the integration.

So far, we have described our instrumentation efforts towards producing chromospheric magnetograms. In the context of the thesis, we conclude the instrument development at this juncture however, with a wide scope for the future. A number of improvements for the current system, and requirements for its successors are discussed in Chapter 6. Further, otherwise applications of ISS are also discussed.

Chapter 5

Correlation between the Chromospheric and Potential Extrapolated Magnetic Fields in Active Regions

5.1 Introduction

Active region magnetic fields play integral role in solar dynamics. Interplay between the magnetic and gas pressures shapes the structures of active region magnetic fields. In deeper photosphere, magnetic field is confined as the gas pressure is dominant. As we go outwards in the solar atmosphere gas pressure decreases, magnetic field is less confined and magnetic field lines start to spread out. This effect continues until field from one magnetic element interacts with fields from other magnetic elements. Consequently, at some point they lead to formation of a *magnetic canopy*, around heights corresponding to lower chromosphere (Giovanelli and Jones, 1982). Observationally, magnetograms corresponding to lower photosphere show confined patches with sharp boundaries where as magnetograms taken in subsequent heights corresponding to upper photosphere, lower and middle chromosphere show more and more diffused features (Giovanelli and Jones, 1982). At the center of sunspots, magnetic field strength was observed to be decreasing with

height. However, nearby locations that show next to no field strength in photospheric magnetograms were recorded to be showing considerable field strength at chromospheric level, owing to aforementioned phenomenon (Solanki et al., 2006, Section 6 and references therein).

Considering such conditions of solar atmosphere, magnetic field configuration can be modeled provided necessary information (that depends on the model) about the magnetic field at the boundary is available. Generally, only photospheric magnetograms are obtained with high reliability and regularity (Keller et al., 2003; Schou et al., 2012) as (1) a number of well modeled spectral lines with high sensitivity to magnetic field (high Landé g-factor) are available, and (2) magnetic field strength at the photospheric level is relatively high resulting in strong polarization signal.

On the other hand, imaging observations are made in multiple broad and narrow spectral bands to image the Sun at various heights or temperatures (Lemen et al., 2012; Ravindra et al., 2018). By means of modeling the magnetic field using available magnetograms, it can be extrapolated to various heights (Sakurai, 1989; Gary, 1989; Gary, 1996). Results of such modeling are widely used for the comparative studies of magnetic fields with other imaging and magnetic field observations (Teuber et al., 1977; Choudhary et al., 2001; Ravindra and Venkatakrishnan, 2003; Tu et al., 2005; McCauley et al., 2015).

As discussed in Section 1.2.3, simple assumption to model magnetic field can be to think of it to be current-free and extrapolate it using photospheric magnetogram as lower boundary condition. This has worked reasonably well in the past for various kinds of studies. For smaller regions of interest, potential magnetic field extrapolation can be made assuming plane parallel geometry. Choudhary et al. (2001) have used observed chromospheric magnetograms (obtained from spectropolarimetric observations of Ca II 8542 Å line), and computed chromospheric magnetograms (obtained from potential magnetic field extrapolations) for a statistical

study of three dimensional structure of the active regions. For the magnetic field extrapolations, photospheric magnetograms (obtained from spectropolarimetric observations of Fe I 8688 Å line) were used as lower boundary. They found that the computed and observed chromospheric magnetograms have best correlation at a height of 800 km, and in the weak field range (few hundreds of Gauss) observed magnetic field is close to potential in nature.

Such extrapolations were also used to understand relation between photospheric magnetic fields and structures observed in upper layers (Ravindra and Venkatakrishnan, 2003; Tu et al., 2005). For full disk magnetograms, magnetic field is extrapolated assuming a potential field with source surface (PFSS) in spherical geometry (Schatten et al., 1969; Schrijver and Derosa, 2003). This was used to model the magnetic field at coronal heights. Results from such modeling were used for comparative study with EUV coronal images (e.g., McCauley et al., 2015; James et al., 2017) and radio observations (e.g., James et al., 2017).

In the present study, we apply Potential Magnetic Field Extrapolation (henceforth referred as PMFE) to active region magnetic fields, in the context of finding the probable height of chromospheric spectral line formation in active regions. We assume plane parallel geometry and use photospheric magnetograms of selected active regions as lower boundary to model the magnetic field at various heights above the photosphere. Such *extrapolated magnetograms* are then compared with observed chromospheric magnetograms obtained from spectropolarimetric observations of Ca II 8542 Å spectral line. Extrapolated magnetogram that yields highest correlation with observed chromospheric magnetogram corresponds to the height of line formation for that particular active region. We apply this to a number of active regions to find probable height of line formation in the active regions. Photospheric as well as chromospheric magnetograms used for this study are obtained by Synoptic Optical Long-term Investigations of the Sun (SOLIS; Keller et al., 2003) of National Solar Observatory (NSO). This could have also been done with the data obtained from SSP. However, during our observation period number of active regions was very low, and also the field of view of our instrument is small. Hence,

we used the data taken from other observing facility.

5.2 Instrument & Data

For the present study of comparing the chromospheric active region magnetic fields with the extrapolated photospheric magnetic fields, it is good to use the data obtained from the same instrument and if possible at the same time. It is also good if the active region is located close to the disk center to avoid any possible effects of projection. Below, we describe the observing instrument, and data obtained from it and its analysis.

5.2.1 Observing instrument

The data used for present study are acquired by Vector SpectroMagnetograph (VSM) of SOLIS, a synoptic solar observing facility operated by National Solar Observatory (NSO). VSM is a back-end instrument for 50 cm telescope of SOLIS. It has a combination of polarimeter unit and slit based Littrow spectrograph. It records the spectrum of three spectral ranges corresponding to following lines: Fe I 6301.5 Å - 6302.5 Å, Ca II 8542 Å and He I 10830 Å. As for the polarimeter, two sets of calibration modules (one for Fe I and another for Ca II) are placed in front of the slit. Three sets of liquid crystal retarder based modulators (one for circular polarimetry of Fe I lines, another for vector polarimetry of Fe I lines and the last one for circular polarimetry of Ca II) are mounted on a sliding mechanism placed behind the slit. The slit has 2048 arcsec spatial coverage along its length.

Spectra corresponding to aforementioned lines are formed near the slit, and a focal plane beam splitter splits it into two 1024 arcsec long spectra. They are re-imaged onto two detectors with polarizing beam splitters placed just before each detector. Thusly, each detector records two orthogonal states of polarization data corresponding to each hemisphere of the solar disk. For each slit position on the solar disk, polarimetry is performed. Spatial scanning is achieved by moving the telescope in declination direction while tracking the Sun. For each slit position, modulated intensities are recorded for computing the Stokes profiles. This data is

processed to produce photospheric vector magnetograms and chromospheric Line-of-Sight (LoS) magnetograms (B_{LoS}). Scanning the full disk with spectropolarimetric observations of Fe I and Ca II takes approximately 20 minutes and 40 minutes respectively.

5.2.2 Data description

Vector spectromagnetograph produces full disk LoS or vector magnetic field maps of the Sun at photospheric (vector) and chromospheric (LoS) heights by means of spectropolarimetric observations of Fe I and Ca II lines. Data from the two detectors that observe each of the solar hemispheres are stitched together and following important processes are applied to produce Stokes profiles corresponding to full disk :

- Gaps in the raster image due to splitting the beam are corrected.
- Intensity is normalized so that data from both the detectors is consistent.
- Image distortion and curvature in the spectra are corrected.
- Wavelength is approximately calibrated.

Once corrected data are obtained, Stokes profiles are inverted to produce the magnetic field map. Milne-Eddington (Skumanich and Lites, 1987) inversion is applied to Fe I Stokes profiles to produce photospheric magnetogram. For chromospheric magnetogram, Weak Field Approximation (WFA; Jefferies et al., 1989) is applied to Ca II Stokes profiles. Solar disk is centered with respect to the frame and rotated so as to match the image axes to reference axes of heliographic coordinate system. We have used level-2 data for our analysis which consists of 2048×2048 pixel full disk LoS magnetograms with spatial plate-scale of 1 arcsec/pixel. Relevant information is stored in the header.

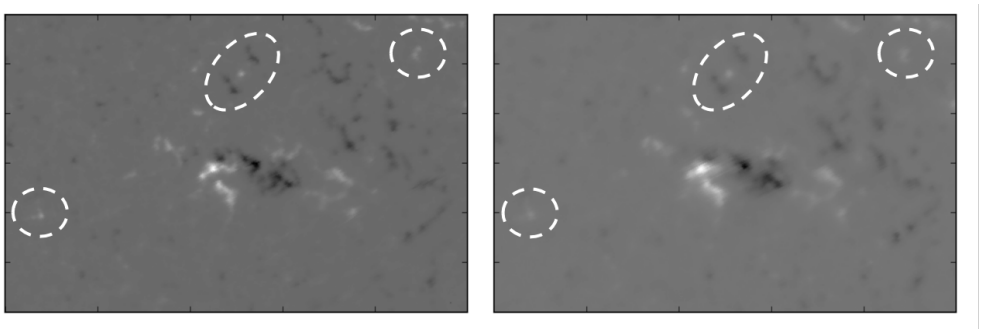

Figure 5.1: Photospheric (*left*) and chromospheric (*right*) magnetograms as observed by VSM/SOLIS. They are taken 100 minutes apart yet there is good correspondence between them as shown in encircled features.

5.3 Analysis & Results

5.3.1 Data selection & preparation

For present study, we have considered LoS photospheric and chromospheric magnetograms of active regions observed through the years 2014 and 2015. These years correspond to part of solar maximum (2014) and subsequent declining phase (2015) of solar activity. Hence, a good number of active regions are available for the study, and magnetic flux balanced region can be selected without overlap from the other active regions (although it is solar maximum of present cycle, it is much weaker compared to previous solar maxima; SILSO, 2019). Magnetograms have been selected by applying following criteria:

- Time gap between observations of photosphere and chromosphere should be as less as possible (less than 2 hours) so that there is maximum correspondence between features observed at those heights.
- Location of the active region and its spatial extent as seen in photospheric magnetogram should be close to disk center so as to avoid any projection effects. A condition is imposed that cosine of heliocentric angle $\mu < 0.9$.
- Continuum raster image should have less smearing so that the observed features can be properly compared.

- Region of interest about the active region is carefully selected in such a way that the magnetic flux imbalance at photospheric boundary is very low, by imposing $\Sigma B_{LoS}/\Sigma|B_{LoS}| < 0.05$
- Chromospheric magnetic field strength should be approximately within $\pm$1200 G. Chromospheric LoS magnetograms computed by applying WFA to Ca II 8542 Å Stokes profiles have certain limitations. They are accurate within 10% up to the field strengths of $\sim$1200 G and systematic errors are introduced for higher field strengths (Centeno, 2018).

Following aforementioned criteria, we have selected 38 active regions. They are of different field strengths, and corresponding regions of interest have different areas. We have followed the steps mentioned below before applying PMFE:

- Region of interest in chromospheric magnetogram corresponding to region in photospheric magnetogram is selected. Their coordinates would be different as the features would have noticeably moved on the solar disk in the time gap between their observations.
- Region of interest coordinates, μ and time of acquisition are noted and saved.
- As the implementation of PMFE involves using Fast Fourier Transform (FFT), it causes *aliasing effects* (Alissandrakis, 1981). Although its consequences are severe when magnetic field strength is high at RoI edges (which is not the case here), we have multiplied the magnetogram region of interest with a custom window function to mitigate any effects.

5.3.2 Potential magnetic field extrapolation

Solutions for current-free case, $\nabla \times \mathbf{B} = 0$, were proposed in terms of various special functions (Bessel function, Fourier series or Green's function) for a number of cases where different information at the boundary is available (B_{LoS}, $B_{Vertical}$ or $\mathbf{B}$; Alissandrakis, 1981 and references therein). They were given for a region of interest assuming the plane parallel geometry. For this statistical study, we have

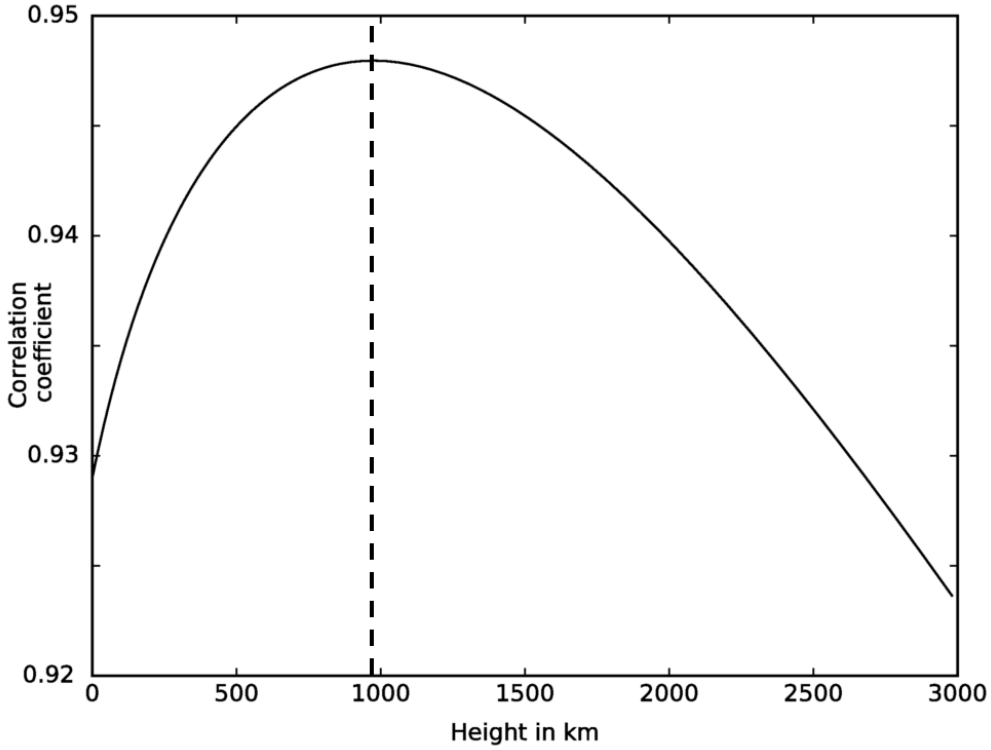

Figure 5.2: Correlation Coefficient for observed chromospheric magnetogram and computed magnetic field map from PMFE as a function of height of extrapolation.

used computationally less expensive solution proposed by Nakagawa and Raadu (1972) in terms of Fourier series, expanded by Alissandrakis (1981). It requires the map of magnetic field component that is normal to the surface at the boundary. So, we used LoS photospheric magnetogram from the disk center. We have selected the active regions accordingly. Its formulation is detailed in Alissandrakis (1981).

Using LoS photospheric magnetogram as lower boundary condition, we have extrapolated the magnetic field up to 3000 km above photosphere sampling at every 20 km height. Next, magnetic field map at each height that is obtained from PMFE is correlated with observed chromospheric magnetogram and Correlation Coefficient (CC) is calculated. Correlation coefficient versus height of extrapolation is plotted as shown in Figure 5.2. Height corresponding to maximum CC is noted. Figure 5.3 shows a sample of selected data and the result. It shows photospheric intensity image and LoS magnetogram, and chromospheric LoS magnetogram along with magnetic field map that is obtained by applying PMFE.

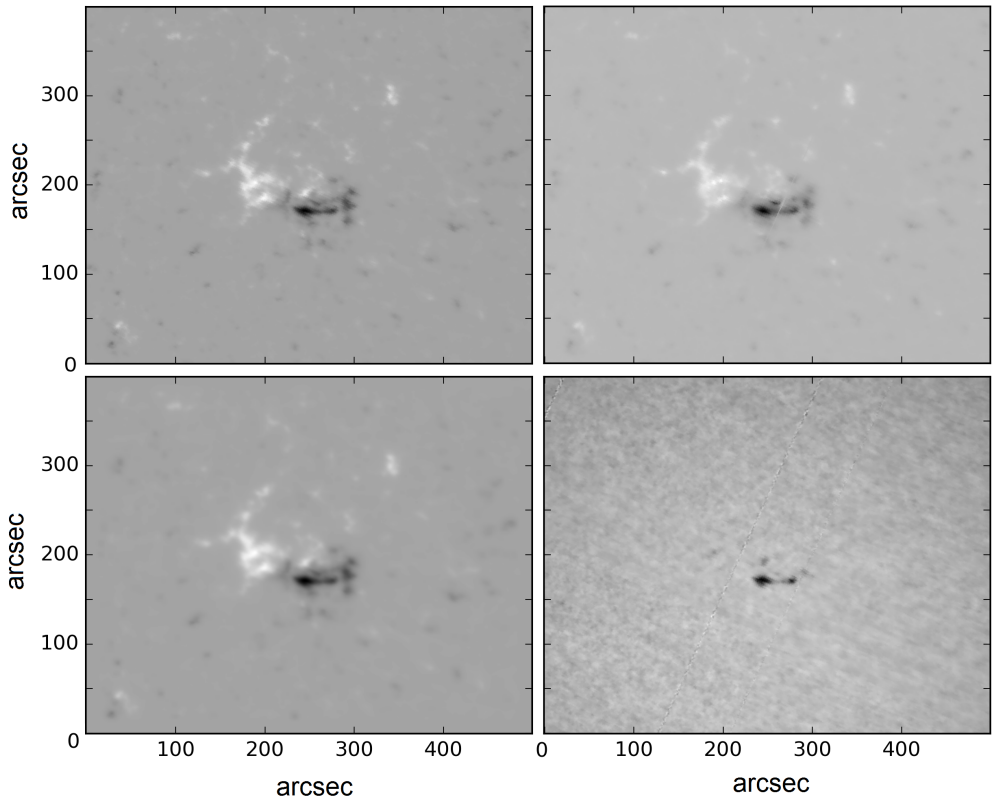

Figure 5.3: A sample of the active region used for the study (19/09/2015). *Top left* : Photospheric magnetogram, *top right*: chromospheric magnetogram, *bottom left*: magnetic field map constructed by applying potential extrapolation to photospheric magnetogram at 980 km (corresponds to highest CC with chromospheric magnetogram), and *bottom right*: continuum image of the active region.

5.3.3 Correlation height

We have applied PMFE to all the selected active regions. We have obtained the height corresponding to the maximum correlation for each active region. Figure 5.4 shows comparison of computed and observed field strengths for two different active regions (AR 12436 and AR 12448) with two different peak CC values. Scatter corresponding to computed field strength seems to be *narrower* than the scatter corresponding to the observed field strength, which is also noted in previous study by Choudhary et al. (2001). In some cases, computed and observed magnetic field values tend to deviate from each other at higher field strengths.

Figure 5.5 shows scatter plot and histogram of the inferred heights with bigger dot size representing higher CC (dot's size and CC are not linearly proportional). In

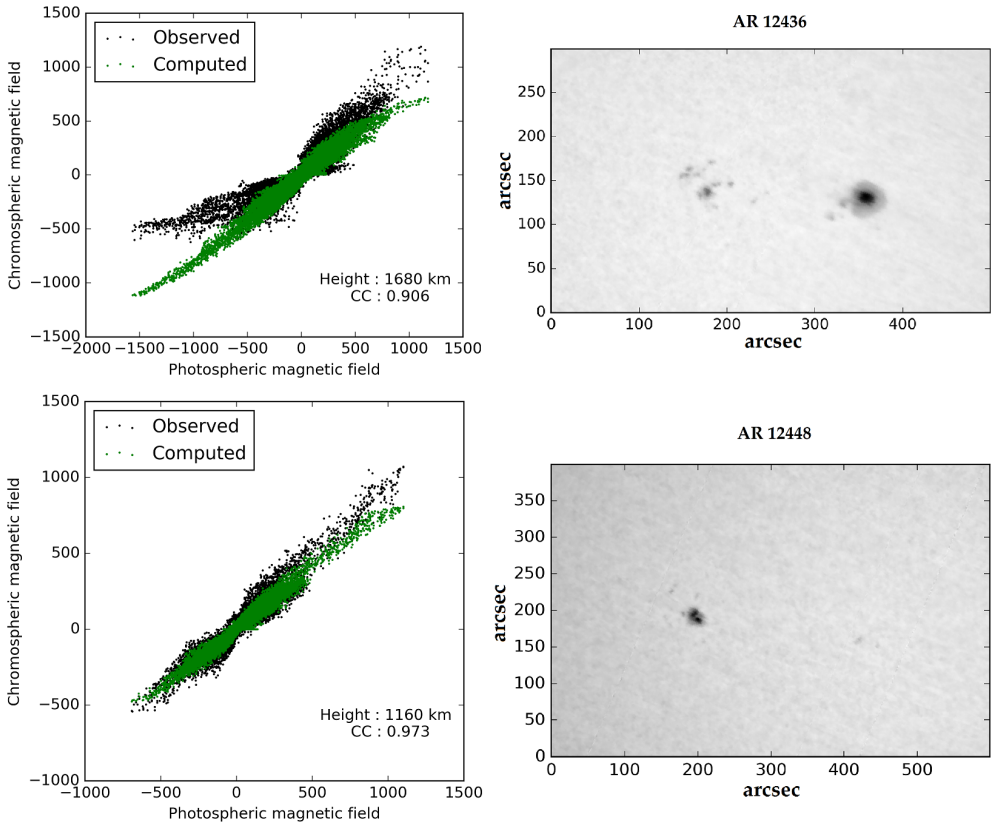

Figure 5.4: Observed and computed chromospheric magnetic fields vs. photospheric magnetic fields. Computed field from PMFE is constrained more tightly than observed field. *Top*: AR 12436 as observed on 23/10/2015, and *bottom*: AR 12448 as observed on 09/11/2015.

the Figure 5.5 (top), we observe that each active region has different maximum correlation height, spread between 500 to 1600 km above the photosphere. But, most of the regions show maximum correlation around 1000 to 1200 km. Corresponding histogram in the same figure shows large spread in the correlation height starting from 500 km to 1600 km, with peak being at ∼1110 km above the photosphere.

5.4 Summary & Discussion

We conducted a pilot study to compute the maximum correlation height of observed chromospheric magnetogram with respect to magnetograms modeled using

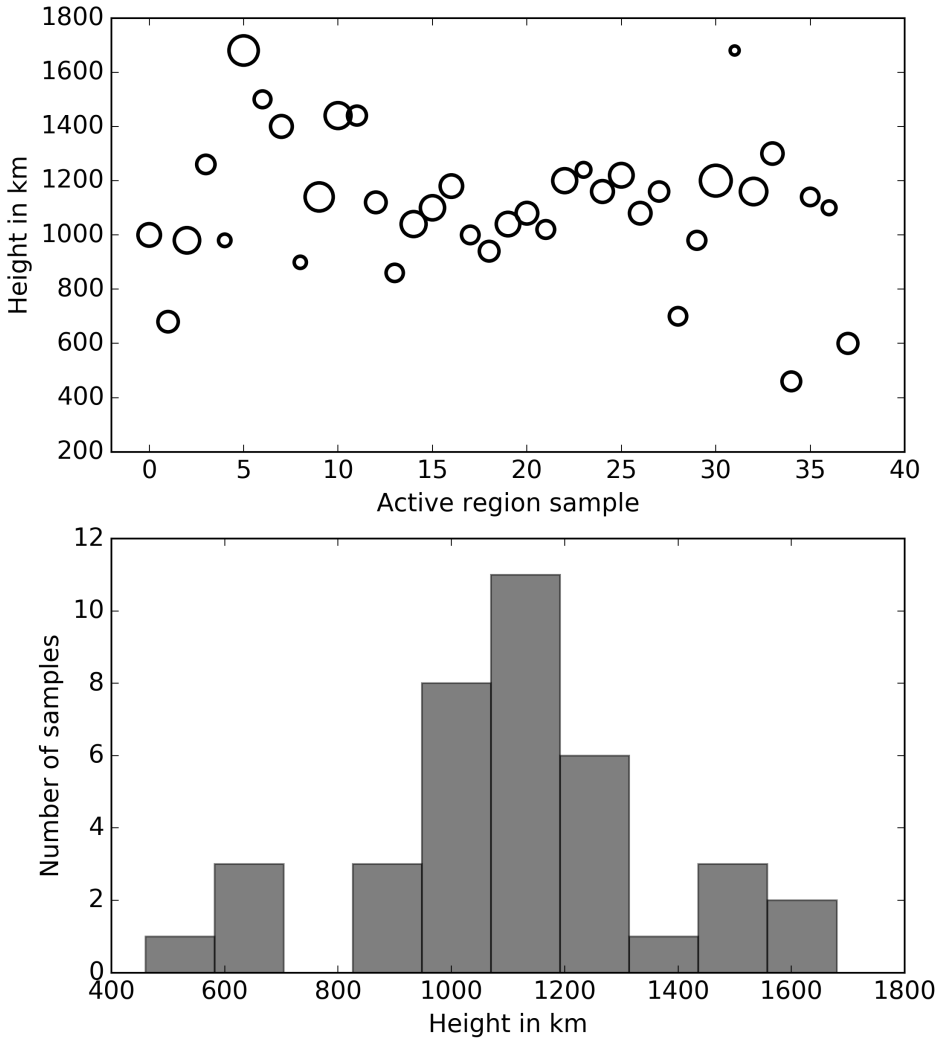

Figure 5.5: *Top*: heights corresponding to maximum correlation between computed and observed chromospheric magnetograms of selected active regions. *Bottom*: histogram of heights of maximum correlation that are shown in the top plot. The gap between 700 and 820 km is due to less number of samples.

their photospheric counterpart, in the active regions. We did so by applying potential magnetic field extrapolation to active region magnetic fields. Photospheric and chromospheric Line-of-Sight (LoS) magnetograms obtained from SOLIS are used for the study. They were constructed by using spectropolarimetric observations of Fe I 6302.5 Å and Ca II 8542 Å lines respectively.

Consequently, height of maximum correlation is found to be ∼1110 km above photosphere, which is likely the height of formation for Ca II 8542 Å spectral line.

But, to be more specific, this height is with respect to the line formation height of Fe I 6302.5 Å as photospheric magnetograms are constructed using that line. Photosphere is taken to be a height in solar atmosphere where optical depth for solar continuum at 5000 Å becomes 1 ($\tau_{5000} = 1$). Bommier et al. (2006) computed height of formation of Fe I 6302.5 Å line core with respect to $\tau_{5000} = 1$ as $\sim$260 km for an active region. In Jones et al. (2002), authors have applied potential field extrapolation to existing LoS magnetograms at a height of 200 km above photosphere in order to simulate VSM photospheric (Fe I 6302.5 Å) magnetograms. If we take these results as they are, estimate of height of Ca II 8542 Å line formation would be $\sim$1350 km from $\tau_{5000} = 1$.

We see a strong spread in histogram shown in Figure 5.5 with σ = 260 km which amounts to $>$ 20% of estimated height. In a previous work by Qu and Xu (2002), Ca II 8542 Å line core is found to be sensitive to height ranging from 1100 km to 1900 km with respect to $\tau_{5000} = 1$ for the quiet Sun. Lagg et al. (2017) present a plot corresponding to $\tau = 1$ height for various chromospheric spectral lines in the quiet Sun, and for Ca II 8542 Å it varies in the range of approximately 1100 km to 1900 km with respect to $\tau_{5000} = 1$. Comparing with aforementioned results, we can say that Ca II 8542 Å spectral line forms at lower heights in the active regions as compared to the quiet Sun.

Figure 5.6 shows one of the active regions used in this study and its comparison with lower coronal image taken from AIA/SDO. One set of field lines are marked with red and it looks like 'S'. It indicates that these field lines connect magnetic poles with twisting (Low and Berger, 2003) that is, magnetic field need not potential all the time. Although current-free modeling provides valuable information on relation between different features and magnetic fields, they are not so realistic representation of solar magnetic fields rather a first order approximation. In order to account for the *twist* in the magnetic field, α has to be non-zero. A simpler choice would be to use $\alpha(x, y, z)$ = constant, assuming *Linear Force-Free* (LFF) condition (Gary, 1989). A more realistic choice would be to use spatially varying α considering Non-Linear Force-Free (NLFF) magnetic fields (Low and Lou, 1990;

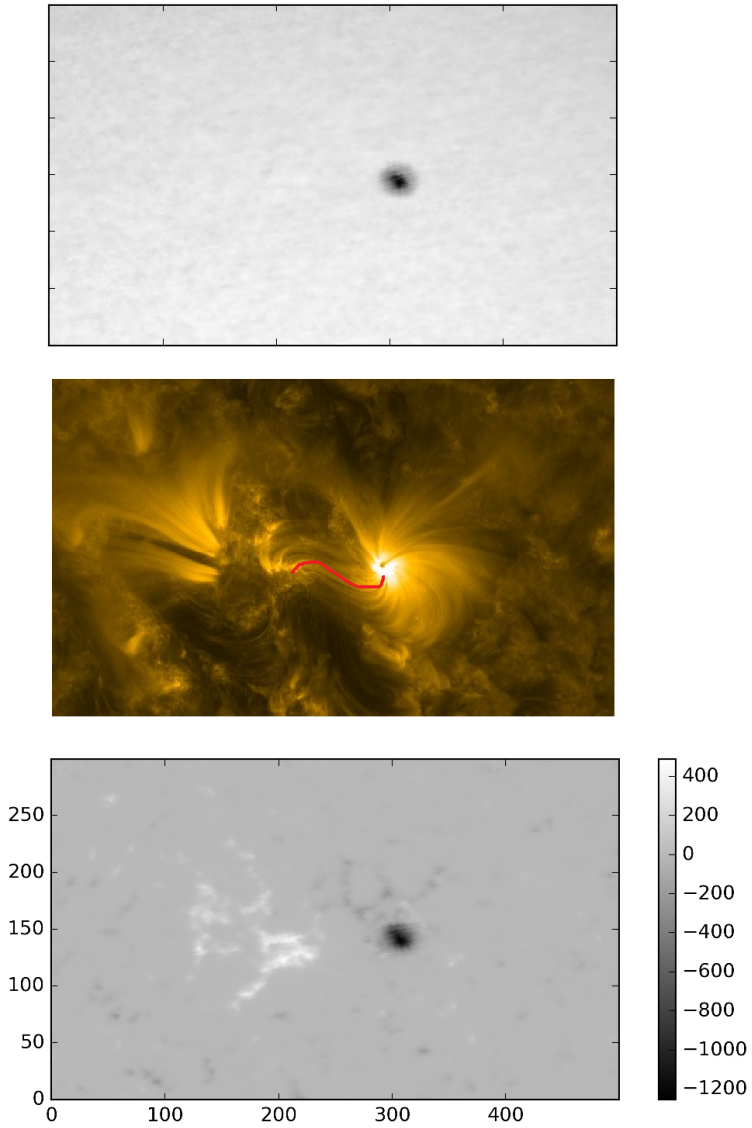

Figure 5.6: A sample of active region used for the study (17/06/2014). *Top*: white light image, *middle*: lower coronal image taken from AIA/SDO 171 Å, and *bottom*: photospheric magnetogram. In coronal image, a set of magnetic field lines in 'S' shape (marked in red colour) that indicate twist in the magnetic field.

Wheatland et al., 2002; Wiegelmann, 2004; and see Schrijver et al., 2006 for comparison of different methods). Both of these models were also applied to active regions to understand their relation with flares or eruptions (Jing et al., 2010; Sun et al., 2012; Feng et al., 2013). Hence, instead of using PMFE, LFF or NLFF extrapolations shall be used to better model the active regions.

For the better statistical study, data set also shall be expanded. As this is a pilot

study, we have used only two years of data. SOLIS LoS photospheric and chromospheric magnetograms are being recorded since 2003. Such large data sets also enable us to extend our study to various active regions such as sunspots, pores, and faculae. As we do not have such observations yet using Solar Scanning Polarimeter (SSP) for a statistical study (it is recently installed and there are not many active regions appearing due to the solar minimum), existing datasets of photospheric and chromospheric magnetograms were used. The dataset also shall be expanded to include observations using SSP. As only regions of interest can be observed, relatively smaller scale magnetic structures such as pores or selected sunspots can be observed. As there is 13 hour time difference between local times of SOLIS and KTT, chromospheric magnetic field measurements from these facilities shall complement each other and we shall have better temporal coverage. Although line formation height needs to be found from the radiative transfer, it can be independently examined from the comparative study of extrapolated and observed magnetic fields.

Chapter 6

Summary & Future Work

In this thesis, I have described instrumentation efforts that we made towards producing chromospheric magnetograms. I have briefly introduced the study of solar atmosphere and outlined the importance of measuring the magnetic fields in the solar atmosphere, especially in the chromosphere. I have described the development of a polarimeter for existing solar observational facility, associated subsystems, data processing pipeline, and analysis of the existing chromospheric magnetograms. This thesis work is summarized below along with its scope and what is needed for the future.

6.1 Chromospheric Magnetic Field

Magnetic fields permeate the solar atmosphere and they play central role in solar dynamics. Morphology and dynamics of so called active regions need to be studied at various heights throughout the solar atmosphere in order to advance the understanding of their role in solar activity and associated energetic events (Lagg et al., 2017). Towards this goal, a number of observing facilities produce magnetic field maps i.e., magnetograms of the Sun. Most of these magnetograms are made at the photospheric heights, and some are made at chromospheric heights. As chromosphere offers some unique conditions (e.g., close to force-free state; Metcalf et al., 1995), obtaining magnetograms at these heights would aid in better modeling of magnetic fields in the solar atmosphere (e.g., Wiegelmann et al., 2008).

6.1.1 Solar Scanning Polarimeter: Design, Development & Testing

We have added a new instrument, Solar Scanning Polarimeter (SSP) to Kodaikanal Tower-tunnel Telescope (KTT) of Kodaikanal Solar Telescope (KSO), an existing solar observational facility. Its objective is to expand the capabilities of present observing facility by enabling measurements of chromospheric magnetic fields of the active regions with Zeeman diagnostics of Ca II 8542 Å spectral line. KTT consists of a Coelostat for tracking, refracting objective and slit based High Resolution Spectrograph (HRS) at the focal plane. We have designed and developed SSP, tested its components in the laboratory, and installed it at the back-end of KTT before the slit. It consists of polarimeter unit, polarimetric calibration unit and raster scanner. Zero-order wave plates rotating in steps are used for polarimetric calibration and modulation. We have developed customized control electronics and observing software to operate SSP. It is capable of scanning a 120×60 arcsec^2 region of interest and producing spectrally resolved full Stokes profiles corresponding to that region.

Solar scanning polarimeter is also modeled to reduce the instrumental polarization which emerged as a natural consequence of the instrument setup. Instrumental polarization is a significant hurdle in the process of accurate measurements of Stokes parameters, especially in the optical system with inclined mirrors (e.g., Hale, 1912). We have extended previously developed instrumental polarization model of the telescope (Balasubramaniam et al., 1985), and propose a way to reduce polarization cross-talks. However, it needs to be fit to the observations of specific features (e.g., Skumanich et al., 1997) in order to get estimates of the model parameters.

6.1.2 Spectropolarimetry: Data Reduction, Calibration & Observations

State of Polarization (SoP) of light is sensitive to any changes in the media, making spectropolarimetry challenging, observation and post-processing wise. We have acquired required datasets that enable the extraction of full Stokes profiles. These data are processed accordingly by taking various effects into account (Wöhl et al., 2002) such as detector response, misalignment (between slit, grating and

detector), distortion caused by the optics and cross-talks due to instrumental polarization. A typical spectropolarimetric observation with 1 sec exposure and 60 scanning steps covering 36×60 arcsec^2 took approximately 14 minutes. We have estimated polarimetric sensitivity and accuracy of the observations to be few times 10^{-3} and 10^{-2} respectively, both of which are limited mainly by the detector.

A number of challenges specific to present system such as etaloning effect in the sensor, and lack of instrumental polarization cross-talk measurements (only modeling is done) are addressed and resolved. Relevant instrumental polarization cross-talks are inferred from observations and corrections are applied (e.g., Sanchez Almeida and Lites, 1992). Thusly, full Stokes parameters of the observed region of interest are extracted. Finally, Weak Field Approximation (WFA; Landi Degl'Innocenti, 1992) is applied to the Stokes profiles to obtain Line-of-Sight (LoS) magnetogram. Although we can detect characteristic Stokes Q/I and U/I profiles after binning several pixels, it is difficult to bring out meaningful information concerning the transverse magnetic field. Polarimetric sensitivity is restricted by etaloning effect in the sensor substrate. Slow readout of the detector causes polarimetric calibration a long time hence limiting the accuracy. A detector which has matching sensing area, good response for 850 nm wavelength radiation and faster readout would significantly improve the performance of the polarimeter.

6.1.3 Image Stabilization System: Design, Development & Testing

Raster scan observations of solar scanning polarimeter suffer from poor image resolution as there is no closed loop control over tracking and imaging. We have envisaged an Image Stabilization System (ISS) to reduce the image motion that is ubiquitous in ground-based observations. We have designed and developed ISS and associated subroutines. We utilized correlation tracking (e.g., von der Lühe, 1983) of solar features such as sunspots or pores to dynamically compute the image motion. We have used piezo-actuator based tip-tilt mount with mirror to apply the corrections to arrest the image motion. Dynamic computation of correlation is implemented using Fast Fourier Transform (Von Der Lühe et al., 1989). We have

tested the subroutines for speed and accuracy. We have tested the ISS in the laboratory and tuned the tip-tilt actuator system. We have integrated image stabilization system into scanning polarimeter and tested it at KTT. We have achieved 0 dB bandwidth of 110 Hz, with a closed loop image acquisition and correction rate of 563 s^{-1}. These developments are anticipated to improve the resolution of images obtained using raster scanner based system.

6.1.4 Correlation between the Chromospheric and Potential Extrapolated Magnetic Fields in Active Regions

We have used potential extrapolation (Alissandrakis, 1981) of active region magnetic fields in order to estimate the probable height of Ca II 8542 Å spectral line formation. We have used existing LoS photospheric and chromospheric magnetogram data obtained by Vector SpectroMagnetograph (VSM) of Synoptic Long-term Optical Investigations of the Sun (SOLIS; Keller et al., 2003) to model the active region magnetic fields. By means of doing so, we have arrived at an estimate for the Ca II 8542 Å line formation height (Choudhary et al., 2001). We have assumed a relatively simpler model of active region magnetic field being current-free or potential. Subsequently we have used this condition to extrapolate the magnetic field to discrete heights spanning 3000 km above the photosphere, using photospheric magnetogram as lower boundary. Computed magnetic field at each of the discrete heights is compared with observed chromospheric magnetogram to obtain height of their maximum correlation. Although spectral line formation is determined from theory of radiative transfer in magnetized solar atmosphere, statistical studies like the aforementioned one can provide an outlook on probable height of line formation. In future, we hope to expand the dataset and model with much more realistic conditions such as applying Non-Linear Force-Free (NLFF; e.g., Low and Lou, 1990) extrapolations to refine our present study.

6.2 Future Scope & Needs

6.2.1 Multi-line Spectropolarimetry

Solar scanning polarimeter is developed as a chromospheric vector magnetograph for observing Ca II 8542 Å spectral line. However, its capabilities can be expanded to observe multiple spectral lines. We have made provision at HRS to record spectra of observing two lines simultaneously for their comparative study (Nagaraju et al., 2008a): Hα 6563 Å and Ca II 8662 Å. We have considered the space restrictions imposed at high resolution spectrograph to mount multiple detectors. We have also modified the observing software to conduct two-line spectropolarimetric observations. We tested retardance of the waveplates for 6563 Å experimentally and results are tabulated in Table 6.1.

Table 6.1: Retardance values of waveplates at 6563 Å.

Waveplate	Fraction of λ	Retardance
QWP, CWP	0.331	$\lambda/3.02$
HWP	0.666	$2\lambda/3$
AQWP	0.258	$\lambda/3.88$

Present balanced modulation scheme is designed keeping single wavelength of observation in mind (8542 Å). Hence, we are preparing a new modulation scheme that results in good polarimetric efficiency for both the aforementioned lines of interest.

Although waveplates are still relevant in solar polarimetric observations, other modulators mentioned in Section 2.1 have a specific advantage of speed. By modulating the intensity at a rate that is higher than the frequency of seeing induced variations, corresponding cross-talks can be significantly reduced. A combination of such temporal and spatial modulations can provide highest polarimetric sensitivity as well as accuracy. Some progress has already been made by testing liquid crystal based materials as polarimetric modulators (Nagaraju et al., 2018). In addition, high speed adaptive image correction systems (for starters, tip-tilt based

image stabilization system) would enable high imaging resolution also. Such instruments would also output high data volume for the processing and analysis.

6.2.2 Spectropolarimetric Inversions

Observed Stokes profiles are shaped by solar atmospheric conditions, and we shall retrieve the information on physical parameters such as temperature, magnetic field using the observations. It is a problem of *inversion* and it is analytically a complex problem. In practice, solutions are obtained by numerical computations. By applying theory of radiative transfer, Stokes profiles shall be inverted and thereby solar atmospheric conditions shall be obtained. Weak field approximation that is used to compute magnetic field has very limited scope when it comes to estimating physical parameters. By applying spectropolarimetric inversions to Ca II 8542 Å, we get a more detailed picture of the physical conditions of the chromosphere, and to some extent photosphere as well (Quintero Noda et al., 2016).

Polarized radiation transfer equation in magnetized media takes the form of (Jefferies et al., 1989)

$$\frac{d\mathbf{I}}{dz} = -\mathbf{K}_t(\mathbf{I} - \mathbf{S}) \tag{6.1}$$

Here, $\mathbf{I}$ is Stokes vector, z is height and $\mathbf{S}$ is the source function. In the same equation, $\mathbf{K}_t$ is a 4×4 matrix that consists of various terms representing absorption and magneto-optic effects of magnetized media on propagating polarized radiation. They are functions of optical depth and they depend on physical conditions of the atmosphere such as temperature, velocity and magnetic field. Their detailed formulation is presented in Jefferies et al. (1989). The formulation shows that Stokes profiles' dependence on the atmospheric parameters is very complex in nature. A reliable method to obtain solution is by numerical means using *response function* formulation, that is given by (Stix, 2004, Chapter 4),

$$\delta\mathbf{I} = \int \mathbf{R}_x(\lambda, \tau)\delta_x(\tau)d\tau \tag{6.2}$$

Here, **I** is Stokes vector and $\mathbf{R}_x$ is the response function. $\mathbf{R}_x$ indicates how sensitive output (Stokes profile) is to change in a particular input parameter (x). At each wavelength point (λ) Stokes parameters are computed by integrating the effects of physical conditions over given range of τ.

We have used Non-LTE Inversion COde using the Lorien Engine (NICOLE) (Socas-Navarro et al., 2015) for inverting the Stokes profiles. It considers NLTE conditions of the chromosphere. It employs a number assumptions, nevertheless they has been tested to be mostly valid for Ca II lines (Socas-Navarro et al., 2015 and references therein). Some of the relevant assumptions being : (1) NLTE atomic populations are computed assuming statistical equilibrium, (2) Frequency and directions of emitted photon and previously absorbed photons are independent of each other, (3) Only Zeeman effect induced polarization is considered, and (4) At each spatial location Stokes profiles are computed assuming that the same conditions extend in horizontal direction infinitely.

For the process of inversions, we input the observed Stokes profiles, and a guessed model atmosphere as a starting point. A model atmosphere consists of temperature (T), three components of the magnetic field (B_x, B_x and B_z), line of sight velocity (v_z), electron pressure (p_{el}) and micro-turbulent velocity (v_{mic}) as functions of optical depth (τ_{5000}). These parameters varied in a small amount, corresponding Stokes profiles are synthesized and weighted χ^2 is computed. This process is repeated to minimize the χ^2, and it is stopped when acceptable χ^2 is achieved or maximum number of iterations is reached. Main outputs are best fit model atmosphere and best fit Stokes profiles.

We used FALC quiet Sun model atmosphere (Fontenla et al., 1993) that is distributed with NICOLE package as a starting point. It produces quiet Sun spectra that is closer to the observed one (Quintero Noda et al., 2016), therefore it might converge faster and to a better solution. Model atmospheric parameters are varied by setting the number of *nodes*. Nodes are the points distributed (by default there are equally spaced) across τ_{5000} at which parameters are varied. For example, suppose two nodes are set for T for the range τ_{5000} = 1.5 to -7.5. It means T is varied

at τ_{5000} = 1.5 and τ_{5000} = -7.5 and rest of the values are inferred by connecting these nodes (straight line). Table 6.2 lists out number of nodes and other parameters used for the inversion.

Table 6.2: Input parameters and nodes used for inverting Stokes profiles with NICOLE. Number of nodes are equally spaced in τ.

Parameter	Value
Starting wavelength	8541.32 Å
Wavelength step	10.8 mÅ
No. of wavelength points	180
Wavelength range	1.90 Å
Instrumental broadening	1.1 km/s
Inversion mode	NLTE
Noise level	1.7×10^{-3}
Parameter	**No. of nodes**
Temperature, T	6
Line-of-sight velocity, v_{los}	1
Magnetic field component, B_z	2
" , B_y	2
" , B_x	2
Micro-turbulent velocity, v_{mic}	1

We present sample inversions of the Stokes profiles obtained from three regions near the sunspot. They are Stokes profile of 2×2 binned pixels to reduce the noise. We have carefully normalized them with respect to the local continuum. They are inverted following aforementioned conditions. Note that $Q \rightarrow U$ and $U \rightarrow Q$ cross-talks are not corrected as the instrumental polarization model parameters are yet to be estimated by using observations. Hence, we present transverse magnetic field strength without azimuth. A quick look reveals that the initial model temperature corresponding to τ_{5000} = -4.5 to -7.5 has changed. Geometric height corresponding to τ_{5000} = -4.5 to -7.5 is most likely the region where line core is sensitive to the temperature (see Quintero Noda et al., 2016 for the study using response functions). We see that B_{LoS} has increased with height in the regions away from the umbra.

After these test runs, we see that the transverse magnetic field components are still difficult to obtain as Stokes Q and U do not have enough signal. This calls for the same requirement that is discussed earlier: detector. A faster detector with

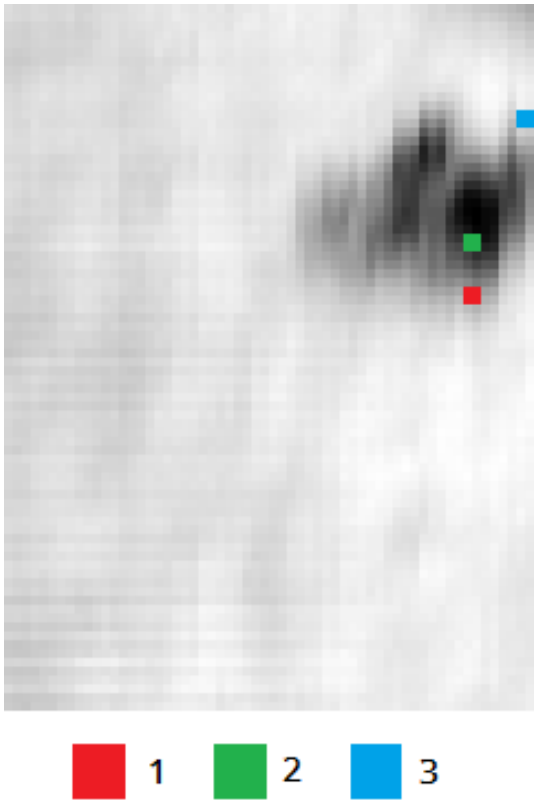

Figure 6.1: Raster image with marked regions from which Stokes profiles are inverted and corresponding fit models are presented.

better response (high quantum efficiency and no etaloning effect) would increase the signal to noise and there by improve the sensitivity.

We have applied spectropolarimetric inversions to all of the observed profiles however, the results have indicated that initial model requires careful monitoring (mainly due to signal-to-noise concerns). Multiple runs of spectropolarimetric inversions are daunting as they tend to be computational power hungry. In present case, a workstation with quad-core 3.2 GHz processor took several minutes to execute a single inversion run. It may require several such runs to obtain a proper fit if noise is high or initial parameters needed modification. For larger fields of view it becomes increasingly cumbersome and to tackle the problem new approaches may be needed. In that context, a future requirements could be: instead of synthesizing Stokes profiles several times for every inversion, one can synthesize several million Stokes profiles corresponding to a variety of the atmospheric conditions and

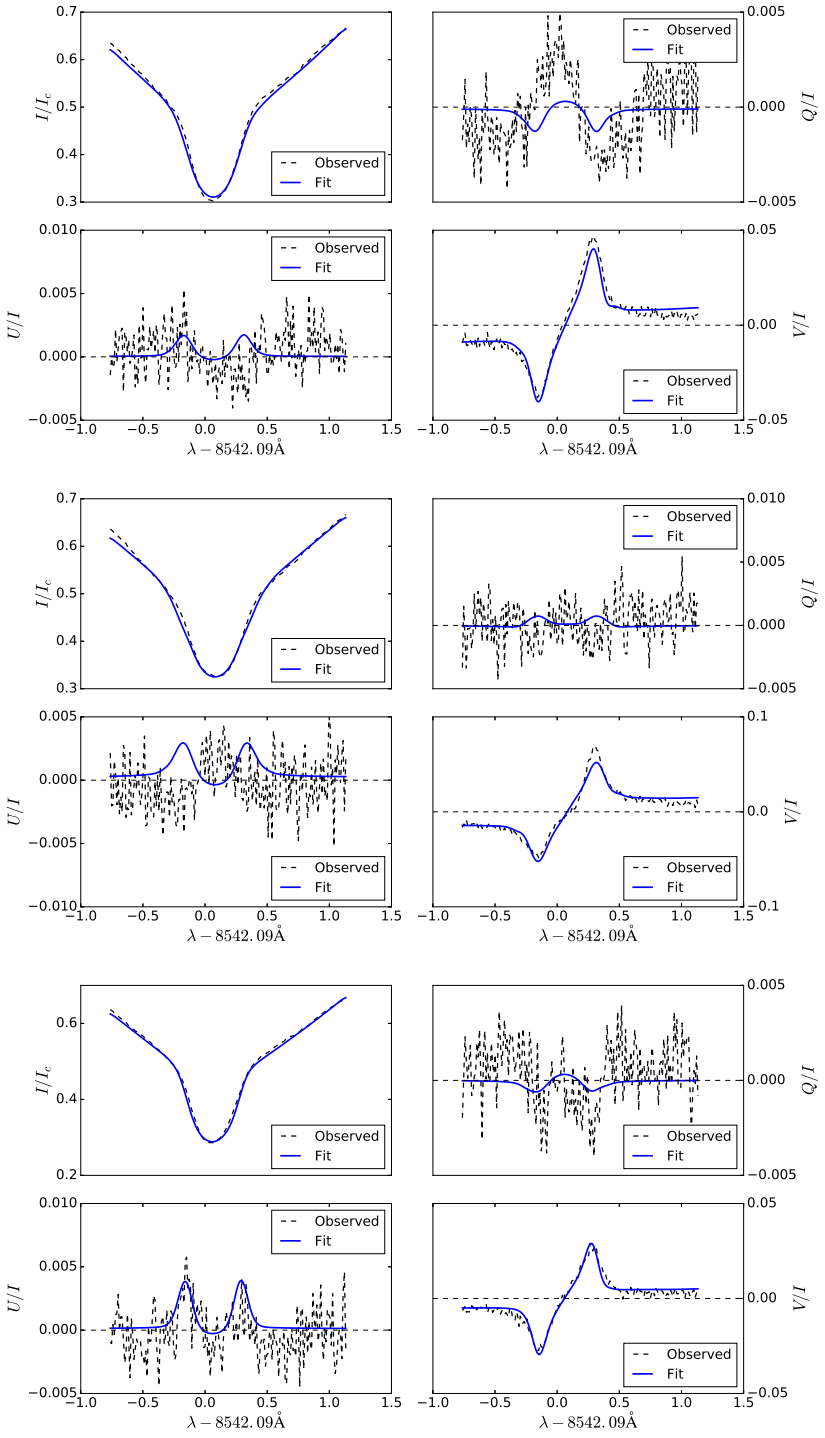

Figure 6.2: Best fit Stokes profiles for the observed Stokes profiles (with noise level of 1.7×10^{-3}) corresponding to the regions marked in Figure 6.1. *Top*: region 1, *middle*: region 2 and *bottom*: region 3.

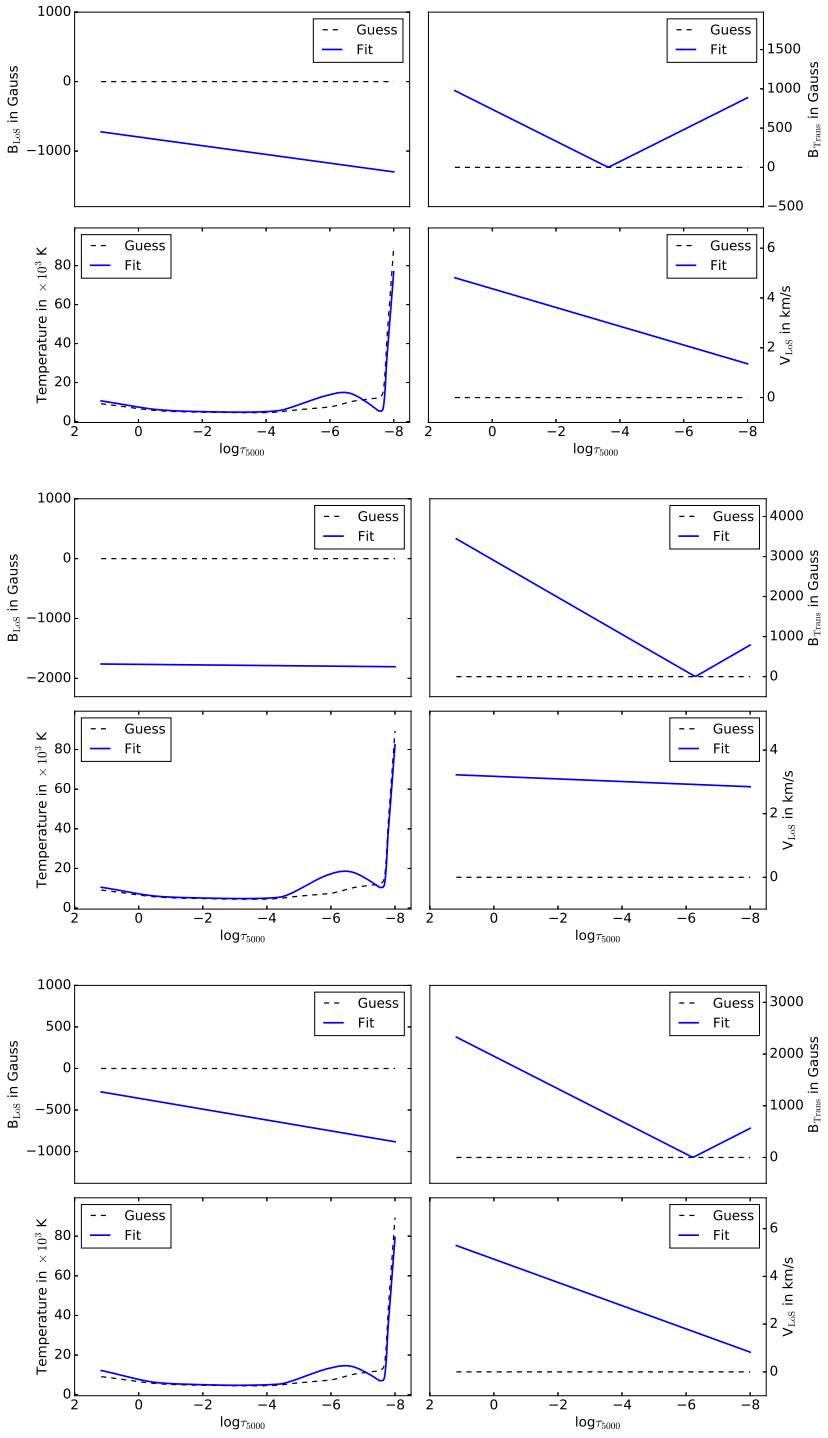

Figure 6.3: Best fit models for the observed Stokes profiles corresponding to the regions marked in Figure 6.1. *Top*: region 1, *middle*: region 2 and *bottom*: region 3.

store them for look-up. It requires having customized software tools to look-up the synthetic profile *database* but in the long run it may reduce the time spent for the inversions. In this regard an in-depth study of advantages and trade-offs is needed.

6.2.3 First Order Adaptive Optics

Wavefront tip and tilt are the first order *aberrations* that translate to image motion in the focal plane. Tip-tilt correction based image stabilization systems very often are at the first stage of Adaptive Optics (AO) systems (Glindemann, 1997; Coulter et al., 2014; Fischer et al., 2016; Rao et al., 2016; Johnson et al., 2016). Image stabilization system that is capable of correcting seeing induced image motion is the first order AO system, and it would significantly reduce the stroke requirement on the deformable mirror used in low order and high order AO systems leading to their better performance. On the other hand, it also reduces seeing-induced polarization cross-talks, resulting in better polarimetric accuracy (Judge et al., 2004).

At present, we are using 128×128 pixel region of interest of a 2560×2160 sCMOS detector for image acquisition. Corresponding frame rate for 1 ms exposure is $\sim$563 s^{-1}. Maximum achievable frame rate in global shutter mode is $\sim$660 s^{-1}. Present system bandwidth is mainly limited by this frame rate of the detector. At present, our ISS is capable of reducing the image motion to the tenth of diffraction limited resolution of the telescope. Future systems needed for upcoming larger telescopes such as National Large Solar Telescope (NLST; Hasan et al., 2010) need detector with faster readouts so that it will not become bottleneck of the image stabilization system.

Bibliography

Alissandrakis, C. (1981). On the computation of constant alpha force-free magnetic field. *Astronomy & Astrophysics*, 100:1997–200.

Anzer, U. (1987). Modelling of the magnetic field of solar prominences. In *Physical Processes in Comets, Stars and Active Galaxies*, pages 61–66.

Aschwanden, M. J., Wülser, J., Nitta, N. V., and Lemen, J. R. (2008). First Three-Dimensional Reconstructions of Coronal Loops with the STEREO A and B Spacecraft. I. Geometry . *The Astrophysical Journal*, 679(1):827–842.

Athay, R. G. (1975). *The Solar Chromosphere and Corona: Quiet Sun*, volume 53 of *Astrophysics and Space Science Library*. Springer Netherlands, Dordrecht.

Babcock, H. W. (1953). The Solar Magnetograph. *The Astrophysical Journal*, 118:387.

Bachmann, G. (1984). Reduction of Instrumental Polarization of Coelostat Telescopes. *Bulletin of the Astronomical Institutes of Czechoslovakia*, 35:308.

Balasubramaniam, K. S., Venkatakrishnan, P., and Bhattacharyya, J. C. (1985). Measurement of vector magnetic fields. I - Theoretical approach to the instrumental polarisation of the Kodaikanal Solar Tower. *Solar Physics* , 99:333–348.

Bappu, M. K. V. (1967). Solar Physics at Kodaikanal. *Solar Physics* , 1:151–156.

Beck, C., Schlichenmaier, R., Collados, M., Bellot Rubio, L., and Kentischer, T. (2005a). A polarization model for the German Vacuum Tower Telescope from in situ and laboratory measurements. *Astronomy & Astrophysics*, 443:1047–1053.

Beck, C., Schmidt, W., Kentischer, T., and Elmore, D. (2005b). Polarimetric Littrow Spectrograph – instrument calibration and first measurements. *Astronomy & Astrophysics*, 437:1159–1167.

Bommier, V., Landi Degl'Innocenti, E., Landolfi, M., and Molodij, G. (2006). UNNOFIT inversion of spectro-polarimetric maps observed with THEMIS. *Astronomy & Astrophysics*, 464(1):323–339.

Born, M. and Wolf, E. (1999). *Principles of Optics*.

Bumba, V. and Topolová-Růžičková, B. (1962). Polarization of light in solar spectrograph. I. Polarization on coelostat mirrors. *Bulletin of the Astronomical Institutes of Czechoslovakia*, 13:95.

Cao, W., Jing, J., Ma, J., Xu, Y., Wang, H., and Goode, P. R. (2006). Diffraction-limited Polarimetry from the Infrared Imaging Magnetograph at Big Bear Solar Observatory. *Publications of the Astronomical Society of the Pacific*, 118(844):838–844.

Capitani, C., Landi Degl'Innocenti, E., Cavallini, F., Ceppatelli, G., Landi Degl'Innocenti, M., Landolfi, M., and Righini, A. (1989). Polarization properties of a 'Zeiss-type' coelostat - The case of the solar Tower in Arcetri. *Solar Physics* , 120:173–191.

Centeno, R. (2018). On the Weak Field Approximation for Ca 8542 Å. *The Astrophysical Journal*, 866(2):89.

Choudhary, D. P., Sakurai, T., and Venkatakrishanan, P. (2001). Chromospheric Magnetic Field Of Solar Active Regions. *The Astrophysical Journal*, 560:439–444.

Collados, M. V. (2003). Stokes polarimeters in the near-infrared. *Polarimetry in Astronomy*, 4843(February 2003):55.

Coulter, R., Ahn, K., Varsik, J., Shumko, S., Cao, W., Gorceix, N., Kosovichev, A., Goode, P., and Plymate, C. (2014). Control and operation of the 1.6 m New Solar Telescope in Big Bear. *Ground-based and Airborne Instrumentation for Astronomy V*, 9147(July 2014):91475D.

Cox, L. J. (1976). The compensation of instrumental polarization by inclined mirrors. *Monthly Notices of the Royal Astronomical Society* , 176:525–532.

del Toro Iniesta, J. C. (2003). *Introduction to Spectropolarimetry*.

del Toro Iniesta, J. C. and Collados, M. (2000). Optimum Modulation and Demodulation Matrices for Solar Polarimetry. *Applied Optics* , 39:1637–1642.

Delbouille, L., Roland, G., and Neven, L. (1973). *Atlas photometrique du spectre solaire de [lambda] 3000 a [lambda] 10000*.

Demidov, M. L. (1991). Polarization characteristics of Jensch coelostat. *Solar Physics* , 135:193–197.

Edelstein, A., Amodaj, N., Hoover, K., Vale, R., and Stuurman, N. (2010). Computer control of microscopes using μmanager. *Current Protocols in Molecular Biology*, 92(1):14.20.1–14.20.17.

Elmore, D. F., Lites, B. W., Tomczyk, S., Skumanich, A., Dunn, R. B., Schuenke, J. A., Streander, K. V., Leach, T. W., Chambellan, C. W., Hull, H. K., and Lacey, L. B. (1992). <title>Advanced Stokes polarimeter: a new instrument for solar magnetic field research</title>. In Goldstein, D. H. and Chipman, R. A., editors, *Polarization Analysis and Measurement*, volume 1746, pages 22–33.

Evershed, J. (1909). Radial Movement in Sunspots. *Kodaikanal Observatory Bulletin*, 15:1–4.

Evershed, J. (1910). Radial Movement in Sun-spots. (Second Paper.). *Monthly Notices of the Royal Astronomical Society*, 70(3):217–226.

Feng, L., Wiegelmann, T., Su, Y., Inhester, B., Li, Y. P., Sun, X. D., and Gan, W. Q. (2013). Magnetic energy partition between the coronal mass ejection and flare from AR 11283. *The Astrophysical Journal*, 765(1).

Fischer, A., Schmidt, D., Heidecke, F., Soltau, D., and Berkefeld, T. (2016). The adaptive optics system of the 1.5m GREGOR solar telescope: four years of operation. *Adaptive Optics Systems V*, 9909(July 2016):990924.

Fleishman, G., Mysh'yakov, I., Stupishin, A., Loukitcheva, M., and Anfinogentov, S. (2018). Force-Free Field Reconstructions Enhanced by Chromospheric Magnetic Field Data. 101:1–17.

Fluri, D. M. and Stenflo, J. O. (2003). Depolarizing lines in the Sun's spectrum. *Astronomy & Astrophysics*, 398(2):763–773.

Fontenla, J. M., Avrett, E. H., and Loeser, R. (1993). Energy balance in the solar transition region. III - Helium emission in hydrostatic, constant-abundance models with diffusion. *The Astrophysical Journal*, 406:319.

Frigo, M. and Johnson, S. G. (2005). The design and implementation of FFTW3. *Proceedings of the IEEE*, 93(2):216–231. Special issue on "Program Generation, Optimization, and Platform Adaptation".

Gary, G. A. (1989). Linear force-free magnetic fields for solar extrapolation and interpretation. *The Astrophysical Journal Supplement Series*, 69(i):323.

Gary, G. A. (1996). Potential field extrapolation using three components of a solar vector magnetogram with a finite field of view. *Solar Physics*, 163(1):43–64.

Gary, G. A. (2001). Plasma beta above a solar active region: Rethinking the paradigm. *Solar Physics*, 203(1):71–86.

Georgoulis, M. K. and LaBonte, B. J. (2004). Vertical Lorentz Force and Cross-Field Currents in the Photospheric Magnetic Fields of Solar Active Regions. *The Astrophysical Journal*, 615(2):1029–1041.

Giovanelli, R. G. (1980). An exploratory two-dimensional study of the coarse structure of network magnetic fields. *Solar Physics*, 68(1):49–69.

Giovanelli, R. G. and Jones, H. P. (1982). The three-dimensional structure of atmospheric magnetic fields in two active regions. *Solar Physics*, 79(2):267–278.

Glindemann, A. (1997). Relevant Parameters for Tip-Tilt Systems of Large Telescopes. *Publications of the Astronomical Society of the Pacific*, 109(1976):682.

Goode, P. R., Cao, W., Ahn, K., Gorceix, N., Coulter, R., Goode, P. R., Shumko, S., Gorceix, N., and Coulter, R. (2011). The New Solar Telescope in Big Bear : Polarimetry I. In *ASP Conference Series*, volume 437, pages 345–349.

Grossmann-Doerth, U. (1994). Height of formation of solar photospheric spectral lines. *Astronomy & Astrophysics*, 285:1012–1018.

Hagyard, M. J. (1990). The significance of vector magnetic field measurements. *Memorie della Società Astronomica Italiana*, 61(2):337–357.

Hale, G. E. (1908). On the Probable Existence of a Magnetic Field in Sun-Spots. *The Astrophysical Journal*, 28(26):315.

Hale, G. E. (1912). Polarization Phenomena of Coelostat Telescopes. *Publications of the Astronomical Society of the Pacific* , 24:73–75.

Hale, G. E., Ellerman, F., Nicholson, S. B., and Joy, A. H. (1919). The Magnetic Polarity of Sun-Spots. *The Astrophysical Journal*, 49(26):153.

Hanaoka, Y., Sakurai, T., Shinoda, K., Noguchi, M., Miyashita, M., Fukuda, T., Suzuki, I., Hagino, M., Arai, T., and Yamasaki, T. (2011). Infrared Stokes Spectro-Polarimeter at the National Astronomical Observatory of Japan. In *ASP Conference Series*, volume 437, pages 371–378.

Harrington, D. M. and Sueoka, S. R. (2018). Polarization Modeling and Predictions for DKIST Part 4: Calibration Accuracy Over Field of View, Retardance Spatial Uniformity And Achromat Design Sensitivity. pages 4–8.

Hasan, S., Soltau, D., Kärcher, H., Süß, M., and Berkefeld, T. (2010). NLST: India's National Large Solar Telescope. *Astronomische Nachrichten*, 331(6):628–635.

Hathaway, D. H. (2015). The solar cycle. *Living Reviews in Solar Physics*, 12(1).

Helmli, F. and Scherer, S. (2002). Adaptive shape from focus with an error estimation in light microscopy. pages 188–193.

Hofmann, A. and Rendtel, J. (2011). Polarimetry with GREGOR. In Fineschi, S., editor, *Polarimetry in Astronomy*, volume 4843, page 112.

Ichimoto, K., Lites, B., Elmore, D., Suematsu, Y., Tsuneta, S., Katsukawa, Y., Shimizu, T., Shine, R., Tarbell, T., Title, A., Kiyohara, J., Shinoda, K., Card, G., Lecinski, A., Streander, K., Nakagiri, M., Miyashita, M., Noguchi, M., Hoffmann, C., and Cruz, T. (2008). Polarization calibration of the solar optical telescope onboard hinode. *Solar Physics*, 249(2):233–261.

Inoue, S., Hayashi, K., and Kusano, K. (2016). Structure and Stability of Magnetic Fields in Solar Active Region 12192 Based on Nonlinear Force-Free Field Modeling. *The Astrophysical Journal*, 818(2):168.

James, A. W., Green, L. M., Palmerio, E., Valori, G., Reid, H. A., Baker, D., Brooks, D. H., van Driel-Gesztelyi, L., and Kilpua, E. K. (2017). On-Disc Observations of Flux Rope Formation Prior to Its Eruption. *Solar Physics*, 292(5):1–24.

Jefferies, J., Lites, B. W., and Skumanich, A. (1989). Transfer of line radiation in a magnetic field. *The Astrophysical Journal*, 343:920.

Jing, J., Tan, C., Yuan, Y., Wang, B., Wiegelmann, T., Xu, Y., and Wang, H. (2010). Free magnetic energy and flare productivity of active regions. *The Astrophysical Journal*, 713(1):440–449.

Johnson, L. C., Cummings, K., Drobilek, M., Johansson, E., Marino, J., Richards, K., Rimmele, T., Sekulic, P., and Wöger, F. (2016). Status of the DKIST system for solar adaptive optics. *Adaptive Optics Systems V*, 9909(July 2016):99090Y.

Jones, H. P., Harvey, J. W., Henney, C. J., Hill, F., and Keller, C. U. (2002). Data analysis for the SOLIS Vector Spectromagnetograph. In *Magnetic Coupling of the Solar Atmosphere Euroconference and IAU Colloquium*, pages 15–18.

Joshi, J., Lagg, A., Solanki, S. K., Feller, A., Collados, M., Orozco Suárez, D., Schlichenmaier, R., Franz, M., Balthasar, H., Denker, C., Berkefeld, T., Hofmann, A., Kiess, C., Nicklas, H., Pastor Yabar, A., Rezaei, R., Schmidt, D., Schmidt, W., Sobotka, M., Soltau, D., Staude, J., Strassmeier, K. G., Volkmer, R., von der Lühe, O., and Waldmann, T. (2016). Upper chromospheric magnetic field of a sunspot penumbra: observations of fine structure. *Astronomy & Astrophysics*, 596:A8.

Judge, P. G., Elmore, D. F., Lites, B. W., Keller, C. U., and Rimmele, T. (2004). Evaluation of seeing-induced cross talk in tip-tilt-corrected solar polarimetry. *Applied optics*, 43(19):3817–3828.

Keller, C. U., Harvey, J. W., and Giampapa, M. S. (2003). SOLIS: an innovative suite of synoptic instruments. *Innovative Telescopes and Instrumentation for Solar Astrophysics*, 4853(February 2003):194.

Keller, C. U. and NSO Staff (1998). SOLIS Instrumentation Aspects. In Balasubramaniam, K. S., Harvey, J., and Rabin, D., editors, *Synoptic Solar Physics*, volume 140 of *Astronomical Society of the Pacific Conference Series*, page 539.

Kleint, L. (2016). First Detection of Chromospheric Magnetic Field Changes During an X1-Flare. *The Astrophysical Journal*, 834(1):26.

Kuhn, J. R., Balasubramaniam, K. S., Kopp, G., Penn, M. J., Dombard, A. J., and Lin, H. (1994). Removing instrumental polarization from infrared solar polarimetric observations. *Solar Physics*, 153(1-2):143–155.

Kumari, A., Ramesh, R., Kathiravan, C., and Wang, T. J. (2017). Addendum to: Strength of the Solar Coronal Magnetic Field – A Comparison of Independent Estimates Using Contemporaneous Radio and White-Light Observations. *Solar Physics*, 292(12):177.

Kuridze, D., Henriques, V., Mathioudakis, M., van der Voort, L. R., Rodríguez, J. d. l. C., and Carlsson, M. (2018). Spectropolarimetric inversions of the Ca ii 8542 Å line in a M-class solar flare. *The Astrophysical Journal*, 860(1):10.

Lagg, A., Lites, B., Harvey, J., Gosain, S., and Centeno, R. (2017). Measurements of Photospheric and Chromospheric Magnetic Fields. *Space Science Reviews*, 210(1-4):37–76.

Landi Degl'Innocenti, E. (1992). *Magnetic field measurements*, page 71.

Lemen, J. R., Title, A. M., Akin, D. J., Boerner, P. F., Chou, C., Drake, J. F., Duncan, D. W., Edwards, C. G., Friedlaender, F. M., Heyman, G. F., Hurlburt, N. E., Katz, N. L., Kushner, G. D., Levay, M., Lindgren, R. W., Mathur, D. P., Mcfeaters, E. L., Mitchell, S., Rehse, R. A., Schrijver, C. J., Springer, L. A., Stern, R. A., Tarbell, T. D., Wolfson, C. J., Yanari, C., Bookbinder, J. A., Cheimets, P. N., Caldwell, D., Deluca,

E. E., Gates, R., Golub, L., Park, S., Podgorski, W. A., Bush, R. I., Scherrer, P. H., Gummin, M. A., Smith, P., Auker, G., Jerram, P., Pool, P., Soufli, R., Windt, D. L., Beardsley, S., Clapp, M., Lang, J., and Waltham, N. (2012). The Atmospheric Imaging Assembly (AIA) on the Solar Dynamics Observatory (SDO). *Solar Physics*, 275:17–40.

Lin, H., Kuhn, J. R., and Coulter, R. (2004). Coronal Magnetic Field Measurements. *Astrophysical Journal Letters* , 613:L177–L180.

Lites, B. W. (1987). Rotating waveplates as polarization modulators for Stokes polarimetry of the sun - Evaluation of seeing-induced crosstalk errors. *Applied Optics* , 26:3838–3845.

Löfdahl, M. G. (2010). Evaluation of image-shift measurement algorithms for solar Shack-Hartmann wavefront sensors. *Astronomy & Astrophysics*, 524(15331):A90.

Low, B. C. and Berger, M. A. (2003). A Morphological Study of Helical Coronal Magnetic Structures. *The Astrophysical Journal*, 589(1):644–657.

Low, B. C. and Lou, Y. Q. (1990). Modeling solar force-free magnetic fields. *The Astrophysical Journal*, 352(1):343.

Maltby, P., Avrett, E. H., Carlsson, M., Kjeldseth-Moe, O., Kurucz, R. L., and Loeser, R. (1986). A new sunspot umbral model and its variation with the solar cycle. *The Astrophysical Journal*, 306(1908):284.

Mártinez Pillet, V., Collados, M., Sánchez Almeida, J. González, V., Cruz-Lopez, A., Manescau, A., Joven, E., Paez, E., Diaz, J., Feeney, O., Sánchez, V., Scharmer, G., and Soltau, D. (1999). LPSP & TIP: Full Stokes Polarimeters for the Canary Islands Observatories. In *ASP Conference Series*, volume 183, pages 264–272.

Martínez Pillet, V., del Toro Iniesta, J. C., Álvarez-Herrero, A., Domingo, V., Bonet, J. A., González Fernández, L., López Jiménez, A., Pastor, C., Gasent Blesa, J. L., Mellado, P., Piqueras, J., Aparicio, B., Balaguer, M., Ballesteros, E., Belenguer, T., Bellot Rubio, L. R., Berkefeld, T., Collados, M., Deutsch, W., Feller, A., Girela,

F., Grauf, B., Heredero, R. L., Herranz, M., Jerónimo, J. M., Laguna, H., Meller, R., Menéndez, M., Morales, R., Orozco Suárez, D., Ramos, G., Reina, M., Ramos, J. L., Rodríguez, P., Sánchez, A., Uribe-Patarroyo, N., Barthol, P., Gandorfer, A., Knoelker, M., Schmidt, W., Solanki, S. K., and Vargas Domínguez, S. (2010). The Imaging Magnetograph eXperiment (IMaX) for the Sunrise Balloon-Borne Solar Observatory. *Solar Physics*, 268(1):57–102.

Mathew, S. K., Bhatnagar, A., Prasad, C. D., Ambastha, A., and Land, A. (1998). Fabry-Perot filter based solar video magnetograph. *Astornomy & Astrophysics Supplement Series*, 133:285–292.

McCauley, P. I., Su, Y. N., Schanche, N., Evans, K. E., Su, C., McKillop, S., and Reeves, K. K. (2015). *Prominence and Filament Eruptions Observed by the Solar Dynamics Observatory: Statistical Properties, Kinematics, and Online Catalog*, volume 290.

McPeak, K. M., Jayanti, S. V., Kress, S. J. P., Meyer, S., Iotti, S., Rossinelli, A., and Norris, D. J. (2015). Plasmonic Films Can Easily Be Better: Rules and Recipes. *ACS Photonics*, 2(3):326–333.

Metcalf, T. R., Jiao, L., McClymont, A. N., Canfield, R. C., and Uitenbroek, H. (1995). Is the solar chromospheric magnetic field force-free? *Astrophysical Journal* , 439:474–481.

Mickey, D. L. (1985). The Haleakala Stokes polarimeter. *Solar Physics*, 97(2):223–238.

Moon, Y., Choe, G. S., Yun, H. S., Park, Y. D., and Mickey, D. L. (2002). Force-Freeness of Solar Magnetic Fields in the Photosphere. *The Astrophysical Journal*, 568(1):422–431.

Mullan, D. (2009). *Physics of the Sun*, volume 20096181 of *Pure and Applied Physics*. Chapman and Hall/CRC.

Munro, R. H., Gosling, J. T., Hildner, E., MacQueen, R. M., Poland, A. I., and Ross, C. L. (1979). The association of coronal mass ejection transients with other forms of solar activity. *Solar Physics*, 61(1):201–215.

Nagaraju, K., Phanindra, D. V. S., Prasad, S. K., Rao, D. S. S., and Sreekumar, P. (2018). Full Stokes polarimetry using Dual-Frequency Liquid Crystals. (July 2018).

Nagaraju, K., Ramesh, K. B., Sankarasubramanian, K., and Rangarajan, K. E. (2007). An efficient modulation scheme for dual beam polarimetry. *Bulletin of the Astronomical Society of India*, 35.

Nagaraju, K., Sankarasubramanian, K., and Rangarajan, K. E. (2008a). On the Weakening of the Chromospheric Magnetic Field in Active Regions. *Astrophysical Journal* , 678:531–540.

Nagaraju, K., Sankarasubramanian, K., Rangarajan, K. E., Ramesh, K. B., Singh, J., Devendran, P., and Hariharan (2008b). On the performance of a dual-beam polarimeter at Kodaikanal Tower Telescope. *Bulletin of the Astronomical Society of India*, 36:99–110.

Nagata, S., Morita, S., Ichimoto, K., Nishida, K., Nakatani, Y., Kimura, G., Kaneda, N., Kitai, R., UeNo, S., and Ishii, T. T. (2014). The Tandem Etalon Magnetograph of the Solar Magnetic Activity Research Telescope (SMART) at Hida Observatory. *Publications of the Astronomical Society of Japan*, 66(2):45.

Nakagawa, Y. and Raadu, M. A. (1972). On practical representation of magnetic field. *Solar Physics*, 25(1):127–135.

Povel, H. P. (2001). Ground-based Instrumentation for Solar Magnetic Field Studies, with Special Emphasis on the Zurich Imaging Polarimeters ZIMPOL-I and II. In *ASI Conference Series*, volume 248, pages 543–552.

Priyal, M., Banerjee, D., Karak, B. B., Muñoz-Jaramillo, A., Ravindra, B., Choudhuri, A. R., and Singh, J. (2014). Polar network index as a magnetic proxy for the solar cycle studies. *The Astrophysical Journal Letters*, 793(1).

Qu, Z.-Q. and Xu, Z. (2002). Key Properties of Solar Chromospheric Line Formation Process. *Chinese Journal of Astronomy and Astrophysics*, 2(1):71–80.

Quintero Noda, C., Shimizu, T., de la Cruz Rodríguez, J., Katsukawa, Y., Ichimoto, K., Anan, T., and Suematsu, Y. (2016). Spectropolarimetric capabilities of Ca ii 8542 Å line. *Monthly Notices of the Royal Astronomical Society*, 459(3):3363–3376.

Rao, C., Zhu, L., Rao, X., Zhang, L., Bao, H., Kong, L., Guo, Y., Feng, Z., Gu, N., and Liu, Y. (2016). INSTRUMENT DESCRIPTION AND PERFORMANCE EVALUATION OF A HIGH-ORDER ADAPTIVE OPTICS SYSTEM FOR THE 1 m NEW VACUUM SOLAR TELESCOPE AT FUXIAN SOLAR OBSERVATORY. *The Astrophysical Journal*, 833(2):1–10.

Ravindra, B., Kesavan, P., Thulasidharen, K. C., Rajalingam, M., Sagayanathan, K., Kamath, P. U., Dorjey, N., Dorjee, A., Kemkar, P. M. M., Dorjai, T., and Banyal, R. K. (2018). Installation of solar chromospheric telescope at the Indian Astronomical Observatory, Merak. *Journal of Astrophysics and Astronomy*, 39(5):60.

Ravindra, B. and Venkatakrishnan, P. (2003). On the correlation between the hell λ304 network brightening and the photospheric magnetic field. *Solar Physics*, 214(2):267–285.

Robustini, C., Leenaarts, J., and de la Cruz Rodríguez, J. (2018). The chromosphere above a δ -sunspot in the presence of fan-shaped jets. *Astronomy & Astrophysics*, 609:A14.

Rodríguez, J. D. C., Ramos, A. A., Bueno, J. T., and Cobo, B. R. (2015). An open-source , massively parallel code for non-LTE synthesis and inversion of spectral lines and Zeeman-induced Stokes profiles. *Astronomy & Astrophysics*, 577(A7):1–10.

Sakurai, T. (1989). Computational modeling of magnetic fields in solar active regions. *Space Science Reviews*, 51(1-2):302.

Sanchez, F., Collados, M., and Vazquez, M. (1992). *Solar observations: Techniques and interpretation*. Cambridge University Press.

Sanchez Almeida, J. and Lites, B. W. (1992). Observation and interpretation of the asymmetric Stokes Q, U, and V line profiles in sunspots. *Astrophysical Journal* , 398:359–374.

Sankarasubramanian, K., Gullixson, C., Hegwer, S., Rimmele, T., Gregory, S., Spence, T., Fletcher, S., Richards, K., Rousset, E., Lites, B., Elmore, D., Streander, K., and Sigwarth, M. (2004). The Diffraction Limited Spectro-Polarimeter : A new instrument for high resolution solar polarimetry . In *SPIE Conference Proceedings*, volume 5171, pages 207–218.

Sankarasubramanian, K., Samson, J. P. A., and Venkatakrishnan, P. (1999). Measurement of instrumental polarisation of the Kodaikanal tunnel tower telescope. In Nagendra, K. N. and Stenflo, J. O., editors, *Polarization*, volume 243 of *Astrophysics and Space Science Library*, pages 313–320.

Sankarasubramanian, K. and Venkatakrishnan, P. (1996). Ellipsometry of Coelostat Coatings Using a Babinet Compensator: Simulation of the Experimental Accuracy. *Solar Physics* , 167:1–7.

Sankarasubramanian, R., Rangarajan, K. E., and Ramesh, K. B. (2002). Measurement of solar vector magnetic fields using Kodaikanal tower telescope. *Bulletin of the Astronomical Society of India*, 30:473–490.

Schatten, K. H., Wilcox, J. M., and Ness, N. F. (1969). A model of interplanetary and coronal magnetic fields. *Solar Physics*, 6(3):442–455.

Scherrer, P. H., Bogart, R. S., Bush, R. I., Hoeksema, J. T., Kosovichev, A. G., Schou, J., Rosenberg, W., Springer, L., Tarbell, T. D., Title, A., Wolfson, C. J., and Zayer, I. (1995). The Solar Oscillations Investigation - Michelson Doppler Imager. *Solar Physics*, 162(1-2):129–188.

Schou, J., Borrero, J., Norton, A., Tomczyk, S., Elmore, D., and Card, G. (2012). Polarization Calibration of the Helioseismic and Magnetic Imager (HMI) onboard the Solar Dynamics Observatory (SDO). *Solar Physics*, 275:327–355.

Schou, J., Scherrer, P. H., Bush, R. I., Wachter, R., Couvidat, S., Rabello-Soares, M. C., Bogart, R. S., Hoeksema, J. T., Liu, Y., Duvall, T. L., Akin, D. J., Allard, B. A., Miles, J. W., Rairden, R., Shine, R. A., Tarbell, T. D., Title, A. M., Wolfson, C. J., Elmore, D. F., Norton, A. A., and Tomczyk, S. (2012). Design and Ground Calibration of the Helioseismic and Magnetic Imager (HMI) Instrument on the Solar Dynamics Observatory (SDO). *Solar Physics* , 275:229–259.

Schrijver, C. J. and Derosa, M. L. (2003). Photospheric and heliospheric magnetic fields. *Solar Physics*, 212(1):165–200.

Schrijver, C. J., Derosa, M. L., Metcalf, T. R., Liu, Y., Mctiernan, J., Régnier, S., Valori, G., Wheatland, M. S., and Wiegelmann, T. (2006). Nonlinear Force-Free Modeling of Coronal Magnetic Fields Part I: A Quantitative Comparison of Methods. *Solar Physics*, 235(1-2):161–190.

Schwabe, H. and Schwabe, H. (1844). Sonnen — Beobachtungen im Jahre 1843. *Astronomische Nachrichten*, 21(15):234–235.

Shimizu, T., Nagata, S., Tsuneta, S., Tarbell, T., Edwards, C., Shine, R., Hoffmann, C., Thomas, E., Sour, S., Rehse, R., Ito, O., Kashiwagi, Y., Tabata, M., Kodeki, K., Nagase, M., Matsuzaki, K., Kobayashi, K., Ichimoto, K., and Suematsu, Y. (2008). Image stabilization system for hinode (Solar-B) solar optical telescope. *Solar Physics*, 249(2):221–232.

SILSO (2019). Sunspot Index and Long-term Solar Observations (SILSO). `http://sidc.be/silso/home`.

Sinharoy, I., xy124, Holloway, C., Nummela, V., ng110, Stuermer, and magro11 (2016). Python-ZEMAX Dynamic Data Exchange, PyZDDE: Release version v2.0.3.

Skumanich, A. and Lites, B. W. (1987). Stokes profile analysis and vector magnetic fields. I - Inversion of photospheric lines. *The Astrophysical Journal*, 322(1986):473.

Skumanich, A., Lites, B. W., and Seagraves, V. M. P. P. (1997). The calibration of the advanced stokes polarimeter. *The Astrophysical Journal Supplement Series*, 110:357.

Socas-Navarro, H., de la Cruz Rodríguez, J., Asensio Ramos, A., Trujillo Bueno, J., and Ruiz Cobo, B. (2015). An open-source, massively parallel code for non-LTE synthesis and inversion of spectral lines and Zeeman-induced Stokes profiles. *Astronomy & Astrophysics*, 577(A7):A7.

Socas-Navarro, H., Elmore, D., Pietarila, A., Darnell, A., Lites, B. W., Tomczyk, S., and Hegwer, S. (2006). Spinor: Visible and infrared spectro-polarimetry at the national solar observatory. *Solar Physics*, 235(1-2):55–73.

Solanki, S. K., Inhester, B., and Schüssler, M. (2006). The solar magnetic field. *Reports on Progress in Physics*, 69(3):563–668.

Spiegel, E. A. and Zahn, J.-P. (1992). The solar tachocline. *Astronomy & Astrophysics*, 265:106–114.

Sridharan, R., Raja Bayanna, A., Louis, R. E., Kumar, B., Mathew, S. K., and Venkatakrishnan, P. (2007). An image stabilization system for solar observations. In Fineschi, S. and Viereck, R. A., editors, *Solar Physics and Space Weather Instrumentation II*, volume 6689, page 66890Z.

St. John, C. E. (1909). Note on the Polarizing Effect of Coelostat Mirrors. *Astrophysical Journal* , 29:301.

Stix, M. (2004). *The sun : an introduction*. Springer.

Sun, X., Hoeksema, J. T., Liu, Y., Wiegelmann, T., Hayashi, K., Chen, Q., and Thalmann, J. (2012). Evolution of magnetic field and energy in a major eruptive active region based on SDO/HMI observation. *The Astrophysical Journal*, 748(2).

Teuber, D., Tandberg-Hanssen, E., and Hagyard, M. J. (1977). Computer solutions for studying correlations between solar magnetic fields and skylab X-ray observations. *Solar Physics*, 53(1):97–110.

Tiwari, S. K. (2012). On the force-free nature of photospheric sunspot magnetic fields as observed from Hinode (SOT/SP). *The Astrophysical Journal*, 744(1).

Tiwary, A. R., Mathew, S. K., Bayanna, A. R., Venkatakrishnan, P., and Yadav, R. (2017). Imaging Spectropolarimeter for the Multi-Application Solar Telescope at Udaipur Solar Observatory: Characterization of Polarimeter and Preliminary Observations. *Solar Physics* , 292:49.

Tritschler, A., Rimmele, T. R., Berukoff, S., Casini, R., Craig, S. C., Elmore, D. F., Hubbard, R. P., Kuhn, J. R., Lin, H., McMullin, J. P., Reardon, K. P., Schmidt, W., Warner, M., and Woger, F. (2015). DKIST: Observing the Sun at High Resolution. In van Belle, G. T. and Harris, H. C., editors, *18th Cambridge Workshop on Cool Stars, Stellar Systems, and the Sun*, volume 18 of *Cambridge Workshop on Cool Stars, Stellar Systems, and the Sun*, pages 933–944.

Tu, C.-Y., Zhou, C., Marsch, E., Wilhelm, K., Zhao, L., Xia, L.-D., and Wang, J.-X. (2005). Correlation Heights of the Sources of Solar Ultraviolet Emission Lines in a Quiet-Sun Region. *The Astrophysical Journal*, 624(2):L133–L136.

Uitenbroek, H. (2010). Detection of chromospheric magnetic fields: a forward modeling approach . *Mem. Societa Astronomica Italiana* , 81:701.

Vemareddy, P. and Mishra, W. (2015). A FULL STUDY ON THE SUN–EARTH CONNECTION OF AN EARTH-DIRECTED CME MAGNETIC FLUX ROPE. *The Astrophysical Journal*, 814(1):59.

von der Lühe, O. (1983). A study of a correlation tracking method to improve image quality of ground-based solar telescopes. *Astronomy & Astrophysics*, 119:85–94.

Von Der Lühe, O., Widener, A. L., Rimmele, T., Spence, G., and Dunn, R. B. (1989). Solar feature correlation tracker for ground-based telescopes. *Astronomy & Astrophysics*, 224:351–360.

Wang, H., Ewell, M. W., J., Zirin, H., and Ai, G. (1994). Vector magnetic field changes associated with X-class flares. *The Astrophysical Journal*, 424:436.

Wheatland, M. S., Sturrock, P. A., and Roumeliotis, G. (2002). An Optimization Approach to Reconstructing Force-free Fields. *The Astrophysical Journal*, 540(2):1150–1155.

Wiegelmann, T. (2004). Optimization code with weighting function for the reconstruction of coronal magnetic fields. *Solar Physics*, 219(1):87–108.

Wiegelmann, T., Petrie, G. J., and Riley, P. (2017). Coronal Magnetic Field Models. *Space Science Reviews*, 210(1-4):249–274.

Wiegelmann, T. and Sakurai, T. (2012). Solar Force-free Magnetic Fields. *Living Reviews in Solar Physics*, 9.

Wiegelmann, T., Thalmann, J. K., Schrijver, C. J., Derosa, M. L., and Metcalf, T. R. (2008). Can we improve the preprocessing of photospheric vector magnetograms by the inclusion of chromospheric observations? *Solar Physics*, 247(2):249–267.

Wöhl, H., Kučera, A., Rybák, J., and Hanslmeier, A. (2002). Precise reduction of solar spectra obtained with large CCD arrays. *Astronomy & Astrophysics* , 394:1077–1091.

Yang, B. and Chen, H. (2019). Filament Eruption and Its Reformation Caused by Emerging Magnetic Flux. *The Astrophysical Journal*, 874(1):96.

Zeeman, P. (1897). The Effect of Magnetisation on the Nature of Light Emitted by a Substance. *Nature*, 55(1424):347–347.